SPIN-TAGGED ELECTRON-HYDROGEN SCATTERING: NEW MEASUREMENTS OF IONIZATION ASYMMETRIES FROM THRESHOLD TO 500 eV

by

DANIEL CROWE

A dissertation submitted to the Graduate Faculty in Physics in partial fulfillment of the requirements for the degree of Doctor of Philosophy, The City University of New York.

1995

This manuscript has been read and accepted for the Graduate Faculty in Physics in satisfaction of the dissertation requirement for the degree of Doctor of Philosophy.

Sept. 13, 1995
Date

Prof. Michael S. Lubell
Chair of Examining Committee

Sept 15, 1995
Date

Prof. Joseph B. Krieger
Executive Officer

Prof. Kurt Becker

Prof. Alvin Halpern

Prof. Marvin H. Mittleman

Prof. Leonard Roellig
Supervisory Committee

THE CITY UNIVERSITY OF NEW YORK

Abstract

SPIN-TAGGED ELECTRON-HYDROGEN SCATTERING:
NEW MEASUREMENTS OF IONIZATION ASYMMETRIES
FROM THRESHOLD TO 500 eV

by

Daniel Crowe

Adviser: Professor Michael S. Lubell

The electron-spin asymmetry for electron-impact ionization of atomic hydrogen has been measured from the ionization threshold to 500 eV. Comparisons are made to the previous measurements of Fletcher *et al* (1985), the predictions of the convergent close-coupling method of Bray and Stelbovics (1992, 1993) and the hidden-crossing theory of Macek, Ovchinnikov and Pasovets (1995), as well as related measurements on electron-atom systems. Subsidiary measurements reported include the characterization of the atomic-hydrogen beam via measurements of its electron-spin polarization, density and dissociation fraction; the characterization of the electron beam via measurements of its energy spread and polarization; and measurements of a dynamic beam-loading effect due to the ionization of residual hydrogen molecules.

ACKNOWLEDGEMENTS

First and foremost, I thank YHWH for giving me the ability to complete this dissertation. Without His help, I would never have finished.

Second, I thank my mentor, Michael S. Lubell, for allowing me to participate in his research program. My understanding of physical principles and techniques was greatly expanded under his guidance. In addition, he introduced me to the larger society of physicists.

Third, I thank my associates in the laboratory, especially Xiao-Qin Guo for tuning the electron beam and assisting with the data acquisition, Ning Chan for helping with the Monte Carlo simulations of the hydrogen beam, and Andrew Vasilakis for his help in preparing the apparatus for data acquisition.

Fourth, I thank Sol Forst and the other machinists in the Physics Department workshop for their expert workmanship in the fabrication of the apparatus.

Finally, I thank my family: My wife, Marilyn, and son, Christian, for patience and support; and my parents for allowing me to stay with them while I finished writing this document.

TABLE OF CONTENTS

LIST OF FIGURES

LIST OF TABLES

LIST OF TEXT BOXES

LIST OF ABBREVIATIONS

AC	alternating current
ADC	analog-to-digital converter
APS	American Physical Society
CCC	convergent close-coupling approximation
CCNY	The City College of New York
CEBAF	Continuous Electron Beam Accelerator Facility
CEM	channel electron multiplier
CFF	"Conflat" flange
CPU	central processing unit
DAC	digital-to-analog converter
DC	direct current
DEC	Digital Electronics Corporation
e/m	charge-to-mass ratio
FWHM	full width at half maximum
HWP	half-wave plate
i/o	input/output
JILA	Joint Institute for Laboratory Astrophysics
KEK	National Laboratory for High Energy Physics, Japan
LBCDA	laser-blocked code data acquisition
LN_2	liquid nitrogen
MCA	multichannel analyzer
MIT	Massachusetts Institute of Technology
NBS	National Bureau of Standards (currently NIST)
NEA	negative electron affinity
NEC	NEC Corporation

NIST	National Institute of Standards and Technology (formerly NBS and currently under attack by Congress)
NMR	nuclear magnetic resonance
NYU	New York University
OFHC	oxygen-free high-conductivity
QMA	quadrupole mass analyzer
QWP	quarter-wave plate
RAM	random-access memory
rf	radio frequency
SLAC	Stanford Linear Accelerator Center
SS	stainless steel
TC	thermocouple
u/e	atomic mass units per elementary charge
UHV	ultrahigh vacuum
VAC	volts AC
VDC	volts DC
VFC	voltage-to-frequency converter
Z	nuclear charge in units of elementary charge

CHAPTER ONE: HISTORICAL INTRODUCTION

The purpose of this chapter is to review the history of technological developments and experimental studies related to the present experimental study. Some theoretical developments are also discussed, but the emphasis is on technology and experiment. The theoretical developments relevant to the present experiment are discussed in more detail in Chapter Two. In addition, the emphasis in this chapter is on the general aspects of the technologies developed and the experiments performed. The discussion of the details of the performance of the technologies and the experimental results is deferred until Chapter Six, at which point comparisons are made with the present work.

I. GENERAL DESCRIPTION OF THE EXPERIMENT

The focus of the present experimental study is the measurement of the spin asymmetry in electron-impact ionization of atomic hydrogen. The measurements were made using crossed beams of spin-polarized free electrons and electron-spin-polarized hydrogen atoms. The spin asymmetry, A, is defined by

$$A \equiv \frac{\sigma(\uparrow\downarrow) - \sigma(\uparrow\uparrow)}{\sigma(\uparrow\downarrow) + \sigma(\uparrow\uparrow)}, \qquad (1.1)$$

where $\sigma(\uparrow\downarrow)$ [$\sigma(\uparrow\uparrow)$] is the cross section with incident- and atomic-electron spins antiparallel [parallel]. The spin

asymmetry was not measured directly, but was obtained from the counting-rate asymmetry, Δ, given by

$$\Delta \equiv \frac{R(\uparrow\downarrow) - R(\uparrow\uparrow)}{R(\uparrow\downarrow) + R(\uparrow\uparrow)}, \qquad (1.2)$$

where $R(\uparrow\downarrow)$ [$R(\uparrow\uparrow)$] is the counting rate with spins antiparallel [parallel]. The two asymmetries are related as

$$\Delta = A \cdot P_e \cdot P_H \cdot |\cos\alpha| \cdot (1 - F_2), \qquad (1.3)$$

where $\boldsymbol{P_e}$ ($\boldsymbol{P_H}$) is the polarization vector of the incident (atomic) electron, α is the angle between $\boldsymbol{P_e}$ and $\boldsymbol{P_H}$, and F_2 is the fraction of events due to molecular contamination in the hydrogen beam.

The spin-polarized electron beam was generated by photoemission from a GaAs crystal; the electron-spin-polarized atomic-hydrogen beam was generated by rf dissociation followed by state selection in a hexapole magnet. The details of the apparatus are described in Chapter Three. Spin-polarized beams are used because the detailed information about the initial states of the collision partners, when combined with previous measurements of absolute spin-averaged cross sections, allows the separation of singlet and triplet cross sections and the partial separation of direct and exchange amplitudes. These separations are discussed in more detail in Chapter Two.

The important subsidiary measurements performed include the characterization of the hydrogen beam via measurements of its electron-spin polarization, density and dissociation fraction; the characterization of the electron beam via

measurements of its energy spread and polarization; and measurements of a dynamic beam-loading effect due to the ionization of residual hydrogen molecules. The details of the data acquisition and analysis procedures are described in Chapters Four and Five, respectively.

II. DEVELOPMENT OF TECHNOLOGIES

The discussion of the development of technologies relevant to the present experimental study is divided into the discussion of those technologies relevant to the polarized-electron source and the discussion of those technologies relevant to the polarized atomic-hydrogen source.

A. Polarized-Electron Source

The discussion of the development of technologies related to the polarized-electron source begins with brief histories of the discovery of the electron and the discovery of electron spin, followed by the definition of polarization and a brief discussion of polarized-electron beams. It continues with a discussion of the various figures of merit relevant to polarized-electron sources followed by a discussion of the various polarized-electron sources that have been developed and concludes with a brief discussion of Mott polarimetry.

1. Discovery of the electron

The discovery of the electron has a long and interesting history (Anderson 1964; Marton & Marton 1980). The critical

experiment that led to the acceptance of the electron hypothesis was the measurement of e/m of cathode rays by J. J. Thomson (1897). The identification of Thomson as the discoverer of the electron is misleading, however, as he relied heavily upon the work of earlier investigators, although he neglected to reference their work: the paper contains no references at all!

Since the polarized-electron source of the present experiment utilizes the photoelectric effect, it is interesting to note that the discovery of the effect was first published by Hertz, Schuster and Arrhenius in 1887[1] (Jammer 1966, p. 33), and that the photoelectric discharge was found to be composed of the same particles as exist in cathode rays when their e/m was measured (Thomson 1899).

2. Discovery of electron spin

The concept of electron spin was developed twice by two groups who, evidently, were unaware of each other's work. The apparent reason for the lack of awareness is that the two groups were trying to explain different phenomena, and each

---

[1]Marton (1974) states, *"The first recorded observation of the photoelectric effect, or photoemission, occurred in 1839 when it was reported that an electric current generated by a cell composed of two metallic electrodes immersed in a conducting solution, or electrolyte, will increase when the cell is illuminated and that the extent of the increase will depend on the wavelength of the illuminating light."* No reference is given. He later states that the photoelectric effect was *"actually and explicitly discovered"* by Hertz in 1887. Van Laar and Scheer (1968) state that the photoelectric effect was first discovered in metals by Elster and Geitel in 1850. No further reference is given. Jammer (1966) gives complete references to the original literature.

group was not interested in the phenomena studied by the other group.

The first development of the concept of electron spin was motivated by the need to explain the converging helices of beta and secondary cathode rays excited by X-rays in air observed by Wilson (1923). Shimizu suggested that the helices "may be explicable on the assumption that the electron has a definite magnetic polarity which on account of gyroscopic action does not change rapidly in direction" (Compton 1921, p. 279). Compton calculated that a magnetic dipole moment of one Bohr magneton would account for the observations, but he implicitly assumed a gyromagnetic ratio of one and, therefore, a spin angular momentum of $\hbar$. Compton also spoke of two possible orientations saying, "The path may have the form of a right- or left-handed helix, according as the north or south pole of the beta particle is foremost" (Compton 1921, p. 280). This statement also implies a longitudinal polarization of beta rays.

The second development of the concept of electron spin was motivated by the need to explain the anomalous Zeeman effect, which was discovered in 1897 by Preston (Jammer 1966, p. 122). The introduction of the fourth quantum number and the Pauli exclusion principle (Pauli 1925) accounted for the anomalous effect, but the fourth quantum number was a mathematical artifice without a physical model. Kronig was the first to develop the concept of electron spin based upon Pauli's work, but he was discouraged from publishing it by

Pauli, Kramers and Heisenberg as well as by his inability to explain the fine-structure splitting of hydrogen including spin (Jammer 1966, p. 147). Soon after, Uhlenbeck and Goudsmit (1925, 1926) published their famous papers explaining the electron-spin model.

The Stern-Gerlach experiment (Gerlach & Stern 1922) that is invariably mentioned in modern physics textbooks in connection with the discovery of electron spin was actually motivated by the magnetic-core model of Sommerfeld, and the observed splitting was considered a resounding confirmation of that model. It was not until Uhlenbeck and Goudsmit replaced the magnetic-core model by the electron-spin model that the Stern-Gerlach experiment was reinterpreted in terms of the electron-spin model.

The first development above implies that the electron is an extended body, while the second development does not disagree with that interpretation. Dirac (1928) developed a relativistic quantum theory of the electron in which the electron is a point charge. The theory includes intrinsic spin angular momentum as an essential element without arbitrary assumptions.

3. Definition of polarization

An electron beam, or any ensemble of electrons, is polarized in a given direction if the two possible spin states are unequally populated. The polarization vector, $\boldsymbol{P}$, is defined as the expectation value of the Pauli spin operator, $\boldsymbol{\sigma}$, in the rest frame of the electron:

$$\boldsymbol{P} \equiv \langle \hat{\boldsymbol{\sigma}} \rangle . \qquad (1.4)$$

For an ensemble of electrons, the polarization in the z direction is given by

$$P_z \equiv \frac{N(\uparrow) - N(\downarrow)}{N(\uparrow) + N(\downarrow)} , \qquad (1.5)$$

where $N(\uparrow)$ $[N(\downarrow)]$ is the number of electrons with spin in the positive [negative] z direction.

4. Early attempts to observe polarized-electron beams

The first attempt to observe a polarized-electron beam was conducted by Cox, McIlwraith and Kurrelmeyer (1928). The electrons, which were derived from a radium β source, were scattered twice at 90° from gold targets and counted in a Geiger counter. The quantity of interest was the asymmetry between counting rates with the final beam directed at 90° and 270° relative to the initial beam direction. The results were inconclusive.

Many unsuccessful attempts followed in the next fifteen years. They included double scattering from a variety of materials at a variety of energies, transmission of high-energy electrons through magnetized iron foils, double diffraction of high-energy electrons, and a combination of scattering and diffraction of high-energy electrons. These attempts are referenced in Thomson (1930), Myers, Byrne and Cox (1934) and Shull, Chase and Myers (1943).

The first successful observation of a polarized-electron beam was conducted by Shull, Chase and Myers (1943). Their experiment was motivated by the electron-nucleus scattering

theory of Mott (1929, 1932) which was based upon the relativistic electron theory of Dirac (1928). Mott predicted that an electron beam with relativistic velocity would be polarized by scattering at large angles from a high-Z target, and that a relativistic polarized-electron beam would scatter asymmetrically at large angles from a high Z target. Shull, Chase and Myers measured this asymmetry in double scattering from gold (Z=79) foils. Some of the earlier, unsuccessful experiments were attempts to observe the Mott asymmetry in double scattering, but they were overwhelmed by instrumental errors (see Section 7).

5. Figures of merit

Polarized-electron beams can be generated by many methods, but not all polarized-electron beams are useful as probes in subsequent collisions. In addition, different applications for polarized-electron beams have different requirements. Several general figures of merit are presented in this section. The weight given to each figure of merit depends upon the application. The presentation of this section follows that of Kessler (1985, pp. 242-7).

The quantity of interest in most applications of polarized- electron beams, as in the present study, is a scattering asymmetry. In such situations, the measured asymmetry, Δ, is proportional to the spin asymmetry, A, times the electron polarization, P:

$$\Delta \propto A \cdot P \tag{1.6}$$

[cf. (1.3)]. The uncertainty in A due to the counting-statistics uncertainty in Δ is approximately

$$\sigma_A \approx \frac{C}{\sqrt{P^2 \cdot I}}, \tag{1.7}$$

(Kessler 1985, pp. 242-5) where C is independent of the parameters of the electron beam, I is the electron current at the interaction region, and $P^2 \cdot A^2 \ll 1$ is assumed. The uncertainty in A decreases as $P^2 \cdot I$ increases; therefore, $P^2 \cdot I$ serves as a useful figure of merit in applications where an asymmetry is measured. Note that I in the figure of merit is often interpreted as the current emanating from the source, but in (1.7) it is the current in the interaction region.

A bright beam, that is one that concentrates a high current density into a small solid angle, is also desirable at the interaction region. If the semi-aperture of the beam, α, is small ($\sin \alpha \approx \alpha$), the brightness, b, is given by (Kessler 1985, p. 258)

$$b = \frac{I}{\pi^2 \cdot r^2 \cdot \alpha^2}, \tag{1.8}$$

where r is the radius of a beam-cross-section minimum at which α is determined. Using the invariant emittance, ϵ, defined by

$$\epsilon \equiv r \cdot \alpha \cdot \sqrt{E}, \tag{1.9}$$

where E is the energy of the beam, the brightness at the interaction region, b_f, can be expressed in terms of the

characteristics of the source (signified by the subscript $_o$) as

$$b_f = \frac{I}{\pi^2 \cdot r_f^2 \cdot \alpha_f^2} = \frac{I \cdot E_f}{\pi^2 \cdot r_o^2 \cdot \alpha_o^2 \cdot E_o}. \qquad (1.10)$$

As E_f is not a characteristic of the source and maximizing $P^2 \cdot I$ is more important than maximizing I, another figure of merit is

$$q \equiv \frac{P^2 \cdot I}{r_o^2 \cdot \alpha_o^2 \cdot E_o} \qquad (1.11)$$

where I again refers to the current in the interaction region. The error introduced by using the source current in (1.11) instead of the interaction-region current is not as great as it is in (1.7), because the brightness, which determines the amount of losses in transmission, is included in (1.11).

Other figures of merit are the stability of polarization and current and the lifetime of the source. In experiments where the polarization is reversed frequently, the ease of reversal and the invariance of beam properties upon reversal are important considerations. Finally, in experiments with low-energy electrons, a small energy spread is desirable, especially one in which the energy distribution is well characterized.

6. Polarized-electron sources

Only those sources useful for scattering experiments, as discussed in the previous section, will be presented. Six processes are considered: low-energy Mott scattering,

photoionization of polarized atoms, the Fano effect, optically-pumped He discharge, field emission from W-EuS, and photoemission from semiconductors. Kessler (1985) reviews all these processes in considerable detail.

a. low-energy Mott scattering

As stated previously, Mott (1929, 1932) predicted that an electron beam with relativistic velocity would be polarized by scattering at large angles from a high Z target. By including the screening effect of the inner electrons, Massey and Mohr (1941) predicted that an electron beam with non-relativistic velocity would also be polarized by scattering from a high-Z target. Low-energy Mott scattering was first demonstrated thirty years later in Mainz (Deichsel 1961) using elastic e^--Hg scattering.

The physical mechanism involved in Mott scattering is spin-orbit coupling, which can be understood as the spin of the electron interacting with the magnetic field of the (screened) nucleus which is moving in the rest frame of the electron. Unfortunately, maxima in the polarization of the scattered beam occur near minima in the scattering cross section due to the smallness of the spin-orbit coupling compared to the Coulomb interaction. Additionally, in order to change the direction of polarization of the scattered beam, one must either change the energy of the incident unpolarized electron beam or change the scattering angle, either of which is relatively inconvenient compared with procedures available with other polarized-electron sources described below.

Operating sources using elastic e^--Hg scattering were developed at Karlsruhe (Jost & Kessler 1966), Mainz (Wilmers, Haug & Deichsel 1969), Stanford (Zeman, Jost & Gilad 1971; Bonner, Van Dort & Yearian 1975), Münster (Hanne & Kessler 1976) and Stirling (Hils & Kleinpoppen 1978; Hils, Jitschin & Kleinpoppen 1982).

b. photoionization of polarized atoms

One year after Mott's prediction, Fues and Hellmann (1930) predicted that polarized electrons could be obtained by photoionization of polarized alkali atoms. This method was first successfully applied at Yale thirty-five years later using a dc mercury high-pressure arc to ionize potassium atoms that had been state selected by passage through a hexapole magnet (Long, Raith & Hughes 1965).

Ideally, the polarization of the photoelectrons should equal the electron-spin polarization of the atomic beam; however, depolarization mechanisms include ionization of molecular contamination in the beam, two-step ionization, and the Fano effect, which is discussed in the next section. Hexapole magnets were used to state select the alkali atoms in all the sources described in this section. (This method of state selection is described in more detail in Section B.) The atomic polarization was then rotated adiabatically to a longitudinal polarization by means of solenoids that were coaxial with the atomic beams. The axial field, which extended to the photoionization region, also served to decouple the nuclear and electronic spins within the atoms,

resulting in a high electron-spin polarization of the atoms. Polarization reversal is achieved by reversing the current direction in the axial solenoids. The energy spread in the polarized-electron beam is determined by the spectrum of the light source and the energy dependence of the near-threshold photoionization cross section of the atom.

Baum and Koch (1969) developed a source in Bonn that used a xenon flash tube to ionize polarized potassium atoms. The ionizing radiation was passed through a nickel sulfate solution in order to filter out visible and infrared light and thereby minimize two-step ionization.

A superior source that used ^{6}Li rather than potassium was investigated at Yale (Hughes *et al* 1972) and later developed for use in high-energy-physics experiments at the Stanford Linear Accelerator Center (SLAC) (Alguard *et al* 1979). Affectionately nicknamed PEGGY, for Polarized Electron Gun, the source originally used a sealed xenon flashlamp which was later replaced by a vortex stabilized argon flashlamp. Two-step ionization was minimized by using a broadband uv interference filter comprising alternating layers of MgF_2 and Al. Lithium has the advantages over the other alkalis of having a higher photoionization cross section, a smaller hyperfine splitting, and negligible Fano-effect depolarization; however, it has the disadvantages of a high boiling point, which requires high oven temperatures, and a high ionization threshold, which requires the use of far-uv optics.

c. Fano effect

Fano (1969) predicted that highly-polarized electron beams could be obtained by photoionization of unpolarized alkali atoms by circularly-polarized light. Fano based his prediction upon the hypothesis of Seaton (1951) that spin-orbit coupling affects the continuum states of alkalis as well as the bound states. Using circularly-polarized light to ionize a polarized atomic-cesium beam, Lubell and Raith (1969) verified Seaton's hypothesis and showed that Fano's analysis was correct. Soon afterward, Kessler and Lorenz (1970) demonstrated the Fano effect with an unpolarized atomic-cesium beam.

As with low-energy Mott-scattering sources, which also rely upon spin-orbit coupling, Fano-effect sources also suffer from the disadvantage that maximum polarization occurs near minimum intensity. Fano-effect sources do have several advantages, however. First, they are easier to construct, less expensive and more compact than sources that require polarized atomic beams since hexapole magnets are unnecessary. Second, since they rely upon spin-orbit coupling, they use heavy (high Z) alkalis which have lower ionization potentials than lithium. Third, hyperfine coupling has negligible effect; therefore, no magnetic field is required in the ionization region. Such a field would increase the emittance (decrease the brightness) of the source in addition to adding to its complexity and cost. Fourth, polarization reversal in Fano-effect sources is achieved by rotating a quarter-wave

plate in the optics train to reverse the helicity of the incident photons. This method of polarization reversal is much easier to achieve than changing energy or angle as with low-energy Mott scattering. In addition, the stability of beam parameters upon polarization reversal is better for Fano-effect sources than for either of the previously discussed sources because there is no change in energy, angle or magnetic field.

Three operating Fano-effect sources have been developed. The first to be reported (von Drachenfels *et al* 1977) used a pulsed, frequency-quadrupled Nd-YAG laser to ionize atomic rubidium beams. It was designed for use at the Bonn synchrotron. The other two sources ran in dc mode and used atomic cesium beams. The first of these was developed at Yale (Wainwright *et al* 1978) and used a high-pressure mercury-xenon arc lamp. The second was developed at Münster (Möllenkamp & Heinzmann 1982) and used a high-pressure mercury arc lamp which resulted in a higher electron polarization but lower electron current than the Yale source.

d. optically-pumped helium discharge

A polarized-electron source using an optically-pumped helium discharge has been developed at Rice under the direction of G. K. Walters. The original configuration of this source (McCusker, Hatfield & Walters 1969, 1972) incorporated a spherical Pyrex bulb containing helium at a pressure of ~0.1 Torr. A radio-frequency generator excited the helium in a weak discharge. The excited atoms quickly

decayed to one of three states: the ground state 1^1S_0 or one of the metastable states 2^3S_1 or 2^1S_0. The metastable 2^3S_1 atoms were then optically pumped to 2^3P states using circularly-polarized resonant light from a low-pressure helium discharge lamp. These 2^3P atoms then decayed spontaneously back to the 2^3S_1 states. The optical pumping with circularly-polarized light systematically changes m_j according to the selection rule Δm_j = +1 (-1) for right- (left-) circular polarization whereas the spontaneous decay changes m_j randomly; therefore, the metastable triplet atoms in the optically-pumped discharge become (partially) polarized.

Collisions between metastable atoms can ionize one of the atoms with the other atom returning to its ground state. The electrons generated by these collisions retain their spin (Hill *et al* 1972) apparently because the lifetime of intermediate molecular reaction complexes is too short to allow magnetic interactions to perturb electron spin states (Keliher *et al* 1975). A weak magnetic field was provided by Helmholtz coils in order to provide a unique quantization axis. The field was collinear with the helicity of the pumping photons, giving the extracted electrons longitudinal polarization. The polarization was reversed by rotating a quarter-wave plate as in Fano-effect sources.

The performance of the source was examined during steady-state discharge and during afterglow. The use of afterglow required that the microwave generator be pulsed. The polarization of the extracted beam was significantly less than

the calculated polarization of the metastable triplet atoms primarily for two reasons: first, some electrons were generated in collisions involving metastable singlet atoms which are unpolarized; second, the extracted electrons ionized unpolarized residual gas in the extraction tube. The polarization was found to be higher in the afterglow than during steady-state discharge.

The source was later improved (Keliher, Gleason & Walters 1975) by introducing a second species with which the metastable atoms could collide and chemi-ionize. In addition, the spherical bulb was replaced by a flow tube to allow polarized electrons to be extracted from a steady-state afterglow. Optimum performance of the new source was achieved when the reactant species was carbon dioxide, which has large cross sections for both chemi-ionization and electron thermalization. Electron thermalization, by rotational and vibrational excitation of the reactant gas by electron impact, reduces the energy spread in the extracted beam and increases the extracted current by reducing electron losses due to diffusion to the wall.

The source was again improved (Hodge, Dunning & Walters 1979) by adding differential pumping to the extraction tube thereby reducing the production of unpolarized secondary electrons in that region. In addition, the relative orientation of the optical-pumping beam to the extraction tube was altered resulting in a transversely-polarized extracted beam. The final improvement reported by the Rice group (Gray

et al 1983) was the replacement of the helium discharge lamp by a NaF $(F_2^+)^*$ color-center laser which allowed selection of individual fine-structure levels during optical pumping. Optimum performance was achieved by selection of the 2^3P_1 states which saturated the polarization of the metastable triplet states.

Recently, a group at Orsay (Arianer *et al* 1993) has developed a source based upon the Rice model. Improvements include (1) increasing the flow velocity of the afterglow and (2) using a combination of linearly and circularly-polarized light to pump atoms to the 2^3P_0, thereby avoiding depolarization due to the D_2 transition.

The major disadvantage of this source is the relatively high pressures in the helium flow tube which make it inconvenient for use in experiments that require ultra-high vacuum.

e. field emission from EuS-coated tungsten tips

Fues and Hellmann (1930), in addition to suggesting photoemission from polarized alkali atoms, proposed that polarized electrons could be obtained by field emission from ferromagnetic materials. This method was first applied with (moderate) success thirty-seven years later in München (Hofmann *et al* 1967) using polycrystalline gadolinium. Another group at München (Müller *et al* 1972) first successfully extracted a highly-polarized electron beam by field emission from europium-sulfide-coated tungsten tips.

A simplified model of the W-EuS system suffices for understanding the emission of polarized electrons. Europium sulfide is a ferromagnetic semiconductor with a Curie temperature of 16.5 K. When cooled below the Curie temperature, the exchange interaction between the $4f^7$ electrons in EuS result in ferromagnetism and the splitting of the conduction band into two levels according to electron spin states. Both effects increase with decreasing temperature. The electric field used in field emission bends the energy bands of the insulating EuS but not the conducting W. Electrons near the Fermi level of W tunnel through the barrier formed by the bent conduction band of the EuS. Since the barriers for the two spin directions have different heights and widths, the emitted beam is highly polarized. The EuS layer acts as a spin filter. The polarization direction is determined by the direction of the magnetic field at the emitting tip.

The operating source at Bielefeld (Kisker *et al* 1978; Baum *et al* 1981) has a small energy width and the highest quality, q [cf. (1.11)], of any polarized-electron source; however, it also is the most difficult to construct and use for several reasons. First, the source requires a two-phase helium flow to maintain cryogenic temperatures. The stability of this flow is difficult to maintain resulting in instabilities in beam parameters. Second, the EuS layer must be annealed in a precise and difficult manner to obtain optimum performance. Third, ultrahigh vacuum must be

maintained in order to prevent contamination of the emitting tip. Fourth, the direction of polarization is difficult to control, and its control is coupled to the focusing of the beam.

f. photoemission from semiconductors

The final type of source of polarized electrons, photoemission from semiconductors, is significantly different from the types previously discussed in that it resulted from a minor modification to a well developed source of unpolarized electrons. The combination of relative low cost, compactness, high current yield and ease of use has made the GaAs photocathode, in particular, the "*model T*" of polarized-electron sources. The early history of NEA (unpolarized) photoemitters is reviewed by Bell and Spicer (1970), Bell (1973), Rougeot and Baud (1979) and Escher (1981).

The GaAs photocathode was developed by Scheer and van Laar[2] (1965) who were trying to design an efficient photoemitter in the optical and near-infrared regions. They calculated[3], and subsequently demonstrated, that a layer of Cs

---

[2]Williams and Tietjen (1971) and Schade, Nelson and Kressel (1972) refer to Simon (1963) as the first publication discussing NEA photocathodes. Simon (1963) is a U. S. Army contract quarterly report that, evidently, was originally classified and is now difficult, if not impossible, to obtain. The abstract to the final report for that contract (Simon & Fuselier 1964) states, "*Evidence in support of the negative electron affinity effect was obtained from photoemission measurements on cesium treated GaP.*"

[3]It is interesting to note that the NEA GaAs photocathode was the first photocathode to be designed based upon theory, albeit a semiempirical theory, as opposed to being developed upon a *purely* empirical basis.

adsorbed on the surface of a degenerately-doped p-GaAs crystal decreases the work function and forms a Schottky dipole layer which causes the crystal bands to bend downward near the interface to the extent that the bottom of the conduction band in the bulk is at a higher potential than the vacuum level, a situation known as negative electron affinity (NEA) (see Figure 1.1). NEA allows thermalized conduction electrons which diffuse to the surface to be emitted.

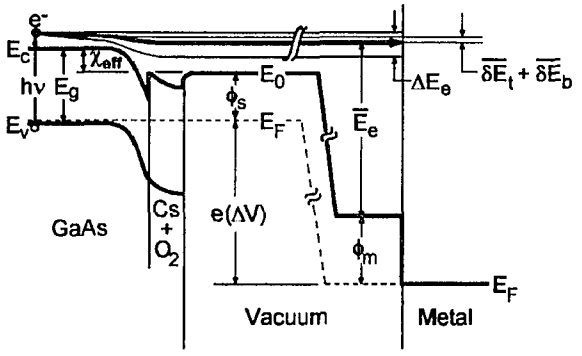

Figure 1.1 Energy-band diagram of an NEA GaAs:Cs-O photocathode showing the excitation of an electron-hole pair followed by the emission and acceleration of the electron. E_c (E_v) is the energy of the conduction (valence) band edge in the bulk; hν is the energy of the incident photon; $E_g \equiv E_c - E_v$ is the bandgap energy; E_0 is the energy of an electron at rest in the vacuum; $\chi_{eff} \equiv E_0 - E_c$ is the effective (negative) electron affinity; E_F is the Fermi level; ϕ_s (ϕ_m) is the work function of the GaAs source (metal electrode); e is the electron charge; ΔV is the accelerating voltage; $\bar{E}_e$ is the mean energy of the electron beam; ΔE_e is the energy spread of the electron beam; $\overline{\delta E_t}$ ($\overline{\delta E_b}$) is the mean energy loss in bulk thermalization (in the band-bending region).

Turnbull and Evans (1968) found that the quantum efficiency was greatly enhanced by alternately applying layers of Cs and O_2 to the surface, a process that has since become

known as *yo-yo activation*. Sonnenberg (1971) obtained better results by simultaneously applying the Cs and O_2 at rates such that the rate of increase of the photocurrent was maximized; however, he was working with a semiconductor with a bandgap smaller than that of GaAs.

The application of Cs has been achieved using either ions (Allen & Gobeli 1963; Weber & Cordes 1966; Kuskevics & Thompson 1966; Schaefer 1970; Madey & Yates 1971) or neutrals (Boutry, Évrard & Richard 1964; Eichenbaum & Moi 1964; Klein 1971; Smith & Huchital 1972). The ion methods preferentially coat the desired material by maintaining the substrate at a potential that is more negative than its environment; however, ion bombardment can damage the photocathode if the accelerating voltage is more than a few volts. Preferential coating by neutrals depends upon proximity and a directional beam. Ion methods also allow the rate of deposition to be roughly determined via the current necessary to neutralize the ions. Unfortunately, although all adsorbed ions are neutralized, the converse is not true. In most situations, however, the most important measure of the amount of deposition is the photo-yield, the determination of which is independent of the method of deposition.

Oxygen is usually stored in pressurized canisters and admitted to the UHV chamber either through a leak valve (Tang *et al* 1986) or by diffusion through heated silver (Whetten & Young 1959). The latter method can also be used to admit highly-purified oxygen using air as the source gas. Schaefer

(1970) developed a source in which the oxygen is stored as manganese dioxide powder in a silver tube. The entire source is mounted in the UHV chamber. When the tube is heated by an electrical current, the manganese dioxide releases oxygen which is then purified as it diffuses through the silver.

The quantum efficiency, Q, of an NEA photocathode depends upon five main design factors: (1) the mode of operation (transmission or reflection), (2) the choice of semiconductor, (3) the fabrication process, (4) the doping level and (5) the thickness of the activation layer (usually Cs-O).

For a given material, Q is greater in reflection mode than in transmission mode. In addition, reflection-mode photocathodes are also easier to construct because they need only one type of semiconductor, whereas transmission-mode photocathodes usually employ three or more different alloys. Transmission-mode photocathodes are used only in applications, such as image intensifiers, where geometrical constraints greatly favor their use. For these reasons, polarized-electron photocathodes are all operated in reflection mode.

As far as Q is concerned, the most important considerations when choosing a semiconductor material are (1) bandgap energy, E_g, and (2) minority-carrier diffusion length, L_D. A potential-energy barrier is formed at the interface between the semiconductor and the activation layer. If E_g is too small, the bottom of the conduction band, E_c, will be below the top of the potential barrier. Then thermalized electrons must tunnel through the barrier, thus decreasing Q.

Therefore, one should choose a semiconductor with large enough E_g so that E_c is above the barrier. Although L_D depends upon the fabrication process and doping level, as described below, in addition to the type of semicondutor, one should choose a material that maximizes L_D so that electrons excited deep within the semicondutor can diffuse to the surface before recombining.

The fabrication process affects Q via its effect upon L_D. Boat-grown wafers contain many defects which tend to reduce L_D and thus Q. Epitaxial layers grown on top of wafer substrates have fewer defects, and thus higher values of L_D and Q. Alvarado *et al* (1981) found that molecular-beam-epitaxial layers make better polarized-electron sources than do liquid-phase-epitaxial layers. The newest strained-layer polarized-electron sources (Alley *et al* 1995) are formed by the recently-developed metal-organic-chemical-vapor-deposition method.

NEA photocathodes are always doped p-type in order to maximize E_c relative to the Fermi level, E_F, and thus relative to the vacuum level, E_0. The more heavily doped the material is, the greater E_c becomes. In addition, the more heavily doped the material is, the narrower the band-bending region becomes, because the density of filled acceptor sites, and thus the space charge, increases. This latter effect is desirable for two reasons: (1) electrons generated in the band-bending region have less energy than electrons generated in the bulk, and (2) electrons generated in the bulk can lose

energy via collisions with phonons in the band-bending region. These lower-energy electrons cannot escape into the vacuum. Unfortunately, L_D decreases as the doping level increases. Therefore, as the doping level is increased, Q first increases, but reaches a maximum and then decreases.

The thickness, L_a, of the activation layer affects Q in two ways: as L_a increases (1) the work function, ϕ_s, decreases thus increasing the effective NEA, χ_{eff}, and (2) the scattering of electrons in the activation layer increases. Therefore, Q reaches a maximum at a finite thickness of the activation layer.

An additional important factor affecting Q is the cleanness of the emitting surface (Uebbing 1970). Most contaminants can be removed prior to activation by heating the crystal just below its congruent evaporation temperature (627°C for GaAs); unfortunately, carbon compounds are not removed at this temperature. Q decreases linearly with the amount of carbon contamination, dropping to zero at approximately one monolayer of carbon. An alternate approach to obtaining a clean surface is to cleave the crystal in ulta-high vacuum (UHV). In either case, the maintenance of a clean surface requires UHV at least at the level of 10^{-10} Torr with special care taken to minimize the amount of carbon in the chamber.

In order to use a semiconductor photocathode as a source of *polarized* electrons, it is necessary to preferentially pump electrons of one spin into the conduction band. This pumping

is accomplished by means of circularly-polarized light in a process which is similar to the Fano effect except that the arrangement of states is inverted: in the Fano effect, the upper (continuum) states are split by the spin-orbit interaction; in semiconductors, spin-orbit coupling splits the lower states (at the edge of the valence band) (see Figure 1.2).

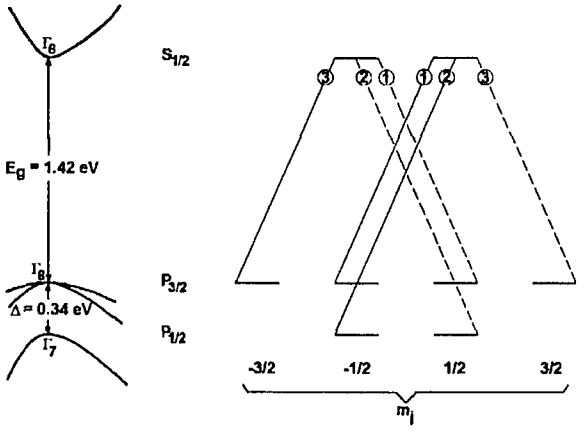

Figure 1.2 The band structure of GaAs at 300 K near the center of the Brilloin zone (left) and the equivalent atomic states at the Γ symmetry point ($\boldsymbol{k}$ = 0) (right). The subscripts of Γ indicate the symmetry of $\boldsymbol{k}$ at each point. The transitions indicated by solid (dashed) lines are for σ^+ (σ^-) polarization of the incident photons. The encircled numbers indicate the relative transition probabilities (Roth, Lax & Zwerdling 1959).

The first theoretical investigation of spin-orbit splitting in semiconductors with zinc-blende structures was carried out by Dresselhaus (1955) who did not calculate numerical values, however. Local empirical pseudopotential calculations were reported by Zucca *et al* (1970); more accurate nonlocal empirical pseudopotential calculations were completed by Chelikowsky and Cohen (1974, 1976). The first

Table 1.1 Luminescence studies of polarized conduction bands.

SEMICONDUCTOR	REFERENCES[1]
Si	Lampel (1968)[2]
GaSb	Parsons (1969, 1971) Hermann & Lampel (1971)
GaAlAs	Ekimov & Safarov (1970, 1971a, 1972a,b) Garbuzov, Ekimov & Safarov (1971) Dzhioev *et al* (1972) Berkovits, Ekimov & Safarov (1974) Weisbuch & Lampel (1974)
GaAs	Zakharchenya *et al* (1971) Dzhioev *et al* (1972) Garbuzov *et al* (1972)

Notes: (1) Only papers published before the proposal of Garwin, Pierce & Siegmann (1974) are listed.
(2) NMR, rather than luminescence, was used to determine the degree of polarization of the conduction band.

investigation of the effects of spin-orbit splitting upon interband transitions induced by circularly-polarized light was conducted by Burstein *et al* (1959) who were studying the band structure of Ge by means of interband magneto-optical measurements. They did not measure the degree of polarization of the excited electrons, however. The polarization of conduction bands produced by circularly-polarized light has been measured by the resulting luminescence (see Table 1.1). In all of these studies, the focus was upon the properties of semiconductors. The possible applications of these materials and processes in sources of polarized electrons were not considered.

Garwin, Pierce and Siegmann (1974) put the pieces together and suggested that an NEA GaAs photocathode with circularly-polarized incident light might be a compact, high-intensity source of polarized electrons. At about the same time, Lampel and Weisbuch (1975), working independently, reached the same conclusion. The first NEA GaAs photocathode used as a source of polarized electrons was developed at Zürich (Pierce, Meier & Zürcher 1975a,b; Pierce & Meier 1976).

The maximum possible polarization, P_{max}, of photoelectrons from III-V semiconductors is 50% when the energy, $h\nu$, of the exciting photons equals E_g (see Figure 1.2). The actual polarization, P, is less than 50% for several reasons. First, spin-lattice relaxation reduces the polarization, P_{th}, of the thermalized electrons relative to their polarization, P_0, when they initially become thermalized according to the following relationship (Pierce *et al* 1980):

$$P_{th} = \frac{\left(S + \sqrt{\frac{D}{\tau}}\right)(\alpha \cdot L_D + 1)}{\left(S + \sqrt{\frac{D}{T}}\right)\left(\alpha \cdot L_D + \sqrt{1 + \frac{\tau}{\tau_s}}\right)} P_0 \approx \frac{\alpha \cdot L_D + 1}{\alpha \cdot L_D + \sqrt{1 + \frac{\tau}{\tau_s}}} P_0, \qquad \textbf{(1.12)}$$

where S is the surface recombination velocity, D is the diffusion coefficient, τ is the lifetime of thermalized electrons, τ_s is the spin-lattice relaxation time, $\frac{1}{T} \equiv \frac{1}{\tau} + \frac{1}{\tau_s}$, $L_D \equiv \sqrt{D \cdot \tau}$ is the diffusion length, and α is the light absorption coefficient. The approximation holds for GaAs, for which $S \gg \sqrt{\frac{D}{T}} > \sqrt{\frac{D}{\tau}}$. The time τ_s decreases with increasing temperature while τ is essentially constant

(Garbuzov, Ekimov & Safarov 1971). The physical mechanisms for this relaxation include spin-exchange collisions with holes, spin-dependent recombination, and spin-orbit interactions with holes and charged impurities (Bir, Aronov & Pikus 1976). In addition, because the conduction-band states are not pure spin states, but contain a small admixture of the opposite spin, there is a small but perhaps significant probability that any spin-independent scattering that changes momentum can also lead to spin flip (Elliott 1954). Fleisher *et al* (1971) explain their measurements by assuming that both bulk and surface effects are significant; however, the results of Clark *et al* (1975, 1976) imply that surface effects are negligible, which is consistent with the approximation in (1.12).

Second, Q increases as $h\nu$ increases slightly above E_g because the density of states in the valence band increases as one moves away from the band edge. Unfortunately, P decreases simultaneously for two reasons (D'yakonov & Perel' 1971): (1) the polarization of the electrons promoted from the light-hole valence band immediately after promotion to the conduction band decreases with increasing $h\nu$ (the corresponding polarization of electrons promoted from the heavy-hole band remains constant at 50%) and (2) the energy relaxation (thermalization) of the electrons in the conduction band is accompanied by spin relaxation due to the spin-orbit splitting of the conduction sub-bands. The latter effect, which can be much greater than the former effect, can be understood as

arising from precession of the electron spin about an effective local magnetic field that is proportional to the cube of the momentum. Whenever the momentum changes, the direction of the effective field changes. The more rapidly the direction of the field changes, the less effective the spin relaxation becomes. Ekimov and Safarov (1971b) found that highly-doped samples maintained their spin orientation better than lightly-doped samples because the higher density of impurities increases the rate at which the momentum changes due to scattering. The quantum efficiency is adversely affected by increased doping, however, as discussed previously.

Third, exchange scattering by paramagnetic neutral Cs in the activation layer can lead to depolarization (Erbudak & Reihl 1978). All of the Cs is ionized on a surface treated with Cs but not O_2, and Cs^+ cannot depolarize via exchange scattering since it is not paramagnetic. Much of the Cs in a Cs-O activation layer is also ionized; however, some Cs is not ionized, and this fraction can depolarize via exchange scattering.

A final spin-relaxation mechanism is precession about an external magnetic field, $\boldsymbol{B}$, transverse to the momentum of the exciting photons (Parsons 1969); however, this mechanism is easily controlled. The effectiveness of this precession depends upon material, doping level and temperature. Zakharchenya *et al* (1971) used luminescence to measure $P(B)$ at 77 K in a GaAs sample doped to a hole density of 2×10^{19} cm^{-3}.

Their measurements show that significant depolarization does not occur until B is of the order of 100 G. The critical value of B increases as temperature increases.

The reader may have noticed that the published reports describing the previously-discussed types of polarized-electron sources stop in the early 1980s (with the exception of the helium- discharge source at Orsay). The vast majority of polarized-electron sources in use since then have used photoemission from semiconductors. Moreover, the number of polarized-electron sources in use has increased rapidly due to the relative low cost and ease of construction and operation of the semiconductor-based sources.

The first GaAs sources were cleaved in vacuum in order to obtain clean surfaces. The resulting surface plane is (110). In addition, most early sources were operated at liquid helium or liquid nitrogen temperatures in order to maximize both P and Q. Pierce, Wang and Celotta (1979) discovered that P was greater for photoelectrons emitted from (100) surfaces than for those emitted from (110) surfaces. Most GaAs sources since then have used (100) surfaces; however, a few since then have been either (110) or (111B) surfaces. (100) surfaces can be obtained by polishing. The resulting surfaces must be cleaned by etching and then heating in UHV before activation. Although P is greater at low temperatures than at room temperature, the lifetime is shorter due to contamination from cryopumping on the cathode surface (Sinclair 1981). In addition, room temperature sources are less expensive and

easier to build and operate than cooled sources. For these reasons, most sources are now operated at room temperature; although some are still cooled when higher P is critical.

The operating GaAs polarized-electron sources that have been reported in the literature are listed in Table 1.2; sources using tertiary alloys are listed in Table 1.3. More information is included in the former, because the present experiment employs a GaAs source. It should be noted that the electronic band structure of the chalcopyrite alloys $ZnSiAs_2$ and $ZnGeAs_2$ differs qualitatively from the band structure of uniform zinc-blende alloys: the heavy-hole and light-hole bands of uniform zinc-blende alloys are degenerate at the Γ point (cf. Figure 1.2); the chalcopyrite band structure does not have this degeneracy. This degeneracy, which is responsible for limiting P_{max} to 50%, can be lifted by reducing the symmetry of a zinc-blende structure. Two methods have been used to reduce the symmetry: superlattices (see Table 1.4) and strained layers (see Table 1.5). Both methods allow P_{max} to be increased all the way to 100%. Superlattices incorporate alternating thin layers of two alloys with different band gaps; strained layers are formed by creating a heterojunction between two alloys with slightly different lattice constants.

Table 1.2 GaAs polarized-electron sources.[1]

LOCATION	FACE	T (K)	DOPING[2] (10^{19} cm^{-3})	REFERENCES
Zürich	(110)	≤10 30 300	1.3	Pierce *et al* (1975a,b) Pierce & Meier (1976) Allenspach *et al* (1984)
SLAC	(100)	LN_2	?	Sinclair *et al* (1976) Prescott *et al* (1978) Sinclair & Miller (1981) Sinclair (1981, 1985)
Zürich	(110)	77	1 5	Erbudak & Reihl (1978) Reihl *et al* (1979)
NBS	(100)	77 110 300	5.6	Pierce *et al* (1979, 1980) Fiegerle *et al* (1984)
Jülich	(100) (110) (111)	300	0.6-4[3] ?	Alvarado *et al* (1981) Campagna *et al* (1982)
Bates	(100)	LN_2	0.5-2	Souder *et al* (1983) Cates *et al* (1989)
Palaiseau	(100) (110)	110 115 120 300	0.13 0.7-1.6 ~1	Drouhin *et al* (1983) Drouhin *et al* (1985a,b) Drouhin & Eminyan (1986) Riechert *et al* (1988)
Nagoya	(100)	LN_2	0.37 2.3	Nakanishi *et al* (1986)
Münster	(100)	300	2.5(1.1)	Luig *et al* (1986)
CCNY	(100)	300	1.6	Tang *et al* (1986) Guo *et al* (1990a)
München	(100)	300	3.8	Kolac *et al* (1988)
USA[4]	(100)	300	0.5[3]	Maruyama *et al* (1989)
Perth	(110)	300	2.2	Ranganathaiah *et al* (1990)
Milano	?	?	~1	Ciccacci *et al* (1994)

Notes: (1) The values are listed in increasing order. See the references for the correlation between values in different columns.
(2) The dopant is Zn unless otherwise indicated.
(3) Be-doped, molecular-beam-epitaxy-grown sample.
(4) Madison/SLAC/CEBAF/Champaign/Urbana.

Table 1.3 Tertiary-alloy polarized-electron sources.

LOCATION	ALLOYS	REFERENCES
Zürich	$ZnSiAs_2$ $ZnGeAs_2$	Zürcher & Meier (1979)
Mainz	$GaAs_{1-x}P_x$ (1)	Conrath *et al* (1979) Reichert & Zähringer (1982) Reichert (1983)
Jülich	$Al_xGa_{1-x}As$ (2)	Ciccacci *et al* (1982) Campagna *et al* (1983)
Jülich	$GaAs_{0.6}P_{0.4}$	Kirschner *et al* (1983)
Leningrad	$GaAs_{0.64}P_{0.36}$	Yashin *et al* (1987)
Europe (3)	$Al_{0.3}Ga_{0.7}As$ (4)	Ciccacci *et al* (1988)
München	$GaAs_{0.6}P_{0.4}$	Kolac *et al* (1988)
Europe (5)	$Al_{0.3}Ga_{0.7}As$	Ciccacci *et al* (1989)
Tübingen	$GaAs_{0.6}P_{0.4}$	Mergl *et al* (1991)
USA (6)	$Al_xGa_{1-x}As$ (4,7)	Maruyama *et al* (1993)

Notes: (1) $x \in \{0, 0.38, 0.65, 0.87, 1.0\}$.
(2) $x \in \{0.08, 0.15, 0.25, 0.32, 0.37, 0.50, 0.58, 0.65\}$
(3) Rome/Paiaiseau/Bagneux.
(4) Covered by a thin epilayer of GaAs.
(5) Milano/Palaiseau/Lausanne.
(6) SLAC/Madison/Berkeley.
(7) $x \in \{0, 0.05, 0.10, 0.15\}$.

Table 1.4 Superlattice polarized-electron sources.

LOCATION	ALLOYS	REFERENCES
SLAC	GaAs/AlGaAs	Sinclair (1981, 1985)
Jülich		Alvarado *et al* (1981) Campagna *et al* (1983)
France/USA[1]		Houdré *et al* (1985)
Europe[2]		Ciccacci *et al* (1988)
Japan[3]		Omori *et al* (1991)
USA[4]	GaAs/AlAs	Maruyama *et al* (1993)
Japan[3]	GaAs/InGaAs[5]	Omori *et al* (1994)
Japan/USA[6]	GaAs/AlGaAs	Kurihara *et al* (1995)

Notes: (1) Palaiseau/Limeil Brévannes/Bell Labs.
(2) Rome/Palaiseau/Bagneux.
(3) KEK/Nagoya/NEC.
(4) SLAC/Madison/Berkeley.
(5) This is a strained-layer superlattice.
(6) KEK/Nagoya/NEC/SLAC.

Table 1.5 Strained-layer polarized-electron sources.

LOCATION	SUBSTRATE	ACTIVE LAYER	REFERENCES
USA[1]	GaAs	InGaAs	Maruyama *et al* (1991)
Japan[2]	GaAsP	GaAs	Nakanishi *et al* (1991) Aoyagi *et al* (1992) Saka *et al* (1993)
USA[3]			Maruyama *et al* (1992)
SLAC			Schultz *et al* (1994) Alley *et al* (1995)

Notes: (1) SLAC/Madison/Berkeley.
(2) Nagoya/Sakai/Toyota/Daido Steel/Tokyo.
(3) SLAC/Madison.

7. Mott polarimetry

Although several types of electron-spin polarimeters are in use (Kessler 1985), only gold-foil Mott polarimetry is described here because the polarization of the electron beam used in the present experiment was determined by comparison with the results of Fletcher *et al* (1985) who used a gold-foil Mott polarimeter to determine the polarization of their electron beam. Mott polarimetry has been reviewed by Gay and Dunning (1992).

As mentioned previously, Mott (1929, 1932) not only showed that an electron beam can be polarized by accelerating it to relativistic velocities and scattering it at large angles from a high-Z target, but also that the polarization of an electron beam can be determined by measuring the asymmetry in the scattering at large angles from a high-Z target if the beam is accelerated to relativistic velocities. He concentrated on the specific case of scattering from a thin gold foil. The first successful use of Mott polarimetry was by Shull, Chase and Myers (1943). As mentioned previously, many previous attempts at Mott polarimetry were overwhelmed by instrumental errors. These instrumental effects will now be discussed after a brief overview of the basic principles of gold-foil Mott polarimeters.

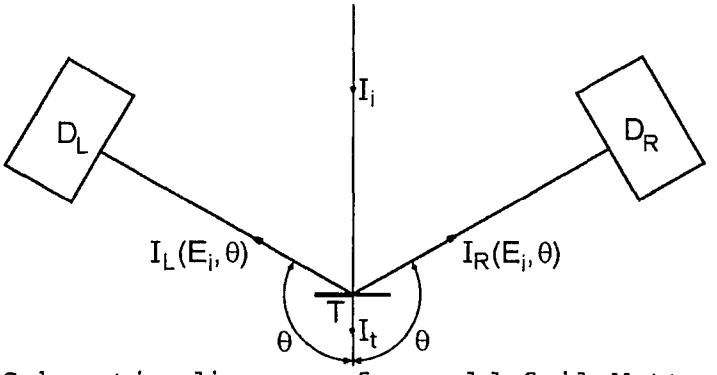

Figure 1.3 Schematic diagram of a gold-foil Mott polarimeter showing the gold-foil target, T, the electron detectors, D_L and D_R, the scattering angle, θ, the incident electron current, I_i, the transmitted current, I_t, and the scattered currents, $I_L(E_i, \theta)$ and $I_R(E_i, \theta)$. E_i is the energy of the electrons in the incident beam. The entire system is planar. The target scatters electrons in all directions; however, only electrons scattered in the directions shown are detected.

Figure 1.3 is a schematic diagram of a gold-foil Mott polarimeter. The detectors measure the scattered currents, $I_L(E_i, \theta)$ and $I_R(E_I, \theta)$. The polarization, $\boldsymbol{P}_e$, of the electron beam is related to the asymmetry, $A_M(E_i, \theta)$, in single elastic scattering as follows (Gay & Dunning 1992):

$$A_M(E_i, \theta) \equiv \frac{I_L(E_i, \theta) - I_R(E_i, \theta)}{I_L(E_i, \theta) + I_R(E_i, \theta)} = S(E_i, \theta)\,\boldsymbol{P}_e \cdot \hat{\boldsymbol{n}}, \qquad (1.13)$$

where $S(\theta)$ is known as the Sherman function (Sherman 1956), and $\hat{\boldsymbol{n}}$ is a unit vector normal to the scattering plane defined by

$$\hat{\boldsymbol{n}} \equiv \frac{\boldsymbol{p}_i \times \boldsymbol{p}_L}{|\boldsymbol{p}_i \times \boldsymbol{p}_L|}, \qquad (1.14)$$

where $\boldsymbol{p}_i$ ($\boldsymbol{p}_L$) is the momentum of the electrons in the incident (scattered) beam. Note that only the component of $\boldsymbol{P}_e$ normal

to the scattering plane is determined by this method. Additional information can be gleaned by arranging two additional detectors in a plane orthogonal to the first plane; however, the longitudinal component of P cannot be determined by Mott scattering. Inclusion of a variable spin rotator, such as a Wien filter, before the polarimeter allows the complete determination of $\boldsymbol{P}_e$. Typical values of the design parameters are E_i = 100 keV and θ = 120°, because S has a maximum there (Motz, Olson & Koch 1964). The scattering cross section decreases with increasing energy, while at lower energies multiple and plural scattering (see below) become more problematic (Gay & Dunning 1992).

Although the basic principles of Mott polarimetry are very simple, many complications arise. First, the description thus far has assumed that each electron scatters off just one nucleus; however, scattering from a gold foil includes both plural scattering (scattering a few times at relatively large angles) and multiple scattering (scattering many times at small angles), both of which reduce the asymmetry. This problem, recognized early on by Mott (1932), can be corrected by using several foils of different thicknesses and extrapolating the asymmetry to zero thickness; however, a residual error results because the functional relationship between the asymmetry and the target thickness is not known exactly, and different functions lead to different extrapolations (Gay & Dunning 1992). A detailed Monte-Carlo

analysis of the effects of multiple and plural scattering on Mott polarimetry has recently been carried out (Khakoo 1995).

A second complication is that most of the scattering is inelastic. A retarding potential reduces the detection of inelastically-scattered electrons; however, a compromise must be reached between energy discrimination and signal strength. Improvements in discrimination reduce systematic error, while increases in signal decrease random error.

A third complication is instrumental asymmetries due to misalignment of the beam, inhomogeneities in the beam and the foil, asymmetrical positioning of the detectors, and differences in the detector efficiencies. In the case of polarized electrons generated by the absorption of circularly-polarized light (e.g., Fano-effect sources or semiconductor sources), these instrumental asymmetries can be corrected (Gay & Dunning 1992) by reversing the helicity of the photons and thus the polarization of the electrons.

A fourth complication is scattering from the substrate onto which the foils are evaporated. This problem can be corrected by scattering the electrons off a blank substrate; however, a residual error results from variations between different samples of the substrate.

Additional complications are dark current in the detectors; electronic noise; electrons that scatter off other surfaces, such as chamber walls, into the detectors; sputtered ions; and photons generated by electrons striking the target.

B. Polarized Atomic-Hydrogen Beams

Hydrogen was isolated as early as the 16th century by Paracelsus, but it was confused with other inflammable gases until 1766 when Cavendish recognized it as a distinct substance. The name "*hydrogen*", which is neo-Greek for "*water former*", was first applied by Lavoisier in 1781 (Jolly 1974). The natural form of elemental hydrogen is the diatomic gas H_2.

An atomic-hydrogen-beam source must perform at least two functions: dissociation of the molecules and formation of a beam. Additional processes in some sources are purification of the molecular gas, excitation of the atoms, and polarization of the atomic electron or the nucleus. The discussion is divided into two main sections: the first describes methods of dissociation and beam formation; the second describes methods for obtaining a polarized beam. Only atomic beams are considered: polarized-proton beams are not discussed.

1. Methods of dissociation and beam formation

Three basic types of atomic-hydrogen-beam sources have been reported in the literature: Wood's tubes, tungsten ovens and rf-discharge tubes. These types are described in the next three sections. The emphasis is upon the development of the technologies, only: no attempt is made to identify all reported applications of the technologies.

a. Wood's tubes

The first to report the development of an atomic-hydrogen-beam source was Wood (1922a,b) of Johns Hopkins

University who modified a discharge tube he designed for spectroscopic studies. He used a long, glass discharge tube because the electrodes acted as catalysts for recombination of hydrogen. By separating the electrodes by 1-2 m, the central region can be maintained highly dissociated. The use of purified (dry) hydrogen for prolonged periods leads to a drastic decrease in the level of dissociation due to recombination on the surface of the tube. Oxygen or water vapor added to the tube "poisons" the walls (decreases the rate of recombination), thereby allowing a high level of dissociation to remain indefinitely. Wood added a tube extending perpendicular to the central region of the discharge and connected a vacuum pump to draw atomic hydrogen into the tube. Phipps and Taylor (1927) of the University of Illinois added a series of three glass slits to better define a beam. Metal slits were not used because they catalyzed too much recombination. While the exit slit of the tube is invariably glass, metal slits are often used at other positions in the beam line (see, for example, Rabi, Kellogg & Zacharias 1934). Phipps and Taylor (1927) also measured the temperature in the discharge to be ~700 K.

b. tungsten ovens

Later in the same year as Wood's announcement, Compton (1922) and Duffendack (1922) (cf. Olmstead & Compton 1923) reported the development at Princeton of a tungsten oven for dissociating hydrogen and other diatomic gases. The main element of the oven is a sheet of tungsten rolled into a

cylindrical tube. When the tube is heated to ~3000 K by passing an electrical current through it, hydrogen at pressures up to several Torr is almost completely dissociated. These atoms then exit through an open end of the tube. Lamb and Retherford (1950) of Columbia altered the design to improve the collimation of the atomic beam. They admitted hydrogen into the tungsten tube via another tube connected to one end. The dissociated hydrogen exited through a slit in the tungsten tube rather than through the end of the tube. They further improved the oven (Lamb & Retherford 1951; cf. Hendrie 1954) by constructing it from a solid cylinder rather than from a rolled sheet. Phipps and Taylor (1927), in addition to employing a Wood's-tube source, used a variation of the tungsten oven. They used a hot tungsten filament, rather than a tube, to dissociate hydrogen. The filament, located within 1 mm of the exit slit of a hydrogen-filled chamber, was wound into a coil and heated to ~2800 K by passing an electrical current through it.

c. rf-discharge tubes

In early discharge tubes, such as Wood's tubes, electrical energy is transferred to the gas via electrodes within the gas. Thomson (1891, 1927) discovered that electrical energy can also induce a discharge without the use of electrodes in the gas. The tube containing the gas is surrounded by a coil in which rf electrical oscillations are induced.

Kunz and Tykociner (1929) of the University of Illinois reported at the 1928 Minneapolis meeting of the APS that they had developed an atomic-hydrogen-beam source based upon an rf discharge in a quartz bulb. Such a source is also mentioned in an abstract from a later APS meeting (Kunz 1933). Evidently, they never followed up their announcements with a full written report.

The next reported use of an rf-discharge atomic-hydrogen-beam source was by Nagle, Julian and Zacharias (1947) of MIT. They did not describe the source in that paper, however, except to say that it was "appropriate to atomic hydrogen". A very brief description of the source is included in a later report (Davis *et al* 1949) from the same laboratory where it was applied to form an atomic-chlorine beam. The glass tube is mounted in a resonant cavity and cooled by an air blast.

Thonemann *et al* (1948) of Oxford developed an rf-discharge source for hydrogen and deuterium atomic ions. The discharge volume is a pyrex tube around which a coil is wrapped. The source is cooled by an air blower.

Risler *et al* (1974) used a source based upon a design by Keller (1957). The hairpin-shaped pyrex discharge volume is immersed in a bath of ciculating cooling fluid (Dow Corning DC-200 Siliconoil 5cSt). Each of the two branches of the tube is surrounded by a cylindrical electrode through which rf power is delivered.

In the sources developed by Ding, Karlau and Weise (1977), Murphy and Brophy (1979) and Slevin and Stirling

(1981) the discharge tube is mounted in a resonant cavity. In the first two sources, the rf power is connected to the cavity; in the last source, the power is delivered to a coil wrapped around the tube. The first source uses a quartz tube cooled by flowing silicon oil; the second source uses a vycor tube cooled by a combination of flowing ice water and flowing compressed air; the third source uses a pyrex tube cooled by flowing water.

The sources are cooled for several reasons: to prevent damage (cracking, melting, etc.) of system components due to overheating; to reduce recombination on the inner surface of the discharge tube; and to reduce the velocity of the beam, thereby increasing its density. Several liquid-helium-cooled sources have been developed to maximize this last benefit. Belushkina *et al* (1976) cool their discharge tube directly. In the other sources (Walraven & Silvera 1982; Hershcovitch, Kponou & Niinikoski 1987; Singy *et al* 1990), the disharge operates at room temperature and the exit nozzle is cooled.

2. Polarization methods

Three basic methods have been developed to generate polarized atomic-hydrogen beams. All three methods use state selection in a magnetic field. The first two methods, deflecting magnets and multipole magnets, use inhomogeneous fields to state select ground-state beams. The major difference between these methods is that in the former, the deflection of each atom is unidirectional while in the latter, atoms in the selected states oscillate in the field. The

third method, motional Stark quenching, uses a homogeneous field to state select metastable (2S) beams. These technologies have often been applied to the production of polarized-proton beams which are not the focus of this discussion; therefore, no attempt is made at an exhaustive listing of applications.

a. deflecting magnets

Phipps and Taylor (1927) were the first to investigate the polarizability of hydrogen using a Stern-Gerlach magnet (Gerlach & Stern 1922). The basic principle behind state selection in a Stern-Gerlach magnet, as well as in the other types of deflecting magnets described in this section and the multipole magnets described in the next section, is the interaction between the magnetic moment, μ, of the atom and the gradient of the magnetic field, B. The atoms experience a force, F, given by

$$F = \nabla(\mu \cdot B) . \qquad (1.15)$$

If μ is independent of B, F can be written as

$$F = \mu_{eff} \nabla B \qquad (1.16)$$

where the effective magnetic moment, μ_{eff}, is the component of μ along B. Atoms in different quantum states have different effective magnetic moments, and therefore experience different deflecting forces. In a high field, a ground-state hydrogen beam is separated into two beams according to electronic spin states. A polarized beam is then obtained by selecting one of these beams. If the beam then enters a low-field region,

hyperfine coupling reduces the degree of polarization of both the electrons and the protons.

Rabi, Kellogg and Zacharias (1934) of Columbia achieved a more uniform gradient by using two parallel "wires" carrying currents in opposite directions to generate a magnetic field. Another advantage of the two-wire deflector is that the field and its gradient can be calculated easily, and, therefore, the tedious job of measuring the gradient can be avoided. Because very high currents (~100 A) are necessary to generate the required fields, the two "wires" are in fact copper tubes which are cooled by water flowing through them.

A third type of deflector (Millman, Rabi & Zacharias 1938) (cf. Chapter Three, Section II.D.), also developed at Columbia, uses magnetic pole pieces in the shape of magnetic equipotential surfaces of the two-wire field. The resulting field is the same as for two wires, with the same uniformity of gradient. As with Stern-Gerlach magnets, "*two-wire*" magnets are generally electromagnets rather than permanent magnets. While "*two-wire*" magnets share most of the advantages of fields generated by two wires, the presence of magnetic materials makes the calculation of the field less accurate.

b. multipole magnets

Friedburg and Paul (1951) (cf. Friedburg 1951; Chapter Three, Section II.B) at Göttingen designed a magnet that not only state selected a neutral-atom beam, but also focused it, albeit with considerable chromatic aberration. The magnet has

six poles arranged in cylindrically symmetric positions with the poles alternating between north and south. The magnetic field, $\boldsymbol{B}$, inside this hexapole magnet is predominantly radial with $B \propto r^2$, where r is the radial distance from the axis of symmetry; therefore, $F \propto r$ [cf. (1.16)]. Atoms in states with $\mu_{eff} < 0$ experience a Hooke's law force and follow oscillatory trajectories; atoms in states with $\mu_{eff} > 0$ follow trajectories that either diverge from or converge to the axis of symmetry. Hexapole magnets were first used with atomic-hydrogen beams by Goldenberg, Kleppner & Ramsey (1960) at Harvard in the development of the hydrogen maser. Both electromagnets and permanent magnets have been used in constructing hexapole magnets.

Bennewitz and Paul (1954) at Bonn developed a quadrupole magnet to state select and focus neutral-atom beams. They added a velocity selector to minimize chromatic abberation. In a quadrupole magnet, $B \propto r$. Quadrupole magnets generally have low field strengths, in which μ_{eff} is constant for two of the hyperfine states of hydrogen while $\mu_{eff} \propto r$ for the other two hyperfine states. In each case, one of the states has $\mu_{eff} > 0$ while the other state has $\mu_{eff} < 0$. Therefore, atoms experience different forces in each of the four states, and atoms in a single hyperfine state can be selected. However, a sharp image requires the use of a velocity selector, which severely limits the intensity of the focused beam.

c. motional Stark quenching

Lamb and Retherford (1950) state selected a metastable ($2^2S_{½}$) hydrogen beam by motional Stark quenching. The beam was first dissociated in a tungsten oven, then excited by electron impact, and finally state selected by passage through a uniform transverse magnetic field, $\boldsymbol{B}$. An atom moving through the magnetic field experiences an electric field, $\boldsymbol{E} = \frac{\boldsymbol{v}}{c} \times \boldsymbol{B}$, in its rest frame. This electric field couples the $2^2S_{½}$ states to $2^2P_{½}$ states which then spontaneously decay to $1^2S_{½}$ states very quickly: the metastable atoms are quenched. The quenching rate depends upon the energy separation between the coupled states. The magnitude of the magnetic field was chosen such that the energy separation for the ($2^2S_{½}$, m = -½) state is zero, thereby maximizing the ratio $\frac{\tau_+}{\tau_-}$, where τ_+ (τ_-) is the lifetime of the m = +½ (-½) state. Later (Triebwasser, Dayhoff & Lamb 1953) a small electric field was added to quench the few remaining metastable atoms in the m = -½ state.

III. RELATED EXPERIMENTAL STUDIES

A brief history of experimental studies related to the present experiment is given. The specific areas discussed are electron-impact ionization, hydrogen scattering and spin asymmetries.

A. Electron-Impact Ionization

The earliest experimental investigations (e.g., Boucher 1922) of electron-impact ionization were limited to the determination of the ionization potential. Hughes and Klein (1924) were the first to measure energy spectra of relative total-ionization cross sections; Jones (1927) was the first to report an energy spectrum of absolute total-ionization cross sections.

Electron-impact ionization of many-electron targets can result in several different species of ions. Bleakney (1929) was the first to use q/m analysis to discriminate between these ionic species.

Funk (1930) was the first to use crossed beams of electrons and atoms to study electron-impact ionization. Boyd and Green (1958) and Fite and Brackmann (1958) introduced the technique of chopping the atomic beam in order to discriminate against ionization of the residual gas.

Lawrence (1926) was the first to conduct a detailed investigation of the near-threshold structure of a total ionization cross section. Fox *et al* (1951) introduced a retarding-potential analysis, especially useful in the near-threshold region, to determine the relative total-ionization cross section due to a narrow-energy-width portion of an electron beam. Other early investigations of near-threshold ionization are referenced in Foner and Nall (1961).

Mohr and Nicoll (1934) were the first to measure double-differential impact-ionization cross sections (i.e., they

measured the energy and direction of one of the two free electrons). In (e,2e) spectroscopy, one measures the momenta, via energy and direction, of the incident and both scattered electrons. This triple-differential cross section provides the most information possible with unpolarized beams. The method is used to determine the momentum distribution (i.e., the square of the amplitude of the momentum state function) of the atomic electron before it is ejected. The first relative (e,2e) measurements were performed by Amaldi *et al* (1969) and Ehrhardt *et al* (1969). Beaty *et al* (1977) reported the first absolute (e,2e) measurements.

Electron-impact ionization is reviewed by Kieffer and Dunn (1966) and Märk and Dunn (1985); (e,2e) spectroscopy is reviewed by Coplan, Moore and Doering (1994).

B. Electron-Hydrogen Scattering

The discussion of this section is limited to experimental studies of electron scattering from atomic hydrogen. The earliest such studies (Olmstead & Compton 1923, and references therein) were limited to determining the radiating and ionizing potentials, or in modern parlance, the threshold energies for inelastic excitation and ionization. Harnwell (1929) was the first to report relative cross sections, measuring double-differential (resolving the energy and direction of the scattered electrons) cross sections at incident-electron energies of 120 and 180 eV. The more recent cross-section measurements are listed in Table 1.6. In

Table 1.6 Electron-hydrogen cross-section measurements.

CHANNEL[1,2]		ENERGY RANGE (eV)	LOCATION	REFERENCES
1s → ?[3]	rA	4 - 12.5	NYU	Bederson *et al* (1957)
		3.1 - 12.3	General Dynamics	Neynaber *et al* (1961)
1s → 1s		1 - 10		Brackmann *et al* (1958)
	rS	3.8 - 9.4		Gilbody *et al* (1961)
		9.4 - 200	Flinders	Teubner *et al*(1973,1974) Lloyd *et al* (1974)
	aS	0.5 - 680	Belfast	Williams (1974,1975a,b)
1s → 2[4]		11.6-54.4		Williams (1976, 1981)
1s → 2s	rA	10.2 - 700	General Dynamics	Fite *et al* (1958b,1959a)
		10.2 - 600		Stebbings *et al* (1960)
		10.2 - 1k	Pittsburgh	Kauppila *et al* (1970)
		10.2-12.3	Stirling	Koschmieder *et al* (1973)
	aA	10.2-54.4	Belfast	Williams (1976, 1981)
1s → 2p				Williams & Willis (1974) Williams (1976, 1981)
	rS	40 - 100	Flinders	Hood *et al* (1979) Weigold (1980) Weigold *et al* (1980)
		35 - 100	Stirling	Slevin *et al* (1980,1982)
1s → Ion	rA	13.6 - 1k	General Dynamics	Fite & Brackmann (1958a) Rothe *et al* (1962) McGowan & Clarke (1968)
		14.6 - 4k	Belfast	Shah *et al* (1987)
		17.5 - 600	Bielefeld	Spicher *et al* (1990)
	rD	25 - 250	Ann Arbor	Shyn (1992)
	rT	100 - 1.2k	Flinders	Weigold *et al*(1977,1979) Weigold (1980) Lohmann & Weigold (1981) McCarthy *et al* (1989)
		4	Kaisers-lautern	Schlemmer *et al* (1989)
2s → Ion	rA	8.5 - 499	Oxford	Dixon *et al* (1975)
		6.3 - 998	Belgium	Defrance *et al* (1981)

Notes: (1) a = absolute, r = relative, A = angle-integrated, S = single-differential (angle), D = double-differential (angle and energy), T = triple-differential (e,2e).
(2) Cross sections are labeled relative if "*absolute*" cross sections are obtained by normalizing to another absolute cross section.
(3) Total cross section (elastic below 10.2 eV).
(4) The angular momentum is not resolved in these experiments.

addition to cross sections, electron-hydrogen scattering experiments have been used to measure the lifetime of the metastable 2s state (Slack 1926; Fite *et al* 1959b) and the polarization of Lyman-alpha radiation (Ott, Kauppila & Fite 1967, 1970) which indicates the relative cross sections for the different magnetic sublevels.

C. Spin Asymmetries

After an introduction to the theory of spin asymmetries, the reported measurements of spin asymmetries in electron-atom scattering are reviewed with special emphasis upon electron-hydrogen scattering.

1. Theory[4]

First-generation atomic-physics experiments use unpolarized incident particles and do not measure the spin of the scattered particles. Second-generation experiments employ two polarization devices: either polarized incident beams or polarimeters. The six nonreactive second-generation experiments with a single spin-quantization axis allow the determination of three spin asymmetries (see Figure 1.4).

---

[4]This section borrows heavily from Lubell (1980).

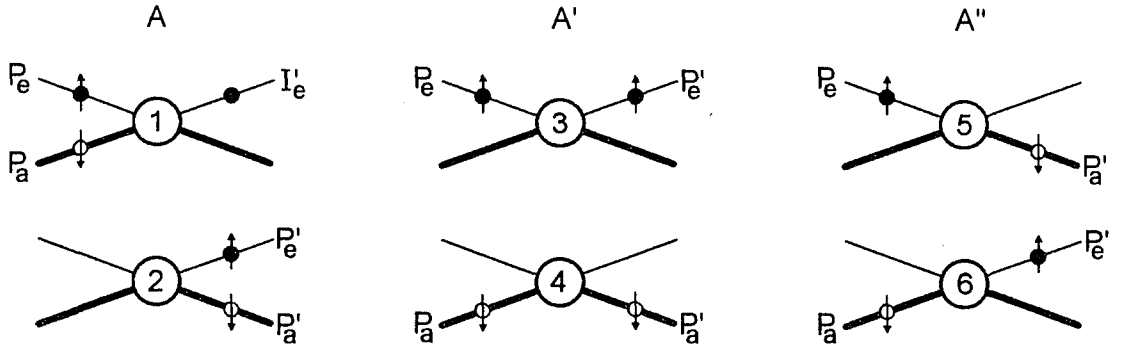

Figure 1.4 Schematic diagrams of the six nonreactive second-generation scattering experiments with a single spin-quantization axis. Particles are incident from the left with electrons (atoms) indicated by thin (thick) lines. The central circle represents the interaction region. The number in this circle denotes the type of experiment. The smaller solid (open) circles indicate measured electron (atomic) beams with the measured quantities denoted by P_e for electron polarization, P_a for atom polarization and I_e for electron current. Primed quantities are measured in the outgoing channels. The asymmetries A, A' and A'' are defined in the text.

Both type-1 and type-2 experiments determine the asymmetry, A, defined by

$$A \equiv \frac{\sigma(\uparrow\downarrow) - \sigma(\uparrow\uparrow)}{\sigma(\uparrow\downarrow) + \sigma(\uparrow\uparrow)} \qquad (1.17)$$

[cf. (1.1)], where $\sigma(\uparrow\downarrow)$ [$\sigma(\uparrow\uparrow)$] is the cross section with the electron and atom spins antiparallel [parallel]. If all non-exchange spin-flip mechanisms (e.g., spin-orbit interaction) can be neglected, A is related to the direct, f, and exchange, g, scattering amplitudes (cf. Table 1.7) by

$$A = \frac{Re\{f^*g\}}{\bar{\sigma}} = \frac{|f||g|\cos\theta}{\bar{\sigma}}, \qquad (1.18)$$

where θ is the relative phase between f and g, and the spin-averaged cross section, $\bar{\sigma}$, is given by

Table 1.7 Polarization processes and cross sections.

PROCESSES[1]		CROSS SECTION[2]
$e\uparrow + A\downarrow \rightarrow e\uparrow + A\downarrow$	$e\downarrow + A\uparrow \rightarrow e\downarrow + A\uparrow$	$\lvert f\rvert^2$
$e\uparrow + A\downarrow \rightarrow e\downarrow + A\uparrow$	$e\downarrow + A\uparrow \rightarrow e\uparrow + A\downarrow$	$\lvert g\rvert^2$
$e\uparrow + A\uparrow \rightarrow e\uparrow + A\uparrow$	$e\downarrow + A\downarrow \rightarrow e\downarrow + A\downarrow$	$\lvert f - g\rvert^2$

Notes: (1) The arrows indicate the spin orientations of the electron, e, and the atom, A.
(2) All non-exchange spin-flip mechanisms (e.g., spin-orbit interaction) are neglected.

$$\bar{\sigma} = \frac{1}{2}\sigma^{\uparrow\uparrow} + \frac{1}{2}\sigma^{\uparrow\downarrow} = \frac{1}{2}|f|^2 + \frac{1}{2}|g|^2 + \frac{1}{2}|f - g|^2 . \quad \textbf{(1.19)}$$

In some experiments, excitations to several nearly-degenerate states are unresolved. The measured asymmetry then depends upon several independent direct and exchange amplitudes.

The asymmetry, A', determined in type-3 and type-4 experiments is related to g and $\bar{\sigma}$ by[5]

$$A' = 1 - \frac{|g|^2}{\bar{\sigma}} , \quad \textbf{(1.20)}$$

where A' is defined by

$$A' \equiv \frac{P_e'}{P_e} \quad \textbf{(1.21)}$$

for a type-3 experiment, and by

[5]As with (1.18), these expressions neglect all non-exchange spin-flip mechanisms. Again, if excitations to several nearly-degenerate states are unresolved, the expressions for the measured asymmetries in terms of direct and exchange amplitudes are more complicated.

$$A' \equiv \frac{P_a'}{P_a} \tag{1.22}$$

for a type-4 experiment; the asymmetry, A'', determined in type-5 and type-6 experiments is related to f and $\bar{\sigma}$ by[5]

$$A'' = 1 - \frac{|f|^2}{\bar{\sigma}}, \tag{1.23}$$

where A'' is defined by

$$A'' \equiv \frac{P_a'}{P_e} \tag{1.24}$$

for a type-5 experiment, and by

$$A'' \equiv \frac{P_e'}{P_a} \tag{1.25}$$

for a type-6 experiment. Only two of these asymmetries are independent as they are constrained by[6]

$$A + A' + A'' = 1. \tag{1.26}$$

The measurement of $\bar{\sigma}$ and any two of these asymmetries allows the separation of $|f|$, $|g|$ and $|\theta|$.

2. Electron-hydrogen

The first second-generation experiment was performed at Columbia by Lichten and Shultz (1959) who measured 1s-2s excitation of atomic hydrogen by electron impact in what was essentially a type-4 experiment. The ground-state hydrogen beam was dissociated in a tungsten oven and state-selected in

---

[6]This constraint results from (1.18), (1.20) and (1.23) and is subject to the same limitations.

a "*two-wire*" magnet. Metastable H(2s) atoms were generated by collisions with an unpolarized electron beam. These metastable atoms were then state selected by motional Stark quenching. Rather than measuring the polarizations of both the incident and scattered atoms, the cross section for generating H(2s, m = +½) atoms was measured separately for each of the two polarizations of the incident beam. From these cross sections they calculated

$$\frac{\sigma_-}{\sigma_+ + \sigma_-} = \frac{|g|^2}{2\sigma} = \frac{1}{2}(1 - A'), \qquad (1.27)$$

where σ_- (σ_+) is the cross section with the incident beam polarized in the m = -½ (+½) state.

All other reported measurements of electron-hydrogen spin asymmetries have been done under the direction of Michael Lubell. He and his collaborators have measured both elastic scattering at 90° and angle-integrated ionization in type-1 experiments. The research was begun at Yale in the mid 1970s and has continued at The City College of New York (CCNY) since the early 1980s.

Both ionization (Alguard *et al* 1977; Lubell 1980; Gay *et al* 1982) and elastic (Fletcher *et al* 1982) asymmetries were measured at Yale. The polarized-electron beam was generated by a DC Fano-effect source (Wainwright *et al* 1978); the polarized atomic-hydrogen beam was dissociated in a tungsten oven and state selected in a hexapole magnet. These measurements are summarized in Fletcher *et al* (1985) where

important corrections to the previously published results are discussed.

The ionization asymmetry was remeasured at CCNY (Crowe *et al* 1990) with special emphasis upon the near-threshold region (Guo *et al* 1990b). These measurements are the subject of this dissertation. The near-threshold measurements required a polarized-electron beam with a much smaller energy spread than the Yale source could generate. A GaAs photocathode (Tang *et al* 1986; Guo *et al* 1990a) amply met this criterion. The atomic-hydrogen source was also changed to an rf-discharge source (Slevin & Stirling 1981; Chan *et al* 1988) which increased the atomic density at the interaction region in addition to allowing for continuous operation.

3. Other electron-atom and electron-molecule

Second-generation electron-atom and electron-molecule scattering experiments have been reported with the following atomic and molecular species besides hydrogen: the alkalis lithium (Li), sodium (Na), potassium (K), rubidium (Rb) and cesium (Cs); the noble gases helium (He) and xenon (Xe); mercury (Hg), oxygen (O_2) and nitric oxide (NO) (see Table 1.8). In many of these experiments, excitations to several nearly-degenerate states were unresolved. In addition, the spin-orbit interaction is significant in experiments with the heavier species.

Table 1.8 Second-generation electron scattering experiments.

SPECIES	CHANNEL[1]	TYPE[2]	LOCATION	REFERENCES
H	D	$1^2S_{1/2} \rightarrow 1^2S_{1/2}$	1 Yale	Fletcher *et al* (1982, 1985)
	A	$1^2S_{1/2} \rightarrow 2^2S_{1/2}$	4 Columbia	Lichten & Schultz (1959)
		$1^2S_{1/2} \rightarrow$ Ion	1 Yale	Alguard *et al* (1977) Lubell (1980) Gay *et al* (1982) Fletcher *et al* (1985)
			CCNY	Crowe *et al* (1990) Guo *et al* (1990)
He	A	$2^3S \rightarrow$ Ion	1 Bielefeld	Baum *et al* (1989b)
Li	D	$2^2S_{1/2} \rightarrow 2^2S_{1/2}$	4 NYU	Bederson & Miller (1976)
			1 Bielefeld	Baum *et al* (1986)
	A&D	$2^2S_{1/2} \rightarrow 2^2P_{1/2,3/2}$		Baum *et al* (1989a)
	A	$2^2S_{1/2} \rightarrow 2^4P_{5/2}$ [3]		Baum *et al* (1988)
		$2^2S_{1/2} \rightarrow$ Ion		Baum *et al* (1981, 1985)
Na	D	$3^2S_{1/2} \rightarrow 3^2S_{1/2}$	4 NYU	Bederson & Miller (1976)
			1 NBS	McClelland *et al* (1987)
			3 Münster	Hegemann *et al* (1991)
	A	$3^2S_{1/2} \rightarrow 3^2P_{1/2,3/2}$	4 Bielefeld	Jitschin *et al* (1984)
				Baum *et al* (1985)
		$3^2S_{1/2} \rightarrow$ Ion	1 Stirling	Hils *et al* (1980, 1982)
			NBS	Kelley *et al* (1983)
	D	$3^2P_{3/2} \rightarrow 3^2S_{1/2}$		McClelland *et al* (1986,1989)
K	D	$4^2S_{1/2} \rightarrow 4^2S_{1/2}$	6 JILA	Hils *et al* (1972)
			4 NYU	Rubin *et al* (1960) Collins *et al* (1967, 1968, 1971) Bederson & Miller (1976)
		$4^2S_{1/2} \rightarrow 4^2P_{1/2,3/2}$		Rubin *et al* (1969) Goldstein *et al* (1972)
	A	$4^2S_{1/2} \rightarrow$ Ion	1 Stirling	Hils & Kleinpoppen (1978) Hils *et al* (1980)
			Bielefeld	Baum *et al* (1985)
		$4^2S_{1/2} \rightarrow$ Total	6 Edinburgh	Campbell *et al* (1971)
Rb	D	$5^2S_{1/2} \rightarrow 5^2S_{1/2}$	4 NYU	Jaduszliwer *et al* (1976)
Cs	A	$6^2S_{1/2} \rightarrow$ Ion	1 Bielefeld	Baum *et al* (1993)
Xe	D	Elastic	3 Münster	Wübker *et al* (1982)
Hg	D	$6^1S_0 \rightarrow 6^1S_0$	3 Münster	Berger *et al* (1981)
		$6^1S_0 \rightarrow 6^3P_{0,1,2}$		Hanne *et al* (1974, 1976a,b) Hegemann *et al* (1991)
O_2	A	Elastic	3 Rice	Ratcliff *et al* (1989)
NO	D		Münster	Hegemann *et al* (1991)

Notes: (1) A = angle-integrated, D = differential.
(2) Experiment type (see Figure 1.4).
(3) This is the autoionizing state $(1s2s2p)^4P_{5/2}$.

CHAPTER TWO: THEORY

The main focus of this chapter is a description of the convergent close-coupling (CCC) method of Bray and Stelbovics (1992, 1993). For introductory purposes, exact general scattering equations are discussed first. The chapter ends with a brief description of the recently published hidden-crossing theory of Macek, Ovchinnikov and Pasovets (1995). Throughout this chapter, the discussion is limited to electron-hydrogen scattering in order to keep the notation as simple as possible. Some of the equations in this chapter are discussed without being derived. The derivations of these equations can be found in any standard textbook on scattering theory; for example, Taylor (1972).

I. GENERAL CONSIDERATIONS

Exact non-relativistic scattering equations are developed for calculating the spin asymmetry. In Section II, an approximation method is discussed which allows the solution of the equations developed in this section.

A. Introduction & Definitions

The concepts of scattering channels, asymptotic states and singlet and triplet scattering are introduced. The scattering operator, the T matrix, scattering amplitudes, cross sections and the spin asymmetry are defined.

1. Scattering channels & asymptotic states

During a nonrelativistic collision between an electron and a hydrogen atom, the system may be considered to comprise the same three particles throughout the collision process: a proton and two identical electrons. Throughout this chapter, the initial state of the system is assumed to be an electron incident upon a stationary hydrogen atom in its ground state. The proton is modeled as remaining stationary at all times since it is much more massive than the electrons. The complications arising from the identity of the electrons are discussed in Section 4.

Throughout the collision, the state vector, $|\psi\rangle$, of the system develops according to the Schrödinger equation

$$\hat{H}|\psi\rangle = E|\psi\rangle, \tag{2.1}$$

where E is the energy of the system and the Hamiltonian operator, $\hat{H}$, is given by[7]

$$\hat{H} = \frac{\hat{\boldsymbol{p}}_1^2}{2m} + \frac{\hat{\boldsymbol{p}}_2^2}{2m} - \frac{e^2}{r_1} - \frac{e^2}{r_2} + \frac{e^2}{|\boldsymbol{r}_1 - \boldsymbol{r}_2|}, \tag{2.2}$$

where $\hat{\boldsymbol{p}}$ is the linear momentum operator, m is the mass of an electron, e is the elementary charge, $\boldsymbol{r}$ is the position of an electron relative to the proton, and the subscript *1* (*2*) refers to the incident (atomic) electron.

---

[7]Note that magnetic forces are not included in this model since they are insignificant at nonrelativistic energies.

Long before closest approach, the state of the system is indistinguishable from $|\psi_{in}\rangle$, known as the *"in asymptote"*, which is the solution to the Schrödinger equation

$$\hat{H}_1 |\psi_{in}\rangle = E|\psi_{in}\rangle, \tag{2.3}$$

where

$$\hat{H}_1 = \frac{\hat{\boldsymbol{p}}_1^2}{2m_1} + \frac{\hat{\boldsymbol{p}}_2^2}{2m_2} - \frac{e^2}{r_2} \tag{2.4}$$

is known as the channel Hamiltonian for the in channel, in which the interactions between the incident electron and ground-state hydrogen atom are negligible.

The situation long after the collision is similar but more complicated: the system has an infinite number of channels. The first channel, $|\psi_1\rangle$, is elastic scattering; the n^{th} channel, $|\psi_n\rangle$, is excitation to the n^{th} energy level; there is also the ionization channel, $|\psi_0\rangle$, which is of particular interest in the present study. The channel Hamiltonian for elastic scattering and excitation is $\hat{H}_1$ as for the in channel[8]; the channel Hamiltonian for ionization can be

$$\hat{H}_0 = \frac{\hat{P}_1}{2m} + \frac{\hat{P}_2}{2m}. \tag{2.5}$$

The most general form of the out asymptote, $|\Psi_{out}\rangle$, is the superposition state

---

[8]In the case of exchange scattering, r_2 is replaced by r_1.

$$|\Psi_{out}\rangle = \{|\psi_0\rangle, |\psi_1\rangle, |\psi_2\rangle, |\psi_3\rangle, \ldots\}, \qquad (2.6)$$

where the ψ_n are orthogonal but unnormalized. In this representation, the in asymptote, $|\Psi_{in}\rangle$, takes the form

$$|\Psi_{in}\rangle = \{0, |\psi_{in}\rangle, 0, 0, \ldots\}, \qquad (2.7)$$

where $|\psi_{in}\rangle$ is normalized.

2. Scattering operator, T matrix & scattering amplitudes

Since the time, t_{int}, during which the interactions between the incident electron and the hydrogen atom is significant is so short ($t_{int} \ll 1\ ps$), only the asymptotes are experimentally discernible. Theoretically, the asymptotes are connected by the scattering operator, $\hat{S}$, defined by

$$|\Psi_{out}\rangle \equiv \hat{S}|\Psi_{in}\rangle . \qquad (2.8)$$

Since it is possible that the out asymptote will be identical to the in asymptote, it is convenient to introduce a second operator, $\hat{R}$, which accounts for any change in the state of the system due to the interactions between the incident electron and the hydrogen atom. Thus, $\hat{S}$ is written as[9]

$$\hat{S} \equiv 1 + \hat{R}, \qquad (2.9)$$

and $|\psi_{out}\rangle$ becomes

$$|\Psi_{out}\rangle \equiv |\Psi_{in}\rangle + \hat{R}|\Psi_{in}\rangle . \qquad (2.10)$$

It is convenient to represent the state of the system in terms of its spectral decomposition into plane-waves which are simultaneously (improper) eigenvectors of the appropriate

---

[9]The notation is taken from Taylor (1972).

channel Hamiltonian and momentum operators. In the ionization channel, the plane waves are[10] $|\boldsymbol{p}_1, \boldsymbol{p}_2\rangle$; in all other channels, the plane waves are $|\boldsymbol{p}_1, \phi_n\rangle$ where the $|\phi_n\rangle$ are the orthonormal eigenvectors of the hydrogen atom with eigenenergies E_n. Thus the in asymptote is expanded as

$$|\psi_{in}\rangle = \int d^3p_1 \, \psi_{in}(\boldsymbol{p}_1)|\boldsymbol{p}_1, \phi_1\rangle, \tag{2.11}$$

the out asymptote in the ionization channel as

$$|\psi_0\rangle = \int d^3p_1 \int d^3p_2 \, \psi_0(\boldsymbol{p}_1, \boldsymbol{p}_2)|\boldsymbol{p}_1, \boldsymbol{p}_2\rangle \tag{2.12}$$

and in the other channels as[11]

$$|\psi_n\rangle = \int d^3p_1 \, \psi_n(\boldsymbol{p}_1)|\boldsymbol{p}_1, \phi_n\rangle. \tag{2.13}$$

To help simplify the notation, the plane waves for the ionization channel, $|\boldsymbol{p}_1, \boldsymbol{p}_2\rangle$, will be represented by $|\boldsymbol{p}_1, \phi_0\rangle$.

The T matrix, $T(\boldsymbol{p}_1', \phi_n \leftarrow \boldsymbol{p}_1, \phi_1)$, is defined in terms of the matrix elements of the scattering operator in the plane-wave representation as follows:

$$\langle \boldsymbol{p}_1', \phi_n | \hat{R} | \boldsymbol{p}_1, \phi_1 \rangle = -2\pi i \delta(E'-E) \, T(\boldsymbol{p}_1', \phi_n \leftarrow \boldsymbol{p}_1, \phi_1). \tag{2.14}$$

The T matrix differs from the more familiar scattering amplitude, $f(\boldsymbol{p}_1', \phi_n \leftarrow \boldsymbol{p}_1, \phi_1)$, by only a scale factor as follows:

---

[10]It should be noted that these plane waves are not orthogonal to the plane waves for the other channels. This lack of orthogonality can lead to complications in calculations.

[11]In the case of exchange scattering, $\boldsymbol{p}_1$ is replaced by $\boldsymbol{p}_2$.

$$f(\boldsymbol{p}_1', \phi_n \leftarrow \boldsymbol{p}_1, \phi_1) = -(2\pi)^2 m\, T(\boldsymbol{p}_1', \phi_n \leftarrow \boldsymbol{p}_1, \phi_1) . \qquad (2.15)$$

The reason for having both matrices is that the T matrix is very simply related to the scattering potential while the scattering amplitudes are more simply related to the scattering cross sections and the asymptotic form of the scattering state functions.

3. Scattering cross sections

The differential cross section, $\frac{\partial\sigma}{\partial\Omega}(\boldsymbol{p}_1', \phi_n \leftarrow \boldsymbol{p}_1, \phi_1)$, is proportional to the probability that an electron with initial momentum $\boldsymbol{p}_1$ incident upon a hydrogen atom in its ground state will have a final momentum of $\boldsymbol{p}_1'$ and excite the atom to the state $|\phi_n\rangle$. The differential cross section is related to the scattering amplitude and T matrix as follows:

$$\begin{aligned} \frac{\partial\sigma}{\partial\Omega}(\boldsymbol{p}_1', \phi_n \leftarrow \boldsymbol{p}_1, \phi_1) &= \frac{p_1'}{p_1} \left| f(\boldsymbol{p}_1', \phi_n \leftarrow \boldsymbol{p}_1, \phi_1) \right|^2 \\ &= (2\pi)^4 m^2 \frac{p_1'}{p_1} \left| T(\boldsymbol{p}_1', \phi_n \leftarrow \boldsymbol{p}_1, \phi_1) \right|^2 . \end{aligned} \qquad (2.16)$$

In the present experiment, the proton that results from ionization is measured irrespective of the directions of the momenta of the electrons. The relevant cross section is the total channel cross section, σ_n, which is the integral of the differential cross section over all solid angles:

$$\sigma_n \equiv \int d\Omega \, \frac{\partial\sigma}{\partial\Omega}(\boldsymbol{p}_1', \phi_n \leftarrow \boldsymbol{p}_1, \phi_1) . \qquad (2.17)$$

One other cross section of interest is the total cross section, σ, which is proportional to the probability that the

electron is scattered via any channel. The total cross section is simply the sum of the total channel cross sections:

$$\sigma \equiv \sum_{n=0}^{\infty} \sigma_n . \qquad (2.18)$$

4. Singlet & triplet scattering

The two electrons in the scattering system are identical Fermions, which means that the overall state function for the system must be antisymmetric according to the Pauli exclusion principle. Electrons have spin ½, and the two can combine as either a singlet (s = 0) or a triplet (s = 1). Table 2.1 shows the relationship between the coupled representation of singlet and triplet states and the uncoupled representation. As can be seen from the information in the table, the triplet states are symmetric in spin while the singlet state is antisymmetric; therefore, the spatial state functions for the triplet states must be antisymmetric while the spatial function for the singlet state must be symmetric.

Table 2.1 Properties of the triplet and singlet states.

TYPE	s	m_s	UNCOUPLED REPRESENTATION	SYMBOLIC REPRESENTATION
triplet	1	1	$\alpha(1)\alpha(2)$	↑↑
		0	$2^{-½}$ [$\alpha(1)ß(2)$ + $ß(1)\alpha(2)$]	↑↓ + ↓↑
		-1	$ß(1)ß(2)$	↓↓
singlet	0	0	$2^{-½}$ [$\alpha(1)ß(2)$ - $ß(1)\alpha(2)$]	↑↓ - ↓↑

The opposite spatial symmetry of the singlet and triplet states implies that the cross sections for the two types of states will differ. In particular, since the spatial state function for the triplet states is antisymmetric, the probability density of the incident electron is low near the proton where the probability density of the atomic electron is high. As a consequence, in singlet scattering, the incident electron approaches the charge center of the hydrogen atom more closely and therefore experiences a greater Coulomb interaction. Thus the cross section for singlet scattering, σ^s, is generally greater than that for triplet scattering, σ^t. Note that σ^t is the cross section for each of the triplet states. The cross sections for the three states are the same since the interactions are spin independent. The spin-averaged cross section, $\overline{\sigma}$, is therefore

$$\overline{\sigma} = \frac{1}{4}(\sigma^s + 3\sigma^t). \qquad (2.19)$$

An alternative procedure is to treat the two electrons as if they were distinguishable and calculate separate direct, f, and exchange, g, amplitudes. In the direct process, the incident electron is free in the out asymptote; in the exchange process, the electron initially bound in the atom ends up free in the out asymptote.

5. Spin asymmetry

The spin asymmetry, A_n, for a particular channel, n, is defined in terms of the cross sections with electron spins antiparallel, $\sigma_n(\uparrow\downarrow)$, and parallel, $\sigma_n(\uparrow\uparrow)$, as follows:

$$A_n \equiv \frac{\sigma_n(\uparrow\downarrow) - \sigma_n(\uparrow\uparrow)}{\sigma_n(\uparrow\downarrow) + \sigma_n(\uparrow\uparrow)} . \qquad (2.20)$$

A nonzero value of A indicates that the cross section depends upon the relative orientation of the electron spins; however, the interactions are spin independent. This paradox can be understood as arising from either the difference in spatial symmetry between singlet and triplet scattering or the interference between direct and exchange scattering. Reference to Table 2.1 and Table 1.7 shows that $\sigma(\uparrow\downarrow)$ and $\sigma(\uparrow\uparrow)$ are related to σ^s, σ^t, f and g as follows:

$$\begin{aligned} \sigma(\uparrow\downarrow) &= \frac{\sigma^s + \sigma^t}{2} = |f|^2 + |g|^2 \\ \sigma(\uparrow\uparrow) &= \sigma^t = |f - g|^2 . \end{aligned} \qquad (2.21)$$

The relationships in (2.21) allow the asymmetry to be rewritten in the following forms:

$$A = \frac{\sigma^s - \sigma^t}{\sigma^s + 3\sigma^t} = \frac{4\,Re\{f^* g\}}{|f + g|^2 + 3|f - g|^2} . \qquad (2.22)$$

Note that both denominators are equal to $4\bar{\sigma}$.

Combining (2.19) and (2.22) and solving for σ^s and σ^t in terms of A and $\bar{\sigma}$ yields

$$\begin{aligned} \sigma^s &= \bar{\sigma}(1 - A) \\ \sigma^t &= \bar{\sigma}(1 + 3A) . \end{aligned} \qquad (2.23)$$

Knowledge of only $\bar{\sigma}$ and A does not allow the complete isolation of f and g; however, combining (2.21) and (2.23) yields the following relationships:

$$|f|^2 + |g|^2 = \bar{\sigma}(1 + A)$$
$$Re\{f^* g\} = \bar{\sigma} A . \qquad (2.24)$$

Further separation requires the measurement of an additional asymmetry as described in Chapter One, Section III.D.1.

B. Optical Theorem

The optical theorem allows one to calculate the total scattering cross section by calculating only the T matrix element for elastic scattering in the forward direction as follows:

$$\sigma = \frac{16\pi^3 m}{p_1} Im\{T(\boldsymbol{p}_1, \phi_1 \leftarrow \boldsymbol{p}_1, \phi_1)\} . \qquad (2.25)$$

The theorem is based upon the unitarity of the scattering operator. The utility of the optical theorem in the present situation is that it allows calculation of the cross section for ionization by calculating only T matrix elements for elastic scattering and excitation. In principle, this method would require the calculation of every cross section except that for ionization, which seems like an increase in difficulty; however, in practice, only the cross sections for excitation to the first few levels need to be calculated, and these cross sections are much easier to calculate than the cross section for ionization.

C. Lippmann-Schwinger Equation

An alternate approach to calculating the T matrix uses the operators $\hat{T}_{n1}(z)$ defined by

$$\hat{T}_{n1}(z) \equiv \hat{V}_1 + \hat{V}_n \hat{G}(z) \hat{V}_1 , \tag{2.26}$$

where the Green's operator, $\hat{G}(z)$, is defined by

$$\hat{G}(z) \equiv (z - \hat{H})^{-1} , \tag{2.27}$$

and the scattering potential in the n^{th} channel, $\hat{V}_n$, is defined by

$$\hat{V}_n \equiv \hat{H} - \hat{H}_n , \tag{2.28}$$

where $\hat{H}_n$ is the channel Hamiltonian appropriate to the n^{th} channel. The T matrix can be written in terms of the $\hat{T}_{n1}(z)$ operators as

$$T(\boldsymbol{p}_1', \phi_n \leftarrow \boldsymbol{p}_1, \phi_1) = \left\langle \boldsymbol{p}_1', \phi_n \middle| \hat{T}_{n1}(E + i0) \middle| \boldsymbol{p}_1, \phi_1 \right\rangle . \tag{2.29}$$

Starting with the operator identity

$$\hat{A}^{-1} = \hat{B}^{-1} + \hat{B}^{-1}(\hat{B} - \hat{A})\hat{A}^{-1} \tag{2.30}$$

and substituting $\hat{A} = z - \hat{H}$ and $\hat{B} = z - \hat{H}_n$ yields

$$\hat{G}(z) = \hat{G}_n(z) + \hat{G}_n(z) \hat{V}_n \hat{G}(z) , \tag{2.31}$$

where the Green's operator, $\hat{G}_n(z)$, for the n^{th} channel is defined by

$$\hat{G}_n(z) \equiv (z - \hat{H}_n)^{-1} . \tag{2.32}$$

Multiplying (2.26) by $\hat{G}_n(z)$ yields

$$\hat{G}_n(z)\,\hat{T}_{n1}(z) = [\,\hat{G}_n(z) + \hat{G}_n(z)\,\hat{V}_n\,\hat{G}(z)\,]\,\hat{V}_1 = \hat{G}(z)\,\hat{V}_1 , \quad (2.33)$$

where the second equality follows from (2.31). Substituting (2.33) back into (2.26) yields the Lippmann-Schwinger equation

$$\hat{T}_{n1}(z) = \hat{V}_1 + \hat{V}_n\,\hat{G}_n(z)\,\hat{T}_{n1}(z) . \quad (2.34)$$

Taking matrix elements in the momentum representation, inserting a complete set of states and evaluating at $z = E + i0$ yields

$$T(\boldsymbol{p}_1', \phi_n \leftarrow \boldsymbol{p}_1, \phi_1) = \langle \boldsymbol{p}_1', \phi_n | \hat{V}_1 | \boldsymbol{p}_1, \phi_1 \rangle + \sum_{m=0}^{\infty} \int d^3p \, \frac{\langle \boldsymbol{p}_1', \phi_n | \hat{V}_1 | \boldsymbol{p}, \phi_m \rangle T(\boldsymbol{p}, \phi_m \leftarrow \boldsymbol{p}_1', \phi_1)}{E - E_m - \frac{p^2}{2m} + i0} , \quad (2.35)$$

where use has been made of (2.29) and (2.32).

II. APPROXIMATION METHODS

While many approximation methods have been applied to electron-impact ionization of hydrogen, only two, the convergent close-coupling method of Bray and Stelbovics (1992, 1993) and the hidden-crossing theory of Macek, Ovchinnikov and Pasovets (1995), are described here.

A. Convergent Close-Coupling Method

The results of the convergent close-coupling (CCC) method (Bray & Stelbovics 1992, 1993) agree reasonably well with the measured asymmetry (see Figure 6.3) over the entire range from threshold to 500 eV. While the earlier coupled-channel

optical method of Bray, Madison and McCarthy (1990) also leads to reasonable agreement with these measurements (Crowe *et al* 1990, Figure 3), it greatly overestimates (Bray, Konovalov & McCarthy 1991) the total ionization cross section as measured by Shah, Elliot and Gilbody (1987). The CCC method achieves good agreement with both sets of measurements. No other approximation method to date comes close to agreeing with the asymmetry measurements over the entire range from threshold to 500 eV [Fletcher *et al* 1985, Figure 23(a)].

The CCC method is a variation of the more traditional close-coupling method in which the state function for the entire system is expanded in terms of the eigenfunctions of the target, in this case the hydrogen atom. The CCC method uses a pseudostate expansion in a basis of L^2 functions (basically Sturmians) which diagonalize the hydrogen-atom Hamiltonian. The advantage of the pseudostate expansion is that it is discrete, and, therefore, the calculational problems associated with the continuum are avoided.

The CCC method uses symmetrized state functions to calculate singlet and triplet T-matrix elements, taking special care to assure the uniqueness of the state functions. The ionization matrix elements are calculated using the optical theorem. From threshold to 50 eV, the published results are from a calculation using seventy channels; from 50 to 500 eV, the results are from a calculation using eighty channels. The primary, n, and orbital, l, quantum numbers

associated with these channels are listed in Table 2.2. There are l + 1 channels associated with each value of l.

Table 2.2 Channels in CCC expansion.

ENERGY (eV)	# CHANNELS	n	l
13.6 to 50	70	1 to 13	0 to 2
50 to 500	80	1 to 10	0 to 3

B. Hidden-Crossing Theory

The recently published hidden-crossing theory of Macek, Ovchinnikov and Pasovets (1995) is a new approach to the threshold law for two-electron escape. The most successful previous threshold theory was first developed classically by Wannier (1953) and later extended quantum mechanically by Rau (1971), Peterkop (1971), Roth (1972) and others (see references in Friedman *et al* 1992). The most important difference between these theories is that the hidden-crossing theory is an *ab initio* theory while the Wannier theory and its quantum-mechanical extensions rely on the *ansatz* of ridge states; that is, nearly equal partitioning of the energy between the two escaping electrons in the region of the nucleus and consequently nearly equal radial distances from the nucleus.

The most successful result of the Wannier theory is the threshold law for the total ionization cross section, σ_I, which takes the form

$$\sigma_I \propto E^{\eta}, \tag{2.36}$$

where E is the excess energy above the ionization threshold and the Wannier exponent, η, is given by

$$\eta = \frac{1}{4}\left(\sqrt{\frac{100Z - 9}{4Z - 1}} - 1\right), \tag{2.37}$$

where Z is the charge of the resulting ion. The Wannier exponent has the value 1.127 for single ionization ($Z = 1$). Note that (2.36) is only a statement of proportionality. The Wannier theory does not predict the value of the coefficient.

The limitations of the Wannier theory are even more evident when applied to the calculation of asymmetries. In its simplest form, the Wannier theory predicts a constant asymmetry in the near-threshold region, but it does not predict the value of the constant. More sophisticated versions of the theory allow for some variation in the asymmetry, but do not predict even the sign of the slope let alone its magnitude. Even with their inherent flexibility, the predictions of the Wannier theory are not entirely consistent with experiment (Friedman *et al* 1992; Guo & Lubell 1993).

The hidden-crossing theory uses hyperspherical coordinates[12]. The most important coordinate in the hidden-crossing theory is the hyperadius, R, which is related to the

[12]It should be noted that the Wannier theory also uses hyperspherical coordinates.

electronic radii, r_1 and r_2, as measured from the proton, as follows:

$$R \equiv \sqrt{r_1^2 + r_2^2}. \tag{2.38}$$

The fundamental quantities in the theory are the adiabatic energy eigenvalues, $\epsilon(R)$, which are calculated at complex values of R. From these eigenvalues, an effective quantum number, $n(R)$, is defined as follows:

$$n(R) \equiv \frac{1}{\sqrt{-2\epsilon(R)}}. \tag{2.39}$$

A plot of $Re\{n(R)\}$ vs. $\sqrt{R}$ exhibits a sloped flat plane for nonreal values of $\sqrt{R}$. The system has harmonic-oscillator eigenfunctions in this region. The integrals involved in the calculation of the ionization cross sections are evaluated from a point on the real axis over to the harmonic-oscillator region and then to infinity in the harmonic-oscillator region.

The leading term for the cross section is the Wannier law, except now the coefficient is determined. In addition, the inclusion of higher-order terms leads to agreement with the measurements of McGowan and Clarke (1968) over the entire calculated range from threshold to 10 eV above threshold. The only caveat is that the calculated coefficient is 7.5% too high. Remember, however, that the Wannier theory does not predict the coefficient at all, and that its range of applicability is less than 1 eV.

The agreement between the calculated and measured asymmetries is somewhat less satisfactory (see Figure 6.1 and

Figure 6.2); however, the hidden-crossing theory does predict definite values for the asymmetry, which the Wannier theory does not. In addition, the hidden-crossing theory predicts rapid variations in the asymmetry near threshold. Further refinements in the theory are necessary before it can be determined whether these calculated variations will match the observed variations. Macek, Ovchinnikov and Pasovets (1995) have already suggested several corrections that can be applied to their calculations.

CHAPTER THREE: APPARATUS & PREPARATION

The purpose of this chapter is to describe the apparatus including the preparations necessary before data acquisition. The chapter comprises five sections describing the electron beam, the hydrogen beam, the interaction region, the vacuum system, and the computers and interfacing, respectively. Figure 3.1 is a schematic diagram of the experimental layout.

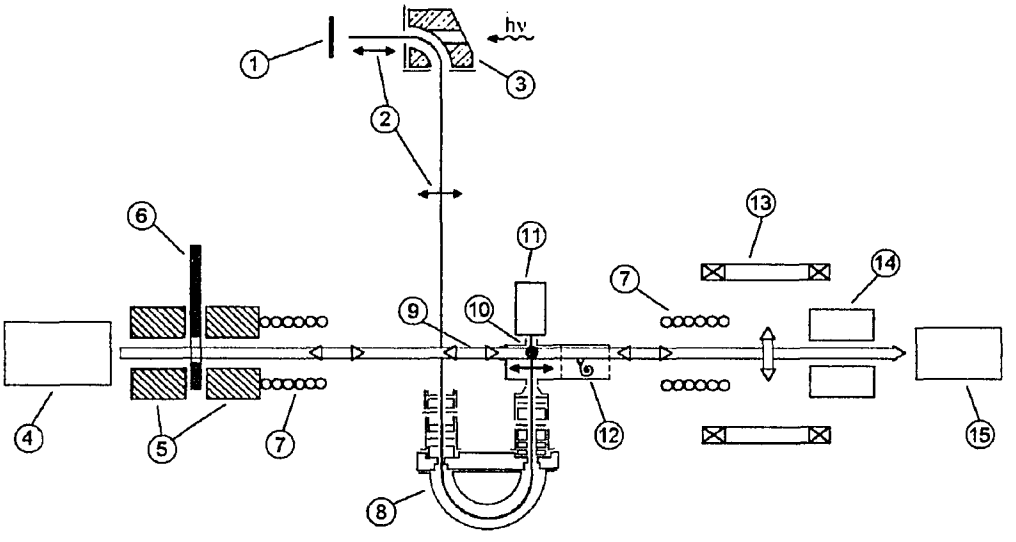

Figure 3.1 Schematic diagram of the experiment showing (1) GaAs photocathode, (2) electron polarization vector, (3) 90° spherical bender, (4) atomic hydrogen source, (5) hexapole magnets, (6) hydrogen beam chopper, (7) guide-field solenoids, (8) electron monochromator, (9) hydrogen polarization vector, (10) interaction point, (11) Faraday cup, (12) ion detector, (13) adiabatic spin rotator, (14) polarimetry magnet, and (15) quadrupole mass analyzer.

I. ELECTRON BEAM

The description of the apparatus associated with the electron beam comprises three sections describing the polarized-electron source, the electron optics, and the Faraday cup, respectively.

A. Polarized-Electron Source

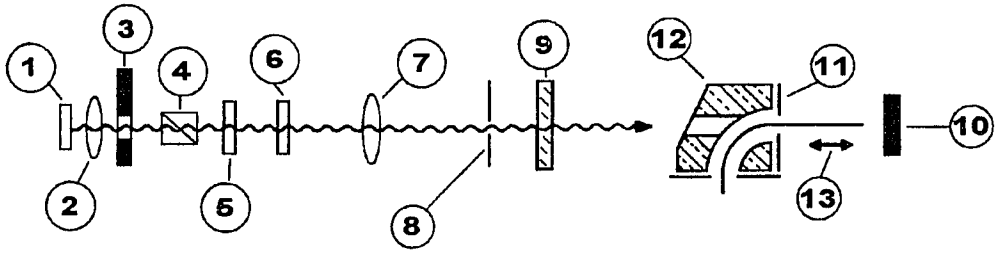

Figure 3.2 Schematic diagram of polarized-electron source showing (1) GaAlAs diode laser, (2) collimating lens system, (3) chopper, (4) linear polarizer, (5) half-wave plate, (6) quarter-wave plate, (7) focusing lens, (8) aperture, (9) vacuum window, (10) GaAs crystal, (11) anode extractor, (12) 90° electrostatic deflector, and (13) electron polarization vector.

A schematic diagram of the polarized-electron source appears in Figure 3.2. The description of the polarized-electron source comprises two sections describing the GaAs cathode and the GaAlAs laser and its associated optics, respectively.

1. GaAs cathode

The polarized-electron beam was generated by photoemission from a <100> face of a GaAs crystal. The GaAs wafers were purchased from M/A-Com Laser Diode, Inc. The

wafers, cut from ingot #15441P, are p-type, doped with Zn to a concentration of 1.6×10^{19} cm^{-3}. Each 0.013 in (0.33 mm) thick wafer was polished on one side only with an etch pit density of 6,000 - 10,000. All of the above specifications are according to the manufacturer's catalog.

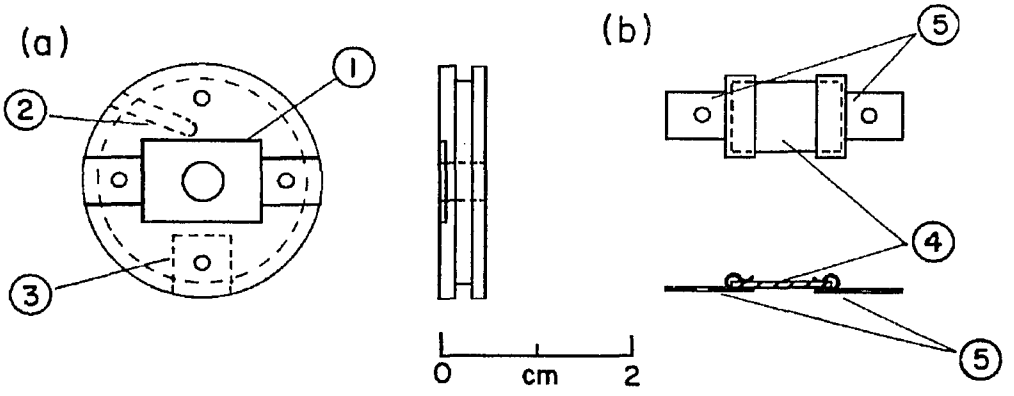

Figure 3.3 **(a)** Front and bottom views of sapphire mounting block for GaAs crystal showing (1) milled slot for crystal, (2) channel for platinum thermometer (not used), and (3) machined step and hole for mechanical support. **(b)** Front and side views of clamp assembly showing (4) GaAs crystal and (5) tantalum clamps.

Four pieces, measuring 7 x 10 mm each, were cut from the wafers and chemically etched. The best of the four pieces was then mounted onto a sapphire block via two tantalum clamps, as illustrated in Figure 3.3, the block being already mounted on an ultrahigh vacuum flange. The flange was then bolted into place and the chamber evacuated. The details of the etching procedure can be found in Tang *et al* (1986).

As mentioned in Chapter One, the quantum efficiency of photoemission drops rapidly with increased contamination on the crystal surface; therefore, the maintenance of a clean

surface is of utmost importance. This objective is achieved by maintaining the crystal's environment at ultrahigh vacuum and by periodically heat cleaning the surface. The initial pump down of the chamber was slower than ideal, taking four hours from the time the etched crystal was exposed to air to achieve 2 μTorr. At one point before data acquisition, the source chamber was brought up to atmospheric pressure for approximately three hours by backfilling with dry nitrogen. No effect upon the performance of the crystal was noted.

The crystal is heat cleaned by passing a current through it via wires connected to the tantalum clamps. The current was increased by ~0.5 A steps every few minutes until the crystal temperature reached ~630°C at which point the heating current was ~2-2.5 A and the crystal resistance was ~1.5-2 Ω. The crystal was left at that temperature for ~20-30 minutes although it was sometimes heated for longer periods at slightly lower temperatures. The crystal temperature was monitored by a chromel-alumel thermocouple in contact with it. Unfortunately, heat conduction along the thermocouple wires, despite the use of thin [0.001-inch (25.4-μm) diameter] wires, lowered the temperature of the contact point; therefore, the thermocouple always gave low readings. Once the crystal temperature reached ~600°C, its blackbody radiation became visibly red in a darkened room; therefore, the maximum temperature was always monitored in this way. This method also allows a rough determination of the temperature

distribution across the surface of the crystal. It was observed that AC gave a more uniform distribution than did DC.

As mentioned in Chapter One, the quantum efficiency of the photoemission process is enhanced by applying alternating layers of Cs and O_2 to the crystal surface, a procedure known as yo-yo activation. The Cs dispensers are type CS/NF/3.9/12 purchased from SAES Getters. The Cs dispensers were initially outgassed by passing 5.5 ADC through them for 30 s. The crystal was heated, as described in the previous paragraph, while the Cs dispensers were outgassed in order to prevent contamination of the crystal surface.

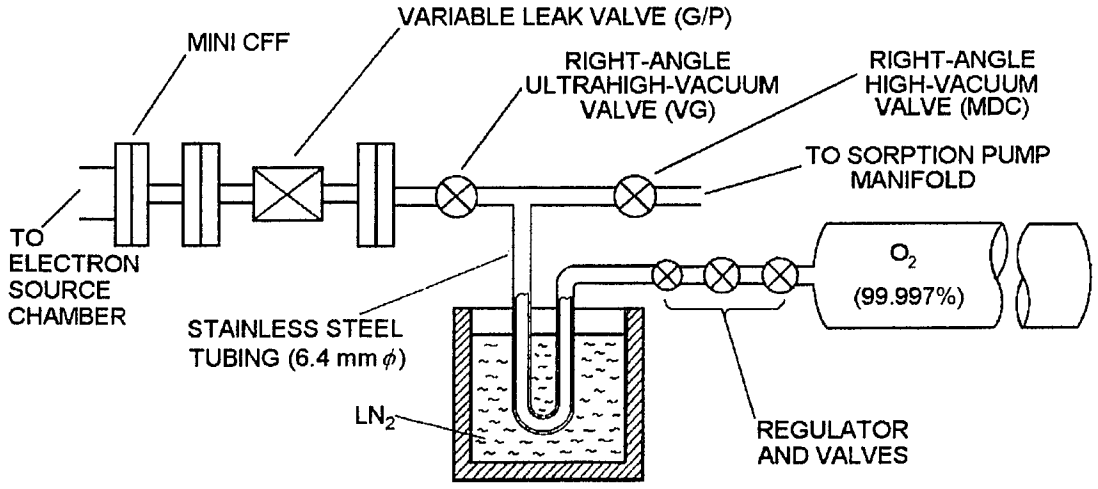

Figure 3.4 Schematic diagram of O_2 delivery system.

A schematic diagram of the O_2 delivery system appears in Figure 3.4. The O_2 tank was purchased from Matheson Gas Products, Inc. who specify the purity as "Research Grade" with a minimum purity of 99.997%. The tank was filled 27 September 1988 with 25 L of gas from lot number 685-0125-D5 compressed to 825 psig @ 70°F. The tank is connected to a Matheson model

3603 regulator followed by a Matheson model FT 4374 valve. The variable leak valve is a series 203 manufactured by Granville-Phillips. The right-angle valve leading to the sorption-pump manifold is an MDC model AV-050; the right-angle valve next to the variable leak is a Vacuum Generators model CR97. The O_2 line is made of SS-304, and all connections are "mini-Conflat" flanges with the following exceptions: the connection to the O_2 tank is a flare seal, both connections to the regulator and one connection to the Matheson valve are ¼" NPT, and the other connection to the Matheson valve is ¼" Swagelok. The O_2 line was first baked out and then purged by alternately pumping with a sorption pump to 10 mTorr and refilling with ~1 psig O_2 ten times. The LN_2 dewar condenses most of the oxygen thereby reducing the gas pressure in the O_2 line and allowing greater control of the rate of O_2 admission into the electron-source chamber.

The crystal was raised above its operating position during activation and positioned directly in front of a cesiator ~50 mm away. The photocurrent from the crystal was monitored during the activation by a molybdenum rod maintained at 800 V relative to the crystal. The rod is located behind the cesiator a distance of ~70 mm from the crystal. During activation, a mirror system allowed the laser light to bypass all elements of the optics train (described in the next section) except the collimating lens system. The laser power at the exit of the collimating lens system was typically 13 mW during activation. Once the crystal was heat cleaned and its

temperature returned to ~50°C, cesium was deposited on the crystal by passing ~5-5.5 A through the cesiator. The crystal current reached a peak of ~50 nA after ~10 min. The crystal was then overcesiated until the photocurrent dropped to ~50% of its peak level, at which point the current to the cesiator was shut off and O_2 was admitted into the chamber. The photocurrent very quickly reached a second peak higher than the first and again was allowed to drop to ~50% of its new peak level, at which point the leak valve was closed and the cesiator current restored to its former value. This process of alternately depositing Cs and O_2 was continued until negligible increase in photocurrent was observed, by which time ~10 layers of each had been applied, the final layer being O_2. The final crystal current was typically 8 μA in its activation position and 25 μA in its operating position, the increased value in the latter case apparently due to the focusing of the laser power onto a hot spot of the crystal surface. The photocurrent was reduced to ~5 μA by reducing the laser power so that the transport efficiency and stability were improved. The quantum efficiency was typically ~2% in the operating position.

In the operating position, the electrons were extracted by a planar anode with a 4-mm-diameter aperture located 6.9 mm from the crystal surface (see Figure 3.5). The lifetime of the crystal was greatly extended by continuous, low-level cesiation provided by a Cs dispenser embedded in the anode and was maximized when the current through the cesiator was ~4 A

giving an e-folding lifetime of ~400 h. The embedded cesiator was biased symmetrically about the anode bias so as to minimize its effect upon the electron beam tuning. A schematic diagram of the cesiator biasing circuit appears in Figure 3.6

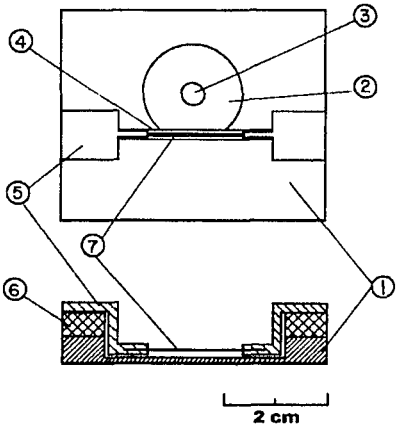

Figure 3.5 Scale drawing of anode extractor with embedded Cs dispenser. The labelled elements are (1) stainless steel mounting plate, (2) molybdenum anode, (3) 4-mm-diameter anode aperture, (4) cesiator mounting slot, (5) Macor insulating supports, (6) copper mounting blocks, and (7) cesiator crimped in copper blocks.

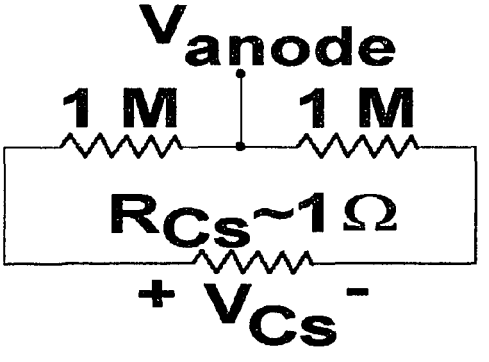

Figure 3.6 Schematic diagram of biasing circuit for cesiator embedded in anode.

2. GaAlAs laser and laser optics

A Sharp model LT021 MF 15 mW GaAlAs diode laser was used to generate photoelectrons from the activated crystal (see Figure 3.2). The laser operates at ~780 nm, with a slight dependence upon temperature and optical power, according to the manufacturer's manual. Its optical power is continuously adjustable up to a rated value of 15 mW. A Melles Griot model 06GLC002 laser diode collimator was mounted directly in front of the diode laser. The laser-beam chopper is a strip of stainless-steel sheet mounted on a stepping motor that was operated under computer control. The Glan prism polarizing cube (model 21-7015-790-BBAR), the half-wave (model 8-8015-½-790) and quarter-wave (model 8-8015-¼-780) retardation plates were all purchased from Special Optics. The last three digits of each serial number indicates the design wavelength in nm; the extension BBAR indicates broad-band, antireflective coating. Each retardation plate is mounted in an Oriel model 13049 motorized 360° rotator that is operated under computer control. The focusing lens is an Oriel model 40390 lens with a focal length of 250 mm. The aperture is a Melles Griot model 04IDC003 pin actuated diaphragm. The vacuum window is a model VP-600 purchased from MDC Vacuum Products Corp.

The polarization, P_{linear}, of the laser light was determined by inserting an Oriel model 27360 near-infrared linear polarizer and measuring the maximum power, P_{max}, and minimum power, P_{min}, transmitted through it as it was rotated through 360°. The laser power was measured with a Newport

model 816 photosensor connected to a Newport model 815 digital power meter. A Newport model 817 OD-3 neutral density filter was placed in front of the photosensor. The linear polarization was calculated using the formula (Hecht & Zajac 1974, p. 246)

$$P_{linear} = \frac{P_{max} - P_{min}}{P_{max} + P_{min}}, \qquad (3.1)$$

giving values of 98.4% after the collimating lens system, a maximum of 99.7% after the polarizing cube, 99.9% after the half-wave plate, and a minimum of 7.9% after the quarter-wave plate. The circular polarization, $P_{circular}$, after the quarter-wave plate was calculated to be 99.6% using the formula (Born & Wolf 1964, p. 31)

$$P_{circular} = \sqrt{P_{in}^2 - P_{out}^2}, \qquad (3.2)$$

where P_{in} (P_{out}) is the linear polarization before (after) the quarter-wave plate.

B. Electron Optics

A schematic diagram of the electron optics appears in Figure 3.7. The description of the electron optics comprises six sections: the 90° deflector, the transport optics, the hemispherical monochromator, the power supply and voltage dividers, the electromagnetic shielding, and the deviations from the original design voltages, respectively. The diode extraction of electrons from the crystal is described in Section A.1 above. The first three sections describe mechanical characteristics only: all optical-element voltages

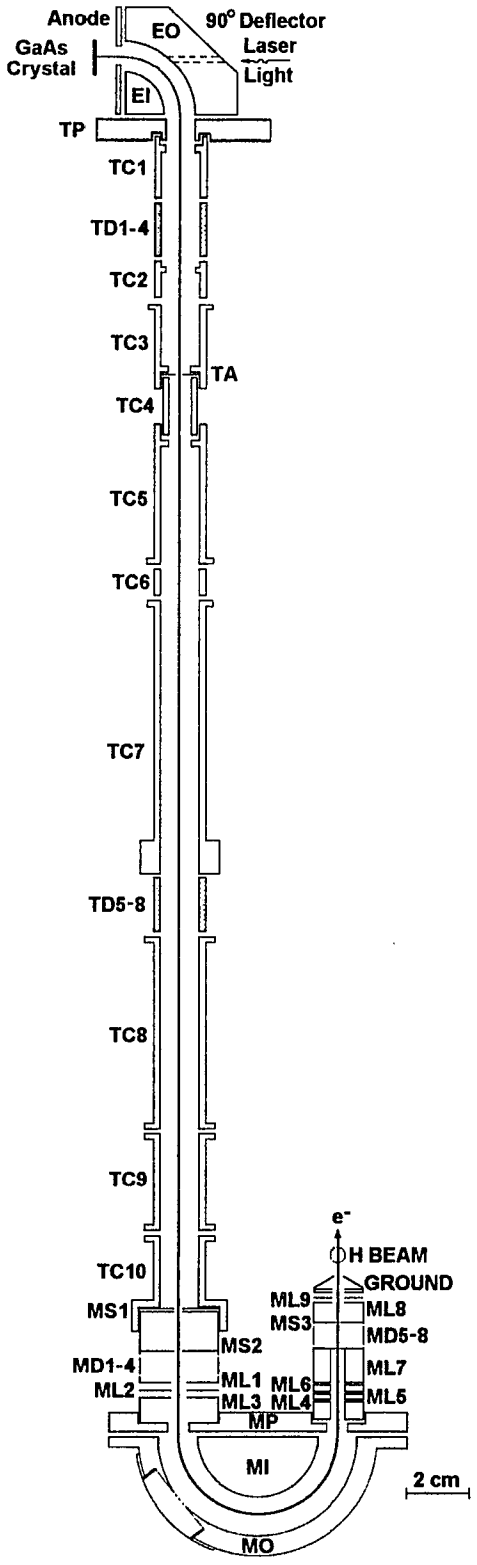

Figure 3.7 Schematic diagram of electron optics.

are described in the final section only. The calculations used for the original mechanical design of the electron-optical elements appear in a previous dissertation (Tang 1989, pp. 205-20) and are not repeated here. During the process of tuning the electron beam for the present study, Tang's description of the electron optics was found to contain a few errors. The mechanical structure was not altered, except by the removal of one aperture, but the corrected information is included in the description that follows.

1. 90° deflector

The electron polarization is converted from longitudinal to transverse by an electrostatic 90° deflector (Kessler 1985, p.230), as illustrated in Figure 3.2 and Figure 3.7. The deflector also acts as a dispersive element, the dispersion being a benign side effect that assists the hemispherical monochromator (described in Section 3 below) in improving the energy resolution of the electron beam probe. The steering surfaces of the deflector are two concentric spherical sections of radii 19.05 mm and 31.75 mm. A 3-mm-diameter hole was drilled through the outer piece in order to pass the laser light to the crystal. The axis of the hole is aligned with the center line of the gap between the two sections of the deflector and with the normal to the anode aperture. The deflector is mechanically connected to the anode and supported by another plate with electrical isolation provided by ruby and/or sapphire balls. The separations between the deflector and the plates were chosen so that the fringe fields were

Herzog corrected (Herzog 1934, 1935). The deflector is made of OFHC copper.

2. Transport optics

Due to the vacuum requirements of the GaAs crystal, the electron source is located in a separate chamber from the interaction point. This separation requires the beam to travel more than 0.5 m from the output of the 90° deflector to the input optics of the monochromator. A three lens system is used to transport the electron beam through this distance, as illustrated in Figure 3.7. The first lens is an accelerating two-cylinder lens; the second lens is a three-cylinder einzel lens with initial acceleration; the third lens is a three-cylinder immersion lens with deceleration at both steps (Harting & Read 1976).

The physical elements of the transport optics comprise one support plate, ten cylinders, one aperture and two sets of four deflector plates each. All elements are electrically isolated from each other by ruby and/or sapphire balls with the following exceptions: TC4 is shorted to TC3 and TC5 by friction fits and to the aperture TA which is held in place by a retaining ring; TC1 is shorted to TP by a friction fit. (TC10 is also shorted to the first element of the input optics of the monochromator, as described in the next section.) The transport optics is mounted vertically and supported by external rods. Table 3.1 lists the effective heights and inner dimensions of the various elements. The support plate, cylinders and deflector plates are made of arcap (AP4); the

Table 3.1 Transport optics dimensions.

ELEMENT	EFFECTIVE HEIGHT (mm)	INNER DIMENSION[1] (mm)
gap	0.64	-
TP	9.7	12
TC1	3.3 21.3	12 15
gap	1.5	-
TD1-4	25.0	13 x 13
gap	1.5	-
TC2[2]	1.8 0.7 0.3 1.0 13.2	15 17 15 12 15
gap	1.5	-
TC3	26.3	15
TA	0.3	1.8
TC4	32.7	12
TC5	3.3 4.6	12 15
gap	1.5	-
TC6	13.5	15
gap	1.5	-
TC7	120.0	15
gap	1.5	-
TD5-8	25.0	13 x 13
gap	1.5	-
TC8	83.9	15
gap	1.5	-
TC9	43.5	15
gap	1.5	-
TC10	30.9	15

Notes: (1) A single number in the Inner Dimension column indicates a diameter; the designation "13 x 13" indicates the lengths of the sides of the square cavity of the deflectors.
(2) The complicated design of TC2 was intended to support an aperture secured with a retaining ring. The aperture was removed, before the present measurements, to facilitate beam transport.

aperture is made of molybdenum in order to minimize the patch effect (Moore, Davis & Coplan 1983, p. 317); the retaining ring is made of Inox.

3. Monochromator

A hemispherical monochromator (see Figure 3.7) is used to narrow the energy spread of the polarized-electron beam probe. This section describes the hemispherical monochromator including its associated input and output optics. The monochromator is operated at low voltages; therefore, all elements are made of molybdenum in order to minimize the patch effect. The only exception is the cover for the output optics which is made of stainless steel.

The entire structure is supported by the outer hemisphere which is in turn supported by four stainless steel rods. The inner hemisphere is supported by a bolt which is supported by a plate, MP. Electrical insulation between the plate and the hemispheres is provided by Macor bushings and ruby and/or sapphire balls. The radii of the hemispherical surfaces are 19.05 mm and 31.75 mm. The vertical axes of the input and output optics are tangential to the spherical surface of radius 25.4 mm midway between the material surfaces. The outer hemisphere contains a 6.35-mm-diameter hole used for vertical alignment of the transport optics.

The input optics comprises a pair of aperture stops, MS1 and MS2, separated by a spacer followed by a set of four deflectors followed by a three-aperture lens followed by another spacer and the plate MP. The two stops limit the

angular spread of the beam as it enters the monochromator, thereby improving the energy resolution. The three-aperture lens forms an image of MS1 at the entrance plane of the hemispheres. The input optics is held in place and electrostatically shielded by a cover that is bolted to MP. Electrical insulation between the cover and MP is provided by Macor bushings. The other elements of the input optics are electrically isolated by ruby and/or sapphire balls with the following exceptions: the cover is shorted to TC10 and MS1 by friction fits; MS1 is shorted to $spacer_1$ by stainless steel (SS) balls; ML3 is shorted to $spacer_2$ by SS balls. ML3 was also shorted to MP unintentionally, presumably through wires. The effective heights and inner diameters of the elements of the input optics are listed in Table 3.2.

The output optics comprises the plate MP followed in sequence by a four-cylinder lens, the energy-analyzing aperture MA, a set of four deflectors, an aperture stop MS3, a three-aperture lens, and a cover. The four-cylinder lens forms an image of the exit plane of the hemispheres at MA. The three-aperture lens is used for focusing the beam at the interaction point. The cover holds the output optics in place in addition to providing electrostatic shielding. The cover is bolted to MP. Electrical insulation is provided by Macor bushings. The other elements of the output optics are electrically isolated by ruby and/or sapphire balls with the following exceptions: ML7 is shorted to MA by SS balls; the cap is shorted to ML10 by SS balls and to the cover by a

Table 3.2 Monochromator input optics dimensions.

ELEMENT	EFFECTIVE HEIGHT (mm)	INNER DIAMETER[1] (mm)
cover	1.3	(15°) 7.6
MS1	1.6	(15°) 1.8
gap	0.76	-
$spacer_1$	10.7	12.7
gap	0.76	-
MS2	1.0	(15°) 1.8 (15°)
gap	0.76	-
MD1-2[2]	3.4	12.7
gap	0.76	-
MD3-4[2]	3.4	12.7
gap	0.76	-
ML1	1.0	(15°) 5.1 (15°)
gap	0.76	-
ML2	1.0	(15°) 5.1 (15°)
gap	0.76	-
ML3	1.0	(15°) 5.1 (15°)
gap	0.76	-
$spacer_2$	5.1	12.7
gap	0.76	-
MP	4.0	6.4
gap	0.76	-

Notes: (1) An angle listed in parentheses indicates a bevel. The diameter listed is the minimum diameter, which occurs on the downstream side if only one bevel is indicated or at the midpoint if two bevels are indicated.
(2) The deflectors come in pairs. Each pair forms a cylinder with a 1.6-mm-wide gap centered upon a diameter.

Table 3.3 Monochromator output optics dimensions.

ELEMENT	EFFECTIVE HEIGHT (mm)	INNER DIAMETER[1] (mm)
gap	0.76	-
MP	4.00	6.4
gap	0.76	-
ML4	6.15	4.8
gap	0.48	-
ML5	1.90	4.8
gap	0.51	-
ML6	1.90	4.8
gap	0.51	-
ML7	10.9	4.8
gap	0.76	-
ML7A	1.0	(15°) 1.8
gap	0.76	-
MD5-6[2]	3.2	6.4
gap	0.76	-
MD7-8[2]	3.2	6.4
gap	0.76	-
MS3	1.0 5.0	(15°) 1.8 3.2
gap	0.76	-
ML8	1.0	(15°) 3.2 (15°)
gap	0.76	-
ML9	1.0	(15°) 3.2 (15°)
gap	0.76	-
ML10	1.0	(15°) 3.2 (15°)
gap	0.76	-
cap	1.6	3.2
cover	0.25 1.3 3.1	12.7 6.4 3.2 (45°)[3]

Notes: (1) An angle listed in parentheses indicates a bevel. The diameter listed is the minimum diameter, which occurs at the downstream side (except as noted below) if only one bevel is indicated or at the midpoint if two bevels are indicated.
(2) The deflectors come in pairs. Each pair forms a cylinder with a 1.6-mm-wide gap centered upon a diameter.
(3) The minimum diameter is on the upstream side.

friction fit. The effective heights and inner diameters of the elements of the output optics are listed in Table 3.3.

4. Power supply & voltage dividers

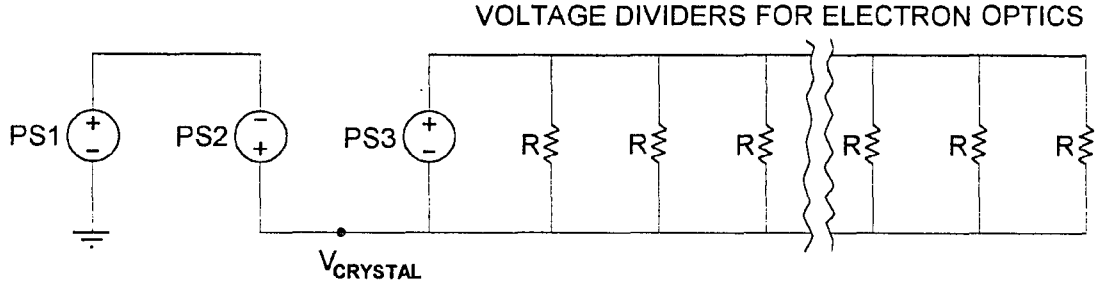

Figure 3.8 Schematic diagram of circuit used to bias cathode and electron optics.

The energy of the electron beam was set by a series combination of two power supplies connected between ground and the cathode (see Figure 3.8). A Kepco model APH 1000M power supply (PS2 in Figure 3.8) provided a rough bias over the range 0-1000 VDC; a Lamda model LDS-X-01 power supply (PS1 in Figure 3.8) provided fine adjustment over the range 0-7 VDC. The determination of the beam energy is described in detail in Chapter Four, Section II.A.

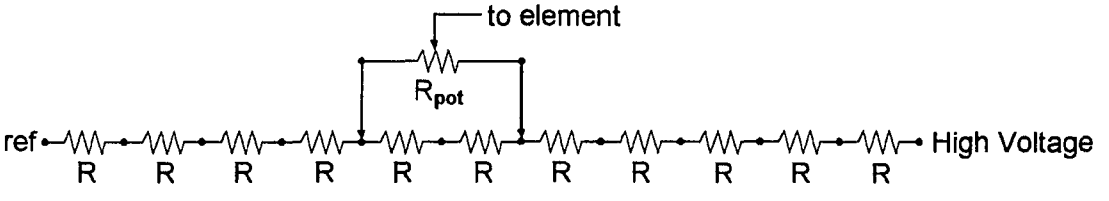

Figure 3.9 Schematic diagram of voltage dividers used for electron-optics biases.

The elements of the electron optics were biased relative to the cathode by a power supply (PS3 in Figure 3.8) connected in parallel with each of several voltage dividers. This

Table 3.4 Resistance values for voltage dividers.

R (kΩ) (±1%)	R_{pot} (kΩ)	ELEMENTS
249	500	90° deflector transport optics ML1,2,4-6,8,9; MS3
24.9	50	anode; hemispheres MS1-2; ML3,7; MP

arrangement required a minimum of retuning if the beam energy was changed. The power supply, a model 210-03R purchased from Bertan Associates, Inc., is adjustable over the range 0-3000 VDC and was set at 2000 VDC throughout all measurements described in this dissertation. Each voltage divider includes a ten-step switch and a potentiometer, as shown schematically in Figure 3.9. All dividers have the same total resistance of 2.49 MΩ, but two different sets of resistors are used to allow for finer control of the voltage of elements with low biases. These sets are listed in Table 3.4 along with the elements using each set. The set with the smaller step resistance is preceded by nine 249-kΩ resistors in series connected to the high voltage side.

5. Electromagnetic shielding

Due to the use of a low-energy beam, especially in the monochromator, it is necessary to shield the beam from stray electromagnetic fields. As mentioned in Section 3, the cover of the monochromator output optics is grounded and serves as a Faraday cage for the output optics. The interaction region is also enclosed by a grounded, stainless-steel box (see

Section III). The interaction region is additionally shielded by a grounded, u-shaped, stainless-steel sheet that covers the monochromator input optics as well as the portion of the transport optics within the interaction chamber. The Faraday cup is also enclosed in a grounded shield as described in Section C.

Magnetic shielding is provided by sheets of 0.5-mm-thick μ-Metal in combination with residual field compensating coils: the coils reduce the magnetic fields due to the earth, ion pumps, motors, etc. to intensities (<100mG) that the μ-Metal can effectively shield. The μ-Metal lines the sides of the electron-source chamber from the bottom to just below the laser-beam line, it surrounds the outside of the nipple that connects the electron-source chamber to the interaction chamber, and it completely covers the inside of the interaction chamber except for the ports. The μ-Metal in the interaction chamber is wrapped with a coil of wire that allowed *in situ* 60-Hz degaussing; the μ-Metal surrounding the nipple is similarly wrapped; the μ-Metal in the electron-source chamber is not wrapped, since the electrons are accelerated rapidly after they leave the GaAs crystal and are somewhat less sensitive to small stray fields.

Three sets of coils are used. A pair of large coils with vertical dipole moments is used primarily to compensate for the earth's magnetic field. The coils are irregularly shaped, but each coil is nearly square, 1.3 m on a side. The two coils are separated vertically by 1.48 m, the top coil being

slightly above the electron-source chamber, the bottom coil just below the interaction chamber and the midpoint being at the base of the electron-source chamber. Each coil is made of a 31.75-mm-wide, thirty-wire ribbon with the thirty wires connected in series to make a thirty-loop coil. Additionally, the two coils are run in series. The power for these coils is supplied by a Sorensen Power Supplies model DCR 150-6B manufactured by the Raytheon Company.

A set of four coils with horizontal dipole moments are located on the 203-mm-diameter flanges of the electron source chamber. These coils are wired in pairs with each pair wired in series. One pair is wrapped on 210-mm-square, aluminum forms that fit snugly over the flanges. Each coil of this pair is wound with twenty-seven turns in three layers and has its dipole moment parallel to the laser beam. The other pair is wound directly on the flanges. Each coil of this pair is wound with twenty-seven turns in two layers with its dipole moment perpendicular to the laser beam. The power supply for the first pair is an Electronic Measurements, Inc. model RE 40-I0-ML; the power supply for the second pair is a Kepco model ATE 75-3M.

A set of four coils is located atop the interaction chamber forming a 183-mm square about the nipple connecting the electron-source chamber to the interaction chamber. Each coil is wrapped in a single layer on a solid, rectangular piece of wood 145 mm × 48 mm. These coils are wired in pairs with each pair wired in series and are aligned with the coils

on the electron source chamber. The pair with dipole moment parallel to the laser beam contains fifteen turns; the pair with dipole moment perpendicular to the laser beam contains fourteen turns. Each pair is powered by a Harrison Laboratories, Inc. model 855B power supply.

6. Deviations from the original design voltages

The transport efficiency of the electron beam was found to be much too small if the original design voltages (Tang 1989) are used. The trouble is due to design errors and stray electromagnetic fields.

A major design error resulted from misplacement of the image of the electron source as the beam makes the transition from the transport optics to the input optics of the monochromator. The image should occur at MS1, but the original design placed the image 17.9 mm before the stop. A second design error resulted in the hemispheres of the monochromator being improperly Herzog corrected. Additionally, the original designs for the plate supporting the 90° deflector and the three-aperture lens of the monochromator input optics do not match the shop specifications; therefore, the design voltages do not match the physical device. Finally, the support for the cathode does not allow for adjustment of the cathode-anode separation; therefore, any error in this separation must be corrected by adjusting the voltages on the electron-optics elements.

Stray electromagnetic fields also necessitated deviations from design voltages. Partial compensation for these fields

is achieved by the methods described in the previous section, but residual effects remain. It should be noted that a magnetic field of ~100 mG is intentionally imposed at the interaction point in order to ensure that the polarization vector of the hydrogen beam is aligned longitudinally (see Section II.D).

Table 3.5 lists typical voltages used during data acquisition. Table 3.6 lists the corresponding currents in the compensating coils. This setting was recorded 5 July 1989 at which time 85% of the beam was transmitted to MS1, but only 3% was transmitted to the interaction region, still quite sufficient for experimental purposes given the large currents produced by the phocathode and the space-charge limits in the monochromator. Some of the loss in the monochromator is due to energy selection; however, note the strong steering in MD1-4 which indicates alignment problems that probably account for most of the losses in the monochromator. The alignment problems are due to the improper Herzog correction of the hemispheres and, probably, stray electromagnetic fields.

C. Faraday Cup

The intensity of electron beam is measured at the interaction point by means of a Faraday cup, a scale drawing of which appears in Figure 3.10. The Faraday cup proper is surrounded by a grounded shield except at the input which is covered by a grid connected to the cup proper. The purpose of the grid is to prevent backstreaming of the electrons. The

Table 3.5 Typical operating voltages for electron optics.

ELEMENT[1]	VOLTAGE (V)[2]	ELEMENT[1]	VOLTAGE (V)[2]
anode	142	ML1	17.56
EO	93.7	ML2	26.9
EI	247	ML3,MP	17.9
TP,TC1-2	148.9	MI	12.9
TD1	148.1	MO	6.05
TD2	149.6	ML4	6.29
TD3	152.1	ML5	85.9
TD4	145.5	ML6	3.92
TA,TC3-5	691	ML7	88.3
TC6	1649	MD5	86.6
TC7	704	MD6	90.1
TD5	703	MD7	99.8
TD6	704	MD8	76.5
TD7	701	MS3	18.4
TD8	705	ML8	346
TC8	715	ML9	104
TC9	185.9	Faraday cup	90
TC10,MS1-2	51.4		
MD1	78.2		
MD2	24.4		
MD3	67.9		
MD4	34.5		

Notes: (1) Elements listed together are connected in parallel to the same voltage divider.
(2) All voltages are relative to the cathode.

Table 3.6 Typical operating currents for compensating coils.

POSITION OF COIL PAIR	DIRECTION[1] OF MAGNETIC DIPOLE	CURRENT (A)
Earth's field compensators	up	2.0
electron-source chamber	0°	1.8
	90°	4.8
atop interaction chamber	180°	1.12
	90°	1.08

Note: (1) Horizontal directions are counterclockwise from the direction of propagation of the laser beam when looking down.

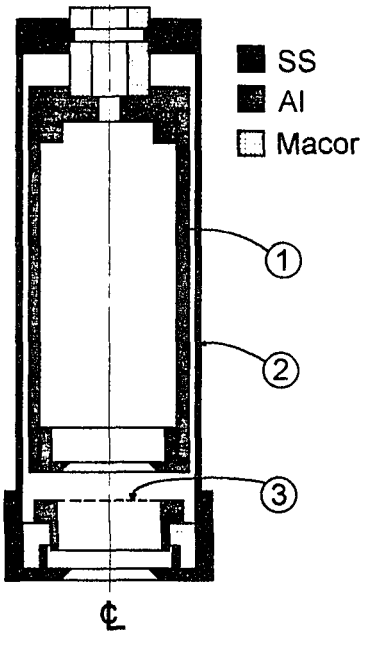

Figure 3.10 Scale drawing of Faraday cup assembly showing (1) Faraday cup, (2) ground shield and (3) entrance grid.

cup and grid are maintained at a potential of 90 V relative to ground by means of a battery.

II. HYDROGEN BEAM

The description of the hydrogen beam will be brief since it has been presented in detail elsewhere (Slevin & Stirling 1981; Chan *et al* 1988). Five sections describe the atomic-hydrogen source and skimmer, hexapole magnets, guide-field solenoids, analyzing magnet, and quadrupole mass analyzer, respectively. Figure 3.11 is a schematic diagram of the entire beam line.

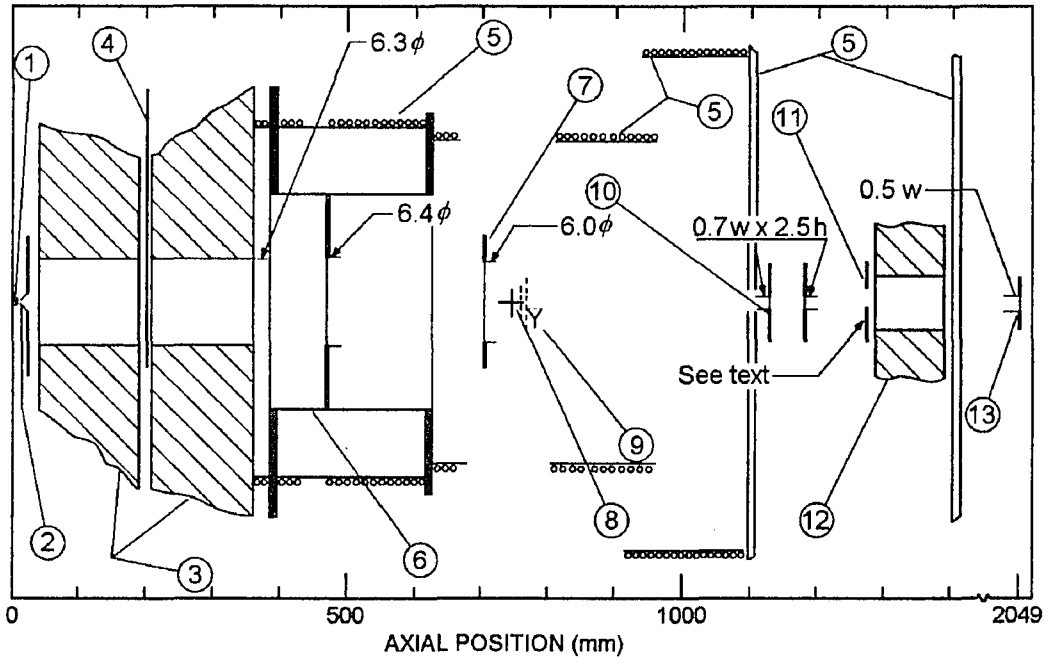

Figure 3.11 Schematic diagram of the hydrogen beam line showing the location and critical dimensions of (1) nozzle, (2) skimmer, (3) hexapole magnets, (4) beam chopper, (5) guide-field coils, (6) refrigerated tube and aperture, (7) interaction-region beam collimator, (8) interaction point, (9) channel electron multiplier, (10) movable, vertical slits, (11) analyzing magnet entrance aperture, (12) analyzing magnet, and (13) quadrupole mass analyzer entrance slit. All dimensions are in mm. (Note that the transverse scale is much larger than the axial scale.)

A. Atomic-Hydrogen Source & Skimmer

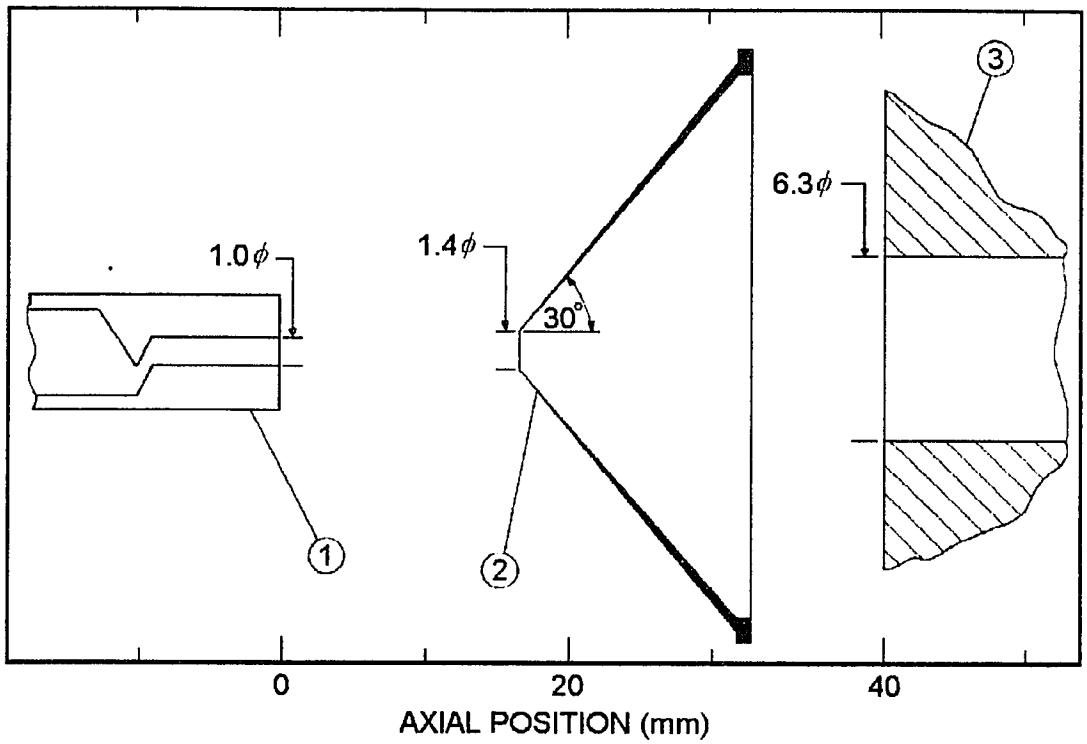

Figure 3.12 Schematic diagram of hydrogen-beam-line source region showing (1) nozzle, (2) skimmer, and (3) hexapole magnets.

The radio-frequency, atomic-hydrogen-beam source was designed for this series of experiments by J. Slevin and W. Stirling, then of the University of Stirling, Scotland. It dissociates molecular hydrogen in a water-cooled Pyrex tube with a radio signal tuned to the tube's resonant frequency of 35 MHz. The molecular hydrogen is purified before entering the dissociation tube by allowing it to diffuse through a heated palladium finger, which also permits the pressure within the dissociation tube to be controlled. The dissociated hydrogen gas leaves the Pyrex tube via a 1-mm-diameter nozzle, which contains a kink prevents excited atoms

and Lyman-α radiation produced in the source from reaching the interaction region. When an electric field of several hundred V/cm was applied at the exit of the Pyrex tube, no change in the ion-counting rate was observed at the interaction region, indicating the absence of metastable (2s) and high-lying Rydberg atoms in the beam, potentially the largest source of excited-state contaminaton.

During data acquisition, the pressure in the dissociation tube is typically ~400 mTorr with ~14 W of forward rf power and ~5 W of reflected rf power. In order to keep the dissociation tube clean during pauses in data acquisition, the pressure within the tube was maintained at ~100 mTorr with ~8 W of forward rf power.

A stainless-steel skimmer is used to help form the beam as well as to provide for differential pumping. The skimmer has a 1.3-mm-diameter hole located 16.5 mm from the nozzle exit. The nozzle-skimmer distance is adjustable and is set to maximize the beam density at the interaction region.

B. Hexapole Magnets & Beam Chopper

Two identical hexapole magnets arranged in tandem are used to state select the hydrogen atoms. The magnets also focus the selected atoms at the interaction point, with considerable chromatic aberration, however. The positions of the magnets were selected by maximizing the atomic density at the interaction point in a simulation program. Each magnet is 152 mm long, has a pole gap of 6.4 mm and a magnetic pole

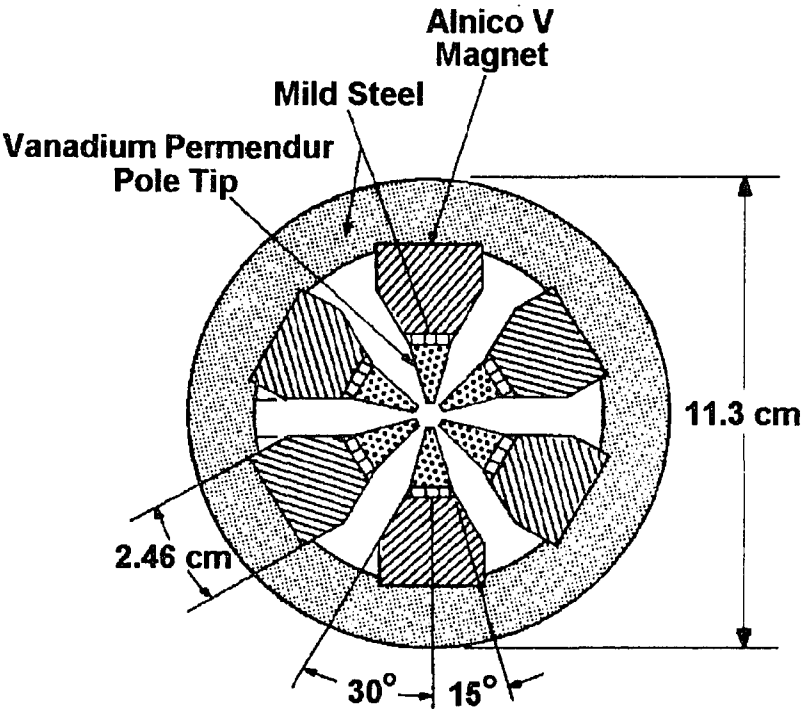

Figure 3.13 Cross-sectional scale drawing of hexapole magnet.

strength of 0.79 T. The entrance to the first magnet is 25.4 mm downstream of the skimmer.

A computer-controlled beam chopper operates between the two magnets in a 19-mm gap that also facilitates pumping. The beam chopper is a strip of stainless-steel sheet connected to a stepping motor. The distance between open and closed positions of the chopper is 251 mrad (four steps) corresponding to an arc length of 36.7 mm at the axis of the magnets. A delay of 20 ms is used after each step so that the motor does not skip steps. This design for the beam chopper is flawed in that the chopping frequency of the atomic beam is limited to less than ~10 Hz. During the course of the measurements described in this dissertation, it was discovered that, as a result of the slow chopping speed, the background

pressure in the interaction region increases significantly while the beam is present and decreases significantly while the beam is blocked with corresponding fluctuations in the background ion signal due to ionization of the residual gas[13]. A superior design for a beam chopper incorporates a chopping wheel rotated by a frequency-stablized DC motor.

C. Guide-Field Solenoids

Solenoids are used to control the polarization direction of the hydrogen beam and to prevent Majorana (diabatic) spin depolarization. All of these solenoids are powered by a set of four Kepco model JQE power supplies.

The first solenoid, mounted on the exit of the second hexapole magnet, is used to adiabatically rotate the atomic spin from radial within the hexapole magnet to longitudinal. This coil is 50.8 mm long and contains fifty loops wound in three layers on a stainless-steel form with a diameter of 15.9 mm.

A set of three solenoids located external to the tube connecting the hexapole-magnet chamber to the interaction chamber maintains the orientation of the atomic spin. A similar set of two solenoids between the interaction chamber and the analyzing magnet serves the same purpose.

A pair of coils located within the interaction chamber is used to maintain a guide field of ~100 mG at the interaction

---

[13]See Chapter Five, Section III.B for a description of the corrections to the ion signal due to this beam-loading effect.

point. The solenoid mounted on the entrance port for the hydrogen beam is 41.3 mm long and contains 38 thirty-eight loops wound in a single layer on a stainless steel form with a diameter of 22.2 mm. The solenoid mounted on the exit port for the hydrogen beam is 127 mm long and contains 120 loops wound in a single layer on a stainless steel form with a diameter of 25.4 mm.

A pair of rectangular coils located downstream of the post-interaction solenoid is used to rotate the atomic polarization from a longitudinal to a transverse direction in order to allow for the measurement of the beam polarization after it has passed through the interaction region. Each coil of the pair contains 52 loops on a 290-mm (horizontal) x 170-mm (vertical) aluminum frame. The pair, which is wired in series, is located external to the vacuum system with their magnetic dipole moments horizontal and perpendicular to the hydrogen beam. The upstream edge of the frames is located 215 mm upstream of the entrance to the analyzing magnet.

D. Analyzing Magnet & Associated Slits

The polarization of the hydrogen beam is measured by deflecting the beam in a pseudo-two-wire electromagnet (Ramsey 1956, pp. 399-401) (see Figure 3.14) and scanning the profile of the beam with a quadrupole mass analyzer (QMA) that acts as a detector of atomic hydrogen. (The QMA is described in the next section.) The pole faces are 101.6 mm long and have a minimum horizontal gap of 3.18 mm.

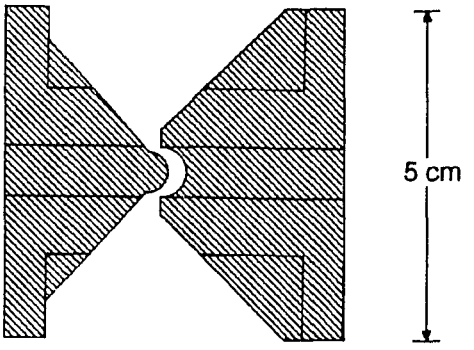

Figure 3.14 Cross-sectional scale drawing of analyzing magnet.

In order to prevent the hydrogen beam from colliding with the pole faces during transit, a set of stainless-steel collimators is used: a knife edge is mounted just in front of the entrance to the magnet and extends into the gap 0.7 mm from the convex pole tip; a 2.5-mm-high aperture is mounted directly in front of the knife edge; a pair of 0.5-mm-wide, 9.5-mm-high slits mounted on a tube connected to a linear-motion feedthrough are located upstream with the nearer (farther) slit 110 mm (160 mm) from the entrance to the magnet. The vertical slits are removed from the beam path except during polarization measurements. The narrow gap between the pole tips restricted the transmission of the beam to the QMA; therefore, the analyzing magnet was removed and replaced by a 38.1-mm-inner-diameter nipple after the polarization measurement was completed and before the ionization asymmetry measurement was begun.

E. Quadrupole Mass Analyzer

The hydrogen beam is monitored with a Vacuum Generators Supavac quadrupole mass analyzer (QMA) mounted just past the beam-dump chamber, a distance of 1.3 m from the interaction point. The QMA uses a Faraday cup and a high-gain amplifier to detect ions generated by electron bombardment at the input to the QMA. The entrance aperture of the QMA has an inner diameter of 6.4 mm. During polarization measurements, the entrance aperture is masked by a 0.5-mm-wide slit. The slit is removed for all other measurements. The QMA is also used for leak detection and residual-gas-pressure measurements as is an identical unit mounted on a branch of the O_2 line of the electron-source chamber. The use of thoria filaments to generate the electron-bombardment ionizing sprays reduces contamination of the ultra-high vacuum.

The maximum sensitivity of the QMA, as described by the manufacturer, is 2×10^{-11} mbar at which point the signal-to-noise ratio is 2:1. More sensitive, reasonably-priced QMAs have become available since this unit was purchased. These newer models use a channel electron multiplier for low pressure measurements while still using a Faraday cup for high pressure measurements, where the total pressure is the deciding factor. The greater sensitivity offered by these newer models would facilitate the measurements involved in this experiment including residual-gas-pressure measurements, polarization measurements and total beam intensity measurements.

The QMA at the end of the hydrogen-beam line is mounted on a linear translator, operated by a stepper motor under computer control, to allow the measurement of beam profiles during polarization measurements as well as background pressure measurements during ionization asymmetry measurements.

III. INTERACTION REGION

The region in which the electron beam interacts with the hydrogen beam is electrostatically shielded by a grounded, stainless-steel box, as shown in Figure 3.15. The box extends vertically from just above the grounded cover of the output optics of the monochromator to just below the ground shield of the Faraday cup. The entrance aperture for the hydrogen beam has a diameter of 6 mm which effectively defines the size of the hydrogen beam as it interacts with the electron beam; the size of the electron beam is defined by apertures in the output optics of the monochromator.

The grounded box also contains the Mullard model X919BL (closed output) channel electron multiplier (CEM) used to count the protons generated by electron-hydrogen scattering. The CEM cone is biased at -700 V to attract the protons; the CEM grid is biased at -650 V to prevent secondary electrons from escaping; the CEM output is biased at +1700 V. The biases are provided by three Power Designs, Inc. model AEC-5000B power supplies. The combination of the forward momentum

of the hydrogen beam and the CEM grid bias provides 4π-solid-angle detection of the generated protons. The efficiency of the CEM for proton detection is 12% with -700 V cone bias, according to the manufacturer. The three grids, each of which is 90% transparent, through which the protons must pass to reach the CEM reduce the effective efficiency to 10%.

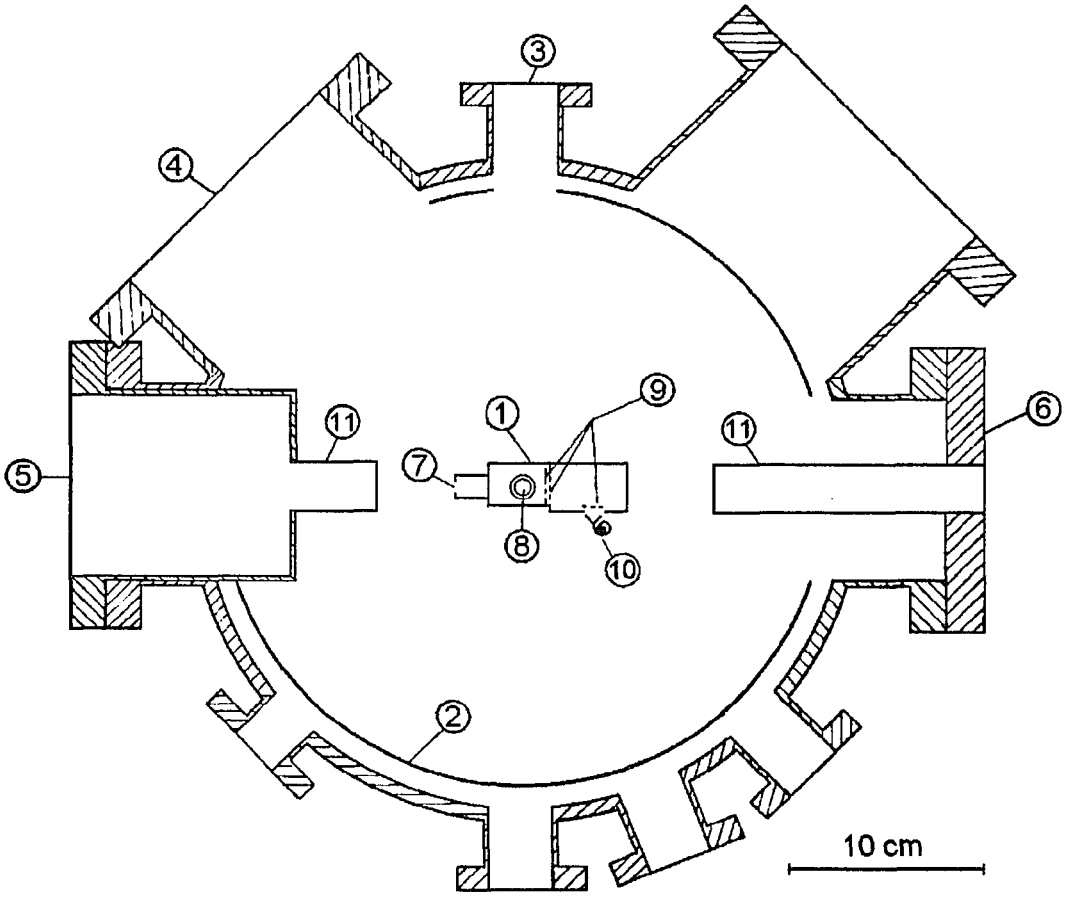

Figure 3.15 Scale drawing of the top view of the interaction chamber showing (1) grounded shield, (2) μ Metal, (3) ionization pressure-gauge port, (4) ion-pump port, (5) hydrogen-beam entrance port, (6) hydrogen-beam exit port, (7) hydrogen-beam aperture, (8) electron-beam aperture, (9) wire grids, (10) channel electron multiplier, and (11) guide-field solenoids.

The CEM is also sensitive to Lyman-α photons, with an efficiency of 5% according to the manufacturer, which contribute to noise in the measurement. This contribution is small, however, since metastable 2S atoms are quenched sufficiently upstream by the cone bias so that the solid angle for Lyman-α photon detection is minute. The solid angle for detection of Lyman-α photons generated by other sources is even less.

IV. VACUUM SYSTEM

The vacuum system is described in two sections: the first describes the chambers, pumps and operating pressures; the second describes the bakeouts of system.

A. Chambers, Pumps & Operating Pressures

The main chambers of the vacuum system are the electron-source chamber, the hydrogen-source chamber, the hexapole-magnet chamber, the interaction chamber, the post interaction chamber, and the beam-dump chamber. These chambers are represented in Figure 3.16.

1. Electron-source chamber

The electron-source chamber is a standard six-way cross with 150-mm-outer-diameter tubing and 200-mm-diameter flanges. A Perkin-Elmer model 207-0164 ion pump, with a pumping speed of 150 l/s, is connected to the chamber by a 150-mm-diameter formed bellows. The ion pump contains a pumping element with

extra titanium which pumps H_2 more efficiently than standard pumping elements. A Perkin-Elmer Digitel 500 controller is used with the pump.

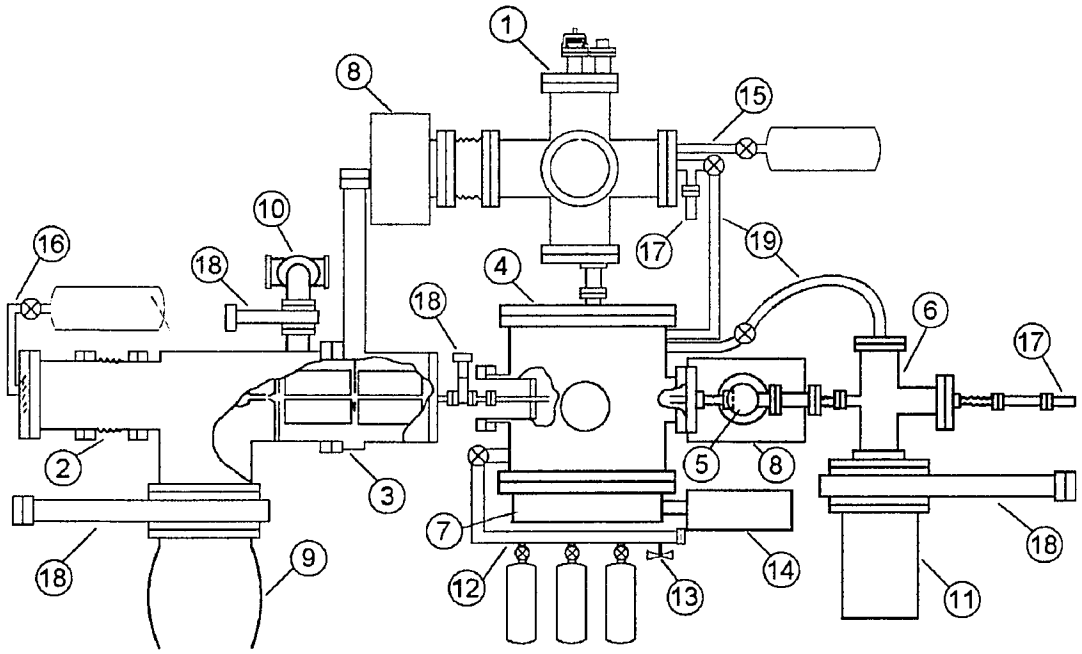

Figure 3.16 Schematic diagram of vacuum system showing (1) electron-source chamber, (2) hydrogen-source chamber, (3) hexapole-magnet chamber, (4) interaction chamber, (5) post-interaction chamber, (6) beam-dump chamber, (7) leak chamber, (8) ion pumps, (9) diffusion pump, (10) turbo pump, (11) cryopump, (12) sorption-pump manifold, (13) Venturi pump, (14) mechanical pump, (15) O_2 line, (16) H_2 line, (17) QMA heads, (18) gate valves, and (19) bypass lines. Not shown are an ion pump connected to the interaction chamber, and a connection between the O_2 line and the sorption-pump manifold.

Pressure can be monitored by three separate devices: the ion-pump controller, a Granville-Phillips model 274-023 ion gauge, and a Vacuum Generator Supavac QMA. The ion gauge is mounted in a tee with 38-mm-outer-diameter tubing so as not to

interfere with the operation of the polarized-electron source. The tee is mounted on the flange opposite the laser window. The ion gauge is attached to a Granville-Phillips 271-004 controller. The QMA is also mounted in 38-mm-outer-diameter tubing on a branch of a bypass line connected to the flange opposite the ion pump. During data acquisition, neither the ion gauge nor the QMA was operated in order to minimize outgassing and magnetic fields, but prior to data acquisition, the QMA indicated pressures an order of magnitude lower than those indicated by the ion-pump controller while the ion gauge indicated pressures approximately one third those indicated by the ion-pump controller. The ion gauge is the most accurate of the three gauges; therefore, the reading from the ion-pump controller, which was the only gauge operated during data acquisition, needs to be corrected by dividing by three. The corrected operating pressure during data acquisition was typically 3×10^{-10} Torr.

Other connections to the electron-source chamber include an MDC model VP-600 viewport for laser transmission; a linear-motion feedthrough on which is mounted the GaAs cathode; electrical feedthroughs for the electron optics, GaAs cathode, thermocouple and molybdenum rod; the O_2 line; and a formed bellows connecting the electron-source chamber to the interaction chamber. All subflanges are half nipples welded into the main flanges. All flanges are sealed by OFHC copper gaskets. The chamber is supported by three stiff springs

supported by the aluminum laser table which is supported by the interaction chamber.

2. Hydrogen-source chamber

The hydrogen-source chamber is pumped by a Innotec Group, Inc. (formerly Torr Vacuum Products) model S-1000 oil diffusion pump with an effective pumping speed 2500 l/s for H_2, which accounts for essentially all of the load except when first pumping down from atmosphere in which case the effective pumping speed for air is 1160 l/s. In preliminary measurements when the system was operating under conditions typical of data acquisition, the pressure in the source chamber was of the order of 10^{-7} Torr, as measured on a Granville-Phillips ionization gauge connected to a Granville-Phillips model 260 controller. During data acquisition, the pressure in the chamber was monitored only by a thermocouple (TC) gauge with a maximum sensitivity of 0.1 mTorr. The TC registered 0.0 mTorr during normal operation.

3. Hexapole-magnet chamber

The hexapole chamber is pumped by a Balzers model TPU 200 turbomolecular pump with effective pumping speeds of 200 l/s for H_2 and 100 l/s for air. During data acquisition, the operating pressure in the chamber was typically 2×10^{-8} Torr, as measured by a Granville-Phillips ion gauge connected to a Granville-Phillips model 260 controller.

4. Interaction chamber

The interaction chamber is pumped by a Perkin-Elmer model 207-0284 ion pump with effective pumping speeds of 500 l/s for

H_2 and 160 l/s for air. These speeds include the effects of a baffle placed in the entrance of the pump in order to prevent ions and electrons generated in the pump from reaching the CEM. The pressure in the interaction chamber could be measured either by a Granville-Phillips model 274-023 ion gauge connected to a Granville-Phillips series 271 controller or by the current in the ion pump controller. The ion gauge readings are more accurate. During data acquisition, the ion gauge was not used so that it would not generate a magnetic field and ions which might interfere with the experiment. Typical ion-pump currents during data acquisition correspond to ion gauge readings of 3×10^{-9} Torr.

As a result of a fabrication error, the bottom flange of the interaction chamber leaked. Because many feedthroughs are connected to the flange, it was decided, in the interest of time and money, to create a vacuum outside the leaks rather than fabricate a replacement. A chamber (labelled the "*leak chamber*" in Figure 3.16) formed from an 200-mm-high section of 300-mm-diameter pipe covered by a brass plate covered the leaks. The leak chamber is pumped by a Varian model SD-300 mechanical pump.

5. Post-interaction chamber

The post-interaction chamber is pumped by a Perkin-Elmer model 207-0164 ion pump with effective pumping speeds of 315 l/s for H_2 and 115 l/s for air. The pump is connected to a Perkin-Elmer Ionpak 200 power supply. The pressure in the chamber could be determined only by the pump current, which is

not a very accurate measure. The current was typically 1 μA, corresponding to a pressure of the order of 10^{-9} Torr.

6. Beam-dump chamber

The beam-dump chamber is pumped by a CTI Cryogenics model Cryo Torr 7 cryopump with an effective pumping speed of 1000 l/s for both H_2 and air. The pressure in the chamber is measured by the QMA and was typically 4×10^{-9} mbar (3×10^{-9} Torr) during data acquisition.

B. Bakeout

The electron-source chamber and the interaction chamber were baked out several times before data acquisition. It was determined that baking out the scattering chamber at ~150°C exasperated the leaks on the bottom flange, so it was decided to stop baking out the scattering chamber. For final bake out of the system, only the electron-source chamber was baked out. The chamber was baked at ~175°C for four days. The ion pump was not heated directly, but its temperature rose to ~60°C due to indirect heating. Earlier bakeouts had been at ~200°C, including the ion pump.

V. COMPUTERS & INTERFACING

Two computer systems are used in this experiment: an LSI-11/23 used for data acquisition and a VAX 780 used for data analysis and simulation programs. Data is transferred between the two systems using the program KERMIT.

A. LSI-11/23

Most data acquisition is controlled by computer programs executed on an LSI-11/23 microcomputer. The ADAC Corporation model 1000-M-60-110 computer has 256kb of RAM and includes the following auxiliary boards: a model 1012-16SE-A-3-P sixteen-channel analog-to-digital converter (±10 V to 12 bits at 35 kHz), two model 1412DA-4-A-V-O-P four-channel digital-to-analog converters (12 bits to ±10 V), a model 1601GPT programmable crystal-clock/general timer, a model 1604/POC-4 four-output pulse generator (used to drive stepper motors), and two model 1604/OPI-4 four-input pulse counters with optically-isolated inputs. The system runs off two floppy drives: it does not include a hard drive.

The computer runs on the RT-11SJ (S) V04.00F operating system. The programs are written in FORTRAN IV V2.1 and MACRO-11 languages. The latter is an assembly language. Data files are transferred to a VAX 780 computer for data analysis. The transferred is controlled by the KERMIT-11 T2.18 program. The data files, along with the control programs, are also saved on floppy disks, and hard copies are printed out.

The computer interface is shown schematically in Figure 3.17. Each of the boxes labelled "*blind counters*" corresponds to two inputs (counters) on a 1604/OPI-4 board. One counter is used with the hydrogen beam present, while the other is used with the beam blocked, as explained in Chapter Four. The CEM produces rounded pulses which are amplified and formed into logic pulses by an Ortec model 473A constant

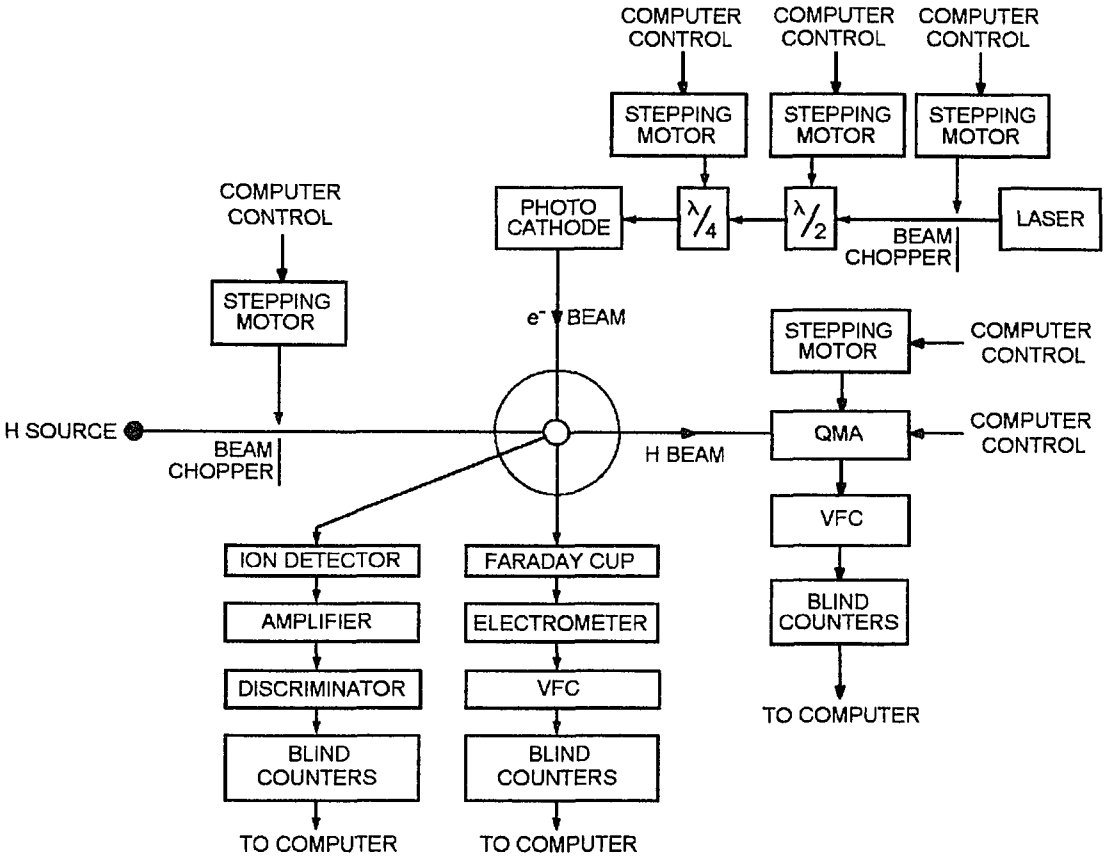

Figure 3.17 Schematic diagram of the computer interface used to control and monitor the experiment. VFC stands for voltage-to-frequency converter.

fraction discriminator, as shown in more detail in Figure 3.18. The Faraday cup is connected to a Keithley Instruments model 621 electrometer which provides a voltage output proportional to the current input. This voltage is converted to logic pulses by a voltage-to-frequency converter (VFC) built at Yale University. The VFC has a conversion factor of ~2kHz/V. The QMA provides a voltage output which is converted to logic pulses by a Canberra model 159 VFC with a conversion factor of 10 kHz/V.

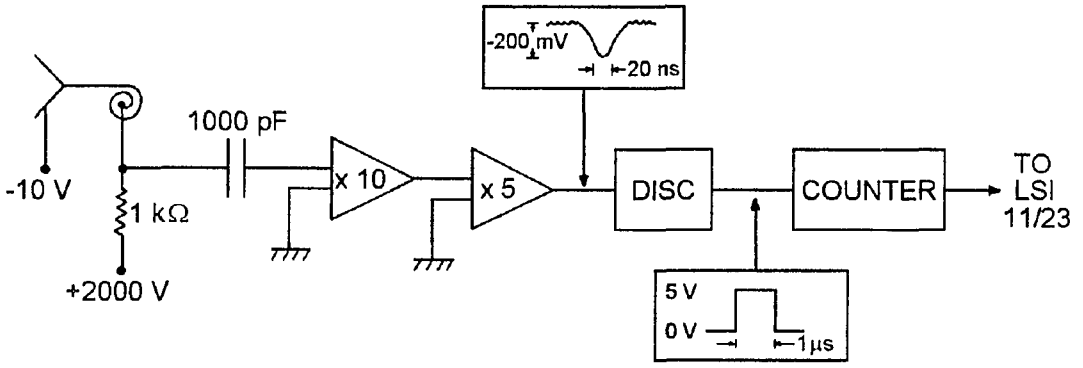

Figure 3.18 Detailed schematic diagram of the computer interface to the channel electron multiplier. The waveforms before and after the discriminator are also shown.

B. Vax 780

The data is analyzed on a Vax 780 computer built by Digital Electronics Corporation (DEC). This computer runs on the 4.3 BSD Unix operating system. The analysis programs are written in the FORTRAN 77 language. The Monte Carlo simulation discussed in Chapter Four was executed on a DEC Celerity computer, which uses four Motorola model 68020 CPUs. The programs, analyzed data files, and output files are saved on nine-track tape.

CHAPTER FOUR: DATA ACQUISITION

The data-acquisition procedures used in the measurements of hydrogen-beam and electron-beam parameters and ionization asymmetries are described in this chapter; the procedures used to analyze the acquired data are described in Chapter Five; the results of the analyses are presented and discussed in Chapter Six.

I. HYDROGEN BEAM

The data-acquisition procedures for the measurement of three parameters of the hydrogen beam at the interaction point are described in this section: the electron-spin polarization, the atomic density, and the dissociation fraction. These measurements have already been described in Chan *et al* (1988); therefore, only a brief outline is given here.

A. Polarization

The data necessary for the determination of the electronic polarization of the hydrogen beam at the interaction point are a set a beam profiles with different settings of hydrogen-source rf power, analyzing-magnet driving currents, I_D, (and consequently magnetic fields), and QMA mass tunings. These profiles are obtained by translating the QMA across the beam in 0.125-mm steps, repeatedly sampling the QMA signal at each step. It is necessary to wait after each step

for vibrations to decay before sampling the QMA output. A delay of 4.5 s was used. The QMA output was sampled 9000 times at each step, with a delay of 2 ms between samples. The computer program calculates the mean and standard deviation of these 9000 readings, assuming Gaussian statistics, and records these as a function of the QMA position.

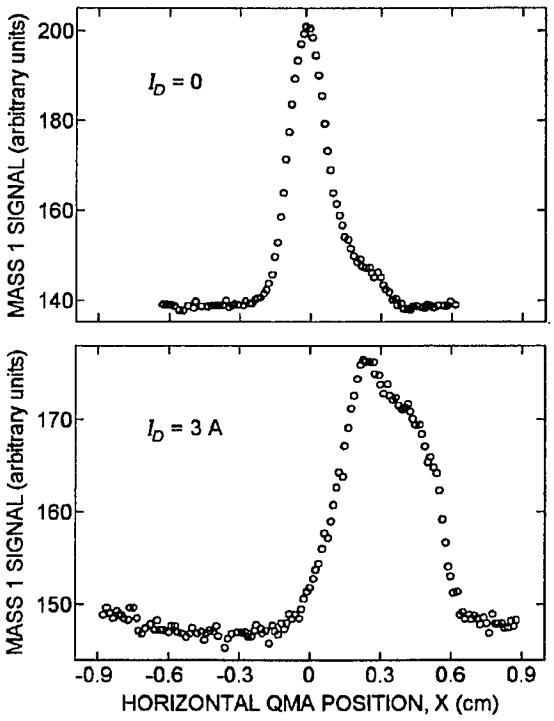

Figure 4.1 Plots of two Q_1^{on} profiles showing the shift and broadening of the beam when the analyzing magnet is energized.

The primary profiles (see Figure 4.1), hereafter referred to as Q_1^{on} profiles, are taken with the rf on and the QMA tuned to mass one. The current I_D is varied from one Q_1^{on} profile to the next. The currents generate fields that vary between zero (no deflection) and a value that causes the edge of the beam to scrape the pole pieces of the analyzing magnet. Three

additional profiles, all taken with zero field[14] in the analyzing magnet, are necessary in order to correct for dissociative ionization in the QMA: a Q_2^{on} profile taken with the rf on and the QMA tuned to mass two, a Q_1^{off} profile taken with the rf off and the QMA tuned to mass one, and a Q_2^{off} profile taken with the rf off and the QMA tuned to mass two. The complete set of profiles was acquired in a quasi-random order to minimize extrapolation errors (see Figure 4.2). Each profile required ~1 h of data aquisition; the entire set was acquired in one continuous 15 h period on the night of 13-14 December 1987. Although this date is nearly 1.5 years before asymmetry data acquisition began, the value of the polarization should be stable.

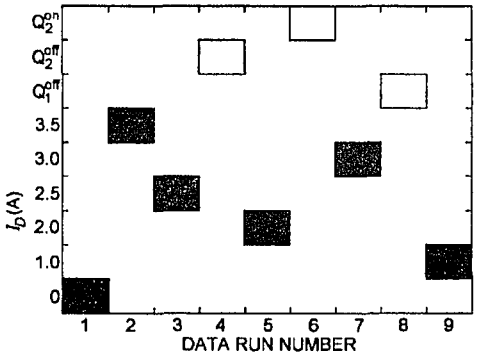

Figure 4.2 Graph showing the quasi-random order in which polarization data files were acquired. Filled boxes are Q_1^{on} profiles.

The complete set of slits are used in the acquisition of the profiles: the two slits upstream of the analyzing magnet and the mask mounted on the input of the QMA. The former

---

[14]A current of 2.5 A was accidently left on during the Q_2^{off} profile; however, the molecular beam is insensitive to the magnetic field.

minimize scattering off the pole pieces of the analyzing magnet; the latter increases the spatial resolution of the profiles. These slits, as well as the entire analyzing magnet, were removed after the polarization data were acquired.

A computer program running on the LSI-11/23 controls the data acquisition; however, the hydrogen-source rf power and I_D are changed manually between profiles. In addition, the QMA scale and the pressure in the hydrogen discharge tube are set manually and remain constant throughout the entire set of profiles: the former at 10^{-10} mbar; the latter at 400 mTorr.

The computer controls the mass setting of the QMA via a voltage from a DAC. Before scanning for the profiles, it is necessary to determine the digital values corresponding to 1 u/e and 2 u/e. This determination is achieved by successively sending all digital values in the range from 1 to 50 and monitoring the QMA output, a process hereafter referred to as "*taking a mass profile*". The digital values corresponding to the first two peaks are recorded, and the appropriate value is entered at the beginning of each profile. This determination was done once at the beginning of the data acquisition process.

Between profiles, the QMA is always returned to the same position, $x_0 = 0$, which is near the centroid of the undeflected beam. In order to prevent backlash, it is necessary to translate the QMA in the same direction between sampling positions; therefore, the QMA is first moved 1.25 mm

Table 4.1 Number of steps on either side of x_0.

PROFILES	# STEPS/SIDE
Q_1^{on}(0 A), Q_1^{off}, Q_2^{on}, Q_2^{off}	50
Q_1^{on}(1 A)	60
Q_1^{on}(2 A), Q_1^{on}(2.5 A), Q_1^{on}(3 A), Q_1^{on}(3.5 A)	70

beyond the extreme data-acquisition position in one direction and then brought back those 1.25 mm before sampling is started. Translation then proceeds in the same direction until the opposite extreme data-acquisition position is reached, after which the QMA is returned to x_0 to await the beginning of the next profile. Within each profile, the number, #, of steps is the same on either side of x_0. Three different values of # were used for different profiles as listed in Table 4.1.

B. Density

Two separate determinations, based upon two separate measurements, were made of the average density of the atomic hydrogen beam at the interaction point. During both sets of measurements, the hydrogen-source rf power was on and the pressure in the hydrogen discharge tube was 400 mTorr.

The first determination of the density is based upon the increase in pressure in the interaction chamber due to the presence of the hydrogen beam. The hydrogen-beam chopper was controlled manually. The pressure was measured on the interaction-chamber ion gauge.

The second determination of the density is based upon the angle-integrated ion production rate due to electron-impact ionization. The data-acquisition procedure for this measurement is described in Section III. The ion production rate at an incident electron energy of 15 eV was used for the density determination. The data, acquired during preliminary tests in 1986, is not included in the asymmetry results reported in this dissertation, but the same data-acquisition procedure was used.

C. Dissociation Fraction

The dissociation fraction at the exit of the hydrogen-source discharge tube is determined from measurements at the beam-dump QMA. Mass-two signals are measured with the hydrogen-beam chopper open and closed, and with the hydrogen-source rf power on and off. Data acquisition is controlled by a computer program running on the LSI-11/23. The output of the QMA is sampled fifty times at each setting. The mean and standard deviation of these fifty values are calculated and recorded. First, a mass profile is taken to determine the digital value corresponding to 2 u/e. The rf-on data is acquired first, with the chopper first closed, then open; the rf-off data is acquired second, again with the chopper first closed, then open. The rf power is turned on and off manually. There is a 250-ms delay after changing the chopper position in order to allow vibrations to dissipate; there is a 7-ms delay between each of the fifty samples. The entire

process takes only a few minutes. The QMA was set on the 10^{-10}-mbar scale.

II. ELECTRON BEAM

The data-acquisition procedures for measurement of the energy of the electron beam are described in this section. Separate, but similar, procedures are used for the determination of the mean energy and of the standard deviation in the energy of the electron beam. These measurements have been described previously in Guo *et al* (1990a) and Guo (1991, pp. 79-88); therefore, again only a brief outline is given here. The polarization of the electron beam is determined using the results of the ionization asymmetry measurements. The procedures used in the acquisition of the asymmetry data are described in Section III.

A. Mean Energy

As a result of contact potentials and the electron affinity of the GaAs crystal, the mean energy of the electron beam, $\overline{E}_e$, is not simply eV_c, where e is the elementary charge and V_c is the voltage applied to the crystal. The offset energy, $\overline{E}_{offset} \equiv eV_c - \overline{E}_e$, is determined by measuring the ionization of molecular hydrogen near its ionization threshold of 15.43 eV. The cross section is measured at 0.1 V intervals for crystal biases in the range 18.3-19.0 V. With the hydrogen-source rf power off, the ion count rate, electron

current and QMA mass-two signal are measured with the hydrogen beam alternately open and closed, typically for a total of 2 min at each bias. The entire process takes ~20 min. The orientation of the retardation plates is kept constant throughout this process, and the laser chopper is not used. Initially, these measurements were performed manually using external counters; however, starting 9 June 1989 the LSI-11/23 controlled all parameters except the crystal bias. The quantity $\overline{E}_{offset}$ was determined after each crystal reactivation and at least once every one to three days in between reactivations if data were acquired in the near-threshold region, where precise knowledge of $\overline{E}_e$ is critical. Sometimes up to four sets of measurements were taken in a row and the results averaged.

B. Standard Deviation in Energy

The data-acquisition procedure for the determination of the energy spread of the electron beam is similar to the procedure described in the last section for determining $\overline{E}_{offset}$, except that the ionization cross section for atomic hydrogen is used instead of that for molecular hydrogen. The cross section was measured at nine energies within 300 meV of threshold. The mean energy of the beam is first calibrated using the procedures outlined in the previous section. With the hydrogen-source rf power on, ion counts, electron current and QMA mass-one signal are measured with the hydrogen-beam chopper alternately open and closed. Again, the orientation

of the retardation plates is kept constant and the laser chopper is not used. This procedure, which was performed only once, was controlled by the same computer program used to determine $\overline{E}_{offset}$.

III. IONIZATION ASYMMETRY

Two slightly different procedures are used in the acquisition of data for the determination of the ionization asymmetry: a simpler one below the H_2 ionization threshold and a more complicated one above the H_2 ionization threshold. The simpler procedure, which is a subset of the more complicated procedure, is described first.

A. Near Threshold

The primary data for the determination of the asymmetry were acquired using the following three instruments: (1) the channel electron multiplier (CEM) for measuring the number of H^+ ions (protons), (2) the electrometer attached to the Faraday cup for measuring the intensity of the polarized-electron beam, and (3) the quadrupole mass analyzer (QMA) for measuring the intensity of the hydrogen beam. In order to correct for background signal, it is necessary to take readings with the electron beam and/or the hydrogen beam absent from the interaction region in addition to the primary data with both beams present. The QMA sampled the residual gas in the beam dump while the electron beam was off. This

sampling was accomplished by translating the QMA off to the side of the hydrogen beam while the electron beam was off and then translating back to the center of the hydrogen beam before turning the electron beam back on. During the course of data acquisition, it was noticed that the background ion signal with the laser blocked (and the electron beam, therefore, absent) was too small to affect the measurements, within their experimental accuracy; therefore, it was decided about halfway through the data acquisition to stop blocking the laser so that more primary data could be collected in the same amount of time (see Figure 4.4). The sampling of residual gas was continued, however.

The data were acquired under the control of computer programs executed by the LSI-11/23 microprocessor. The subroutines responsible for i/o functions were written in assembly language; the main program was written in FORTRAN IV, as were some subroutines responsible for determining values to send to the assembly-language subroutines; another subroutine, which calculates means and standard deviations, was also written in FORTRAN IV. An important note concerning the programming is that no interrupts were used. The timing of all processes was determined by using a delay subroutine which set a clock to start counting down from a set time and then used a closed loop to repeatedly test the clock's control/status register until it indicated that the time was zero.

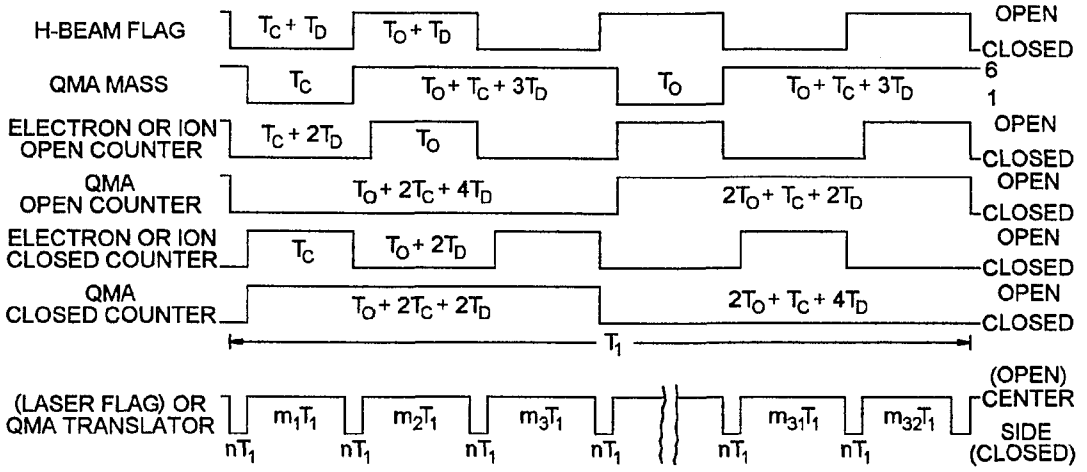

Figure 4.3 Timing diagram for control signals in the near-threshold region. T_O (T_C) is the data open (closed) time; T_D is the delay after toggling the hydrogen-beam chopper plus the time (40 ms) to actually toggle the chopper; $T_1 = 3T_O + 3T_C + 6T_D$ is the period of one data-acquisition cycle; n is the number of cycles with the laser blocked; m_i is the number of cycles at the i^{th} orientation of the retardation plates.

A total of six blind counters were used to collect data, two for each of the primary data types, one with the hydrogen beam present, the other with the hydrogen beam blocked. Figure 4.3 shows the timing of signals controlling the acquisition of near-threshold data in these counters. The QMA mass tuning of 6 u/e is used because the response time of the QMA is approximately 1 s when set at the pressure ranges necessary for precise measurement of the 1 u/e signal. The QMA needs to have negligible input signal while it has time to integrate the response to the 1 u/e signal. The smallest, and therefore most convenient, setting with negligible input signal is 6 u/e.

```
DO YOU WANT A MASS PROFILE?
ENTER QMA CODE FOR ATOMIC HYDROGEN:
ENTER QMA CODE FOR MOLECULAR HYDROGEN:
ENTER ELECTRON ENERGY (IN EV):
ENTER RF CONDITION CODE (0 FOR OFF, 1 FOR ON):
ENTER GUIDE FIELD DIRECTION CODE (0 FOR RED, 1 FOR GREEN):
ENTER DATA OPEN TIME (IN MILLISECONDS):
ENTER DATA CLOSED TIME (IN MILLISECONDS):
ENTER DELAY AFTER CHOPPER (IN MILLISECONDS):
ENTER QMA SCALE (MBAR)(E FORMAT):
ENTER ELECTROMETER FULL SCALE READING (A):
ENTER TOTAL ION COUNT/ORIENTATION:
ENTER NUMBER OF CYCLES WITH LASER BLOCKED:
ENTER OUTPUT FILENAME:
ENTER 1 FOR MASS ONE ONLY, 2 FOR ALTERNATING MASS ONE AND TWO:
IS THE SYSTEM READY TO BEGIN DATA ACQUISITION?
```

Text Box 4.1 Questions asked by the data-acquisition program as they would appear on the video monitor.

The main program begins by printing a series of questions on the monitor (see Text Box 4.1) and waiting for responses from the keyboard. It first asks whether it should take a mass profile. A mass profile was taken at the beginning of each day, but usually was not repeated on subsequent data runs on the same day. The value of the center of each mass peak was one of two numbers. The variation was most likely the result of temperature fluctuations. The main program then asks for the digital values corresponding to the mass peaks for 1 u/e and 2 u/e. About halfway through the data acquisition, an air conditioner in the lab broke down resulting in high and unstable room temperatures which caused the tuning of the QMA to become unstable. A voltage divider was installed (cf. Figure 4.4) between the DAC in the LSI-11/23 and the input of the QMA in order to stabilize the tuning. It was decided to keep the voltage divider installed even after the air conditioner was fixed.

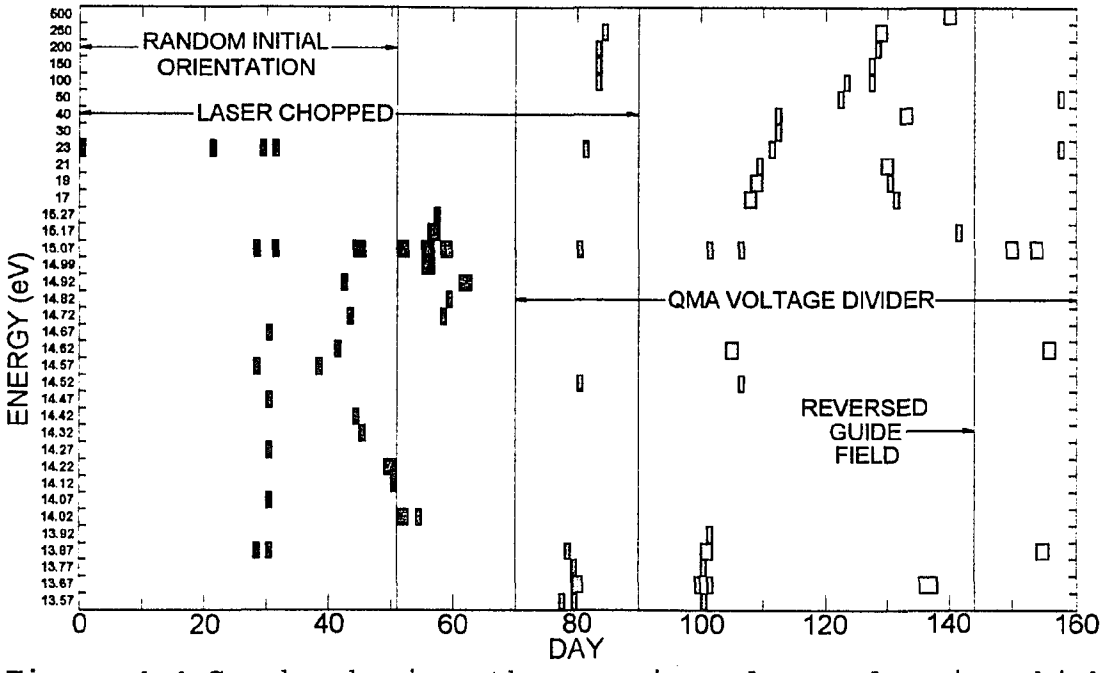

Figure 4.4 Graph showing the quasi-random order in which electron energy was varied. Day 1 is 2 May 1989. The other notations are explained in the text.

The main program then asks for the mean energy (eV) of the electron beam. The electron energy is constant within each data run. Often, the energy was kept the same for several data runs in a row; on other occasions, the energy was changed between every run. A quasi-random order of electron energies was used in order to minimize systematic errors in the asymmetry spectrum (Figure 6.1 and Figure 6.3). Figure 4.4 shows the order in which energy was varied. Note that data was acquired repeatedly at 15.07 eV over the course of the experiment for the purpose of monitoring secular drifts in the response of the equipment.

The main program then asks whether the rf generator in the hydrogen source is on, with a "0 (1)" indicating that it is off (on). The rf power was always on during data

acquistion in the near-threshold region. Next, it asks for the polarity of the magnetic guide field in the interaction region, with a "0" ("1") indicating that the polarity is parallel (antiparallel) to the momentum of the hydrogen beam. (Red and green are the colors of the indicator lights on the switch box used to control the guide-field polarity.) The polarity was parallel for the first 142 days and was antiparallel for the final 15 days (see Figure 4.4).

The main program then asks how long data should be collected each time the hydrogen beam chopper is open, how long data should be collected each time the hydrogen beam chopper is closed, and how long to wait after opening or closing the chopper before starting data collection. The toggling of the chopper was found to induce vibration in the apparatus which caused the hydrogen beam to be unstable for a brief period. Thus it was necessary to incorporate a delay before data acquisition. Typical times were 1000 ms each for data collection with a 125-ms delay after toggling the beam chopper. Note that these times are independent of each other: the delay time is not subtracted from the data-acquisition times.

The main program then asks for the scales used on the QMA and the electrometer used to measure the intensity of the electron beam. These scales were always kept as sensitive as possible in order to maximize the counting rate and thus minimize the relative error due to counting statistics.

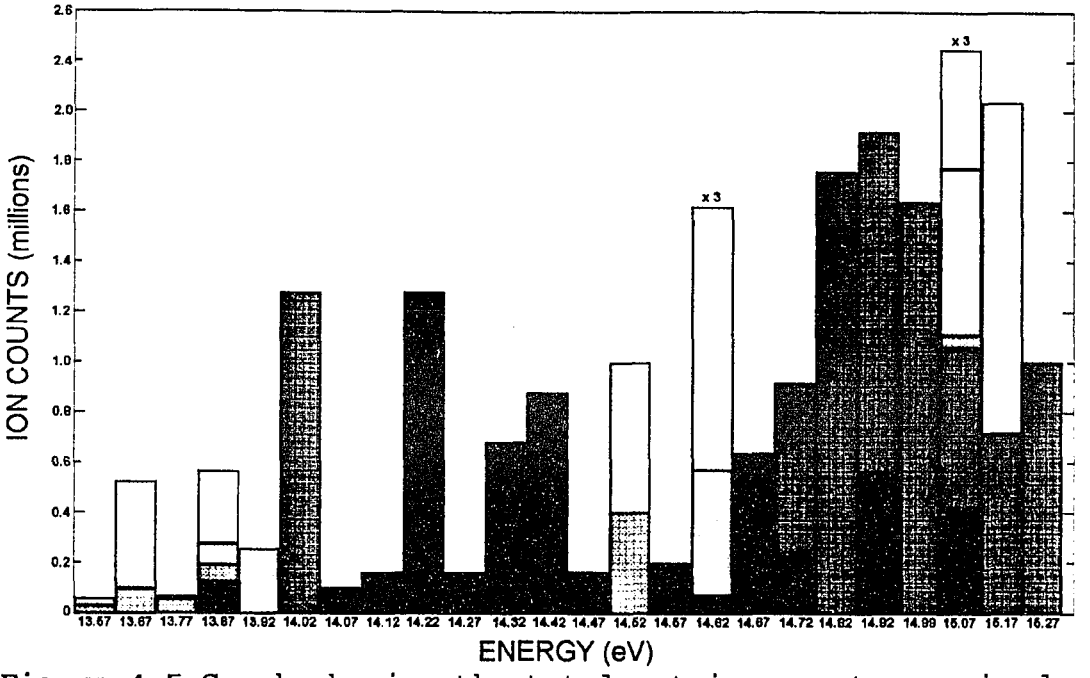

Figure 4.5 Graph showing the total net ion counts acquired at each electron energy in the near-threshold region. The shadings correspond to those in Figure 4.4.

The main program then asks how many ion counts it should acquire at each orientation of the combination of the quarter-wave and half-wave plates. The main FORTRAN IV subroutine that controls the actual data acquisition keeps a running total of the net ion counts at each orientation. When this total exceeds the amount entered in response to this query from the main program, the subroutine stops data acquistion until it calls subroutines to rotate the quarter-wave and/or half-wave plates. The running total of net ion counts is zeroed before data is acquired at this new orientation. The total net ion counts at each energy in the near-threshold region, summed over all orientations and all data runs, is shown in Figure 4.5.

30MY89.D02
ELECTRON ENERGY = 14.5 EV
LASER-BLOCKED CODE = 3
INITIAL HALF-WAVE-PLATE ORIENTATION = 3
INITIAL QUARTER-WAVE-PLATE ORIENTATION = 1
QMA SCALE = 0.1E-09 MBAR
ELECTROMETER FULL SCALE READING = 0.1E-06 A
DATA OPEN TIME = 1000 MS/READING = 3000 MS/LINE
DATA CLOSED TIME = 1000 MS/READING = 3000 MS/LINE
DELAY AFTER CHOPPER = 125 MS
TOTAL ION COUNT/ORIENTATION = 2000.
NUMBER OF CYCLES WITH LASER BLOCKED = 3

	------OPEN------			-----CLOSED-----			
CODE	ION	ELECTRON	QMA	ION	ELECTRON	QMA	LINE
3	7	581.	18898.	8	580.	13158.	1
3	8	578.	18479.	7	580.	12794.	2
3	8	560.	18481.	6	559.	12578.	3
218	244	13831.	37581.	39	13974.	13431.	4
218	229	13206.	37863.	39	13039.	13432.	5
218	222	12680.	37377.	31	12394.	13262.	6
218	223	12435.	37422.	38	12541.	13144.	7
218	298	14467.	37198.	46	14016.	13070.	8
218	247	14725.	37230.	39	14718.	13089.	9
218	229	14748.	37336.	42	14725.	13445.	10
218	251	14646.	36963.	47	14561.	12997.	11
218	286	14473.	37142.	46	14411.	13311.	12
218	230	14593.	36897.	46	14665.	13069.	13
3	4	550.	19084.	5	554.	13272.	14
3	3	537.	19046.	6	537.	13255.	15
3	8	564.	19112.	4	558.	12964.	16
220	208	13252.	38108.	45	12570.	13873.	17
220	227	14438.	37827.	48	14410.	13651.	18
220	213	14344.	37614.	53	14378.	13542.	19
220	243	14469.	38132.	34	14422.	13727.	20
220	248	14651.	37723.	45	14583.	13780.	21
220	223	14661.	38124.	52	14694.	13659.	22
220	243	14697.	37473.	43	14681.	13625.	23
220	229	14729.	37791.	42	14660.	13617.	24
220	259	14593.	37483.	49	14579.	13487.	25
220	227	14498.	37779.	31	14436.	13576.	26
220	203	14600.	37568.	47	14609.	13655.	27
3	5	677.	19350.	3	673.	13848.	28
3	10	688.	19132.	4	686.	13500.	29
3	6	719.	19214.	3	714.	13279.	30
222	248	14430.	38482.	40	14372.	14172.	31
222	286	14428.	38207.	60	14473.	13781.	32
222	270	14479.	38190.	44	14384.	13611.	33
222	250	14544.	37912.	54	14473.	13933.	34
222	264	14441.	38006.	40	14417.	13888.	35

Text Box 4.2 Beginning of a typical printout of raw data in the near-threshold region.

Text Box 4.2 shows the beginning of a typical printout of raw data in the near-threshold region. The header, which appears only at the beginning of the data file, includes most of the information entered in response to the questions in Text Box 4.1: the data filename, the electron energy, the QMA and electrometer scales, the data acquisition and delay times, the total ion counts per orientation, and the number of cycles with the laser blocked. The laser-blocked code, L, is related to the rf condition code, R, and the guide-field direction code, G, as follows:

$$L \equiv R + 2G. \tag{4.1}$$

The code listed in the left-most column of the data is L if the laser is blocked; otherwise it is defined by

$$CODE = 3 + M + 2H + 16Q + 64L, \tag{4.2}$$

where M is the QMA mass tuning (1 or 2), H is a code (0 to 7) indicating the orientation of the half-wave plate (HWP), Q is a code (0 to 3) indicating the orientation of the quarter-wave plate (QWP), and L is the laser-blocked code (0 to 3) as before. The purpose of the 3 is to avoid degeneracies with L.

The second, third and fourth columns are the ion, electron and QMA signals, respectively, with the hydrogen-beam chopper open; the fifth, sixth and seventh columns are the corresponding signals with the hydrogen-beam chopper closed. Each line of data corresponds to one data acquisition cycle in Figure 4.3: each ion and electron count listed is the sum over three sampling periods; each QMA count in the sum over one sampling period.

The retardation plates are always rotated in the same direction in order to avoid backlash: the HWP in 45° steps; the QWP in 90° steps. For the orientations used, the laser light incident on the HWP has its linear polarization vector either aligned with one of the optical axes of the half-wave plate or at 45° to the axes; the light incident on the QWP has its polarization vector at 45° to the axes.

For the first 51 days of data acquisition, the initial orientation of the retardation plates was set randomly (see Figure 4.4) for the purpose of minimizing systematic errors due to secular drifts during the course of a single data run. A true random number generator was constructed by twice sampling the QMA output for 1 s each with the QMA tuned to 2 u/e. The initial orientation of the QWP (HWP) is the two (three) least-significant binary bits of the first (second) sample. After the first 51 days, it was decided to start all data runs with the same initial orientation of the retardation plates for two reasons: (1) secular drifts were negligible and (2) the analysis, via false asymmetries, of systematic errors due to the retardation plates is greatly simplified by always using the same initial orientation.

The rotation of the plates then proceeds as follows: the QWP is held at its initial orientation while the HWP is rotated 360° in eight steps; the QWP is then rotated 90° and held at this new orientation while the HWP is again rotated 360° in eight steps; this procedure is repeated twice more; finally, the QWP is rotated 90° again to its initial

orientation. At this point, the QWP has been rotated a total of 360° and the HWP has been rotated a total of 1440°, or four complete rotations, for a total of thirty-two combinations of retardation-plate orientations.

Each data run begins and ends with "*laser-blocked code data acquisition*" (LBCDA). In addition, LBCDA occurs immediately following each rotation of the retardation plates. As noted earlier, it was decided about halfway through the data acquisition to stop blocking the laser. During the first half of the experiment, the laser was blocked and the QMA was moved off to the side of the hydrogen beam during LBCDA; during the second half, the laser was no longer blocked, but the QMA continued to be moved during LBCDA.

B. Above H_2 Ionization Threshold

The primary data-acquisition procedure is the same above the ionization threshold of H_2 as in the near-threshold region, except that additional data is acquired with the QMA tuned to 2 u/e (see Figure 4.6). Text Box 4.3 shows the beginning of a typical printout of raw primary data in the higher-energy region. Note that each data-acquisition cycle now results in two lines in the data file: one for mass one and another for mass two. The total net ion counts at each of the higher energies is shown in Figure 4.7.

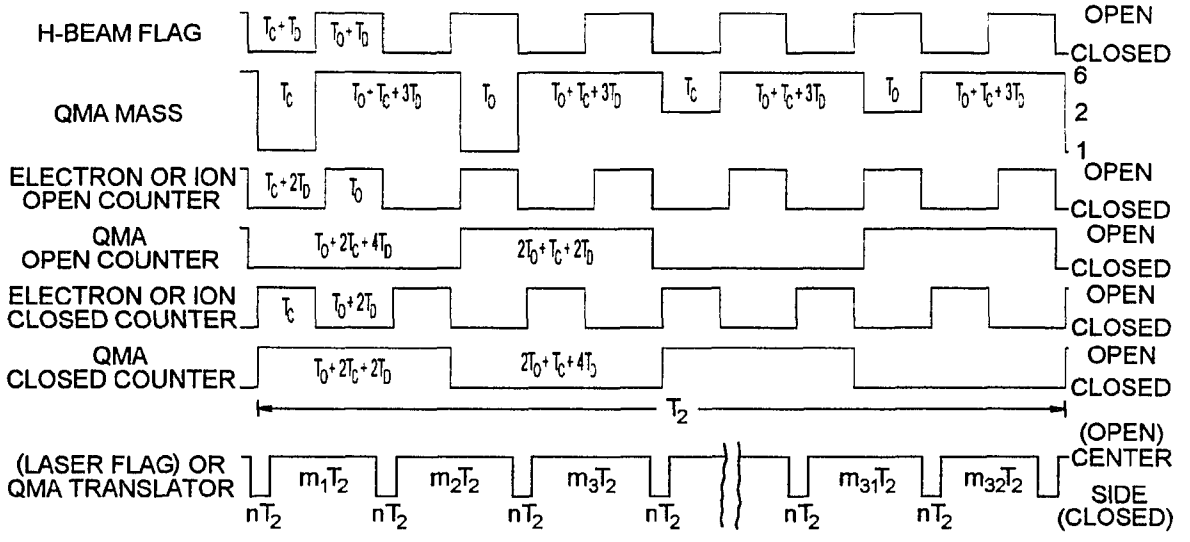

Figure 4.6 Timing diagram for control signals above the ionization threshold for H_2. The symbols have the same meaning as in Figure 4.3, except that $T_2 = 6T_O + 6T_C + 12T_D$ is the new period of one data-acquisition cycle.

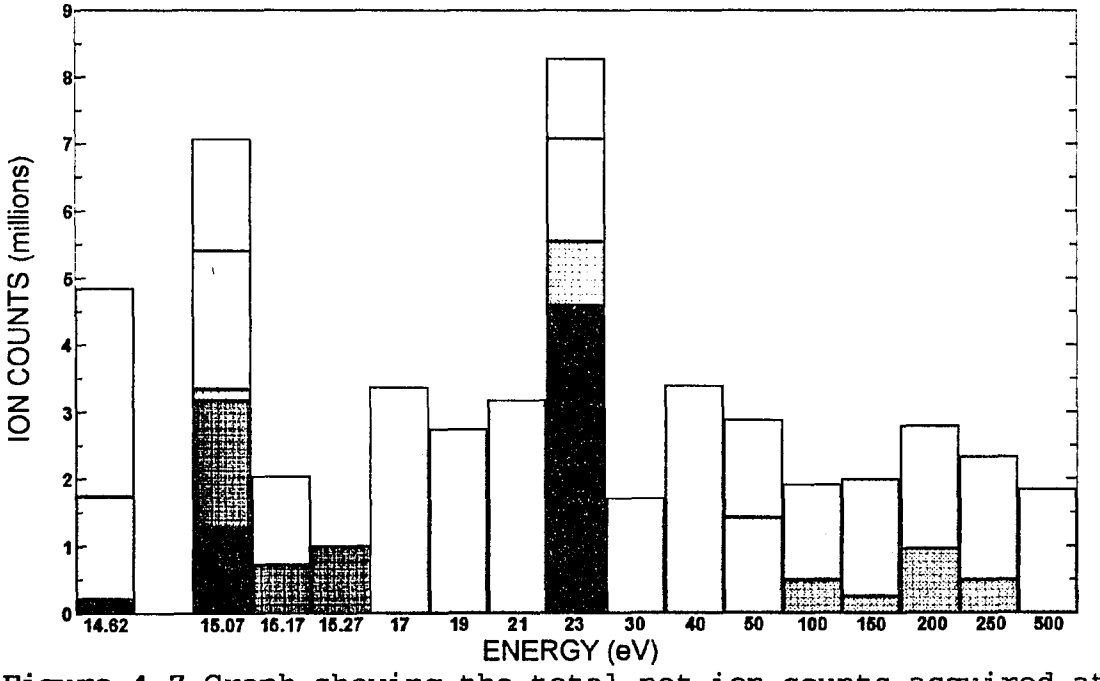

Figure 4.7 Graph showing the total net ion counts acquired at each electron energy above 15 eV. The shadings correspond to those in Figure 4.4.

09ST89.D01

ELECTRON ENERGY = 21.00 EV
LASER-BLOCKED CODE = 3
INITIAL HALF-WAVE-PLATE ORIENTATION = 0
INITIAL QUARTER-WAVE-PLATE ORIENTATION = 0
QMA SCALE = 0.1E-09 MBAR
ELECTROMETER FULL SCALE READING = 0.3E-07 A
DATA OPEN TIME = 1000 MS/READING = 3000 MS/LINE
DATA CLOSED TIME = 1000 MS/READING = 3000 MS/LINE
DELAY AFTER CHOPPER = 125 MS
TOTAL ION COUNT/ORIENTATION = 15000.
NUMBER OF CYCLES WITH LASER BLOCKED = 3

	------OPEN------			-----CLOSED-----			
CODE	ION	ELECTRON	QMA	ION	ELECTRON	QMA	LINE
3	1682	36936.	9767.	968	37075.	7202.	1
4	1688	37583.	46272.	973	37602.	26925.	2
3	1760	36760.	9307.	976	37000.	6994.	3
4	1610	36270.	45705.	874	36278.	26273.	4
3	1702	36256.	9162.	908	36348.	7081.	5
4	1637	35936.	45638.	920	36243.	26417.	6
196	1655	36566.	18262.	905	36789.	7198.	7
197	1697	36712.	56752.	956	36643.	26692.	8
196	1673	36961.	18089.	879	37017.	6955.	9
197	1767	36791.	56817.	930	36750.	26483.	10
196	1734	36894.	18093.	943	37007.	7059.	11
197	1579	36489.	56097.	921	36577.	26489.	12
196	1567	36417.	18436.	907	36408.	6823.	13
197	1676	36316.	55947.	989	36399.	26091.	14
196	1677	36387.	18189.	924	36576.	7155.	15
197	1639	35800.	56055.	851	35899.	25973.	16
196	1673	36418.	17895.	842	36402.	6802.	17
197	1703	36942.	55765.	952	36943.	26157.	18
196	1633	36417.	18271.	900	36550.	7296.	19
197	1736	37346.	56287.	913	37300.	26448.	20
196	1740	37445.	18069.	1053	37540.	7058.	21
197	1714	36871.	56032.	975	37136.	25641.	22
196	1703	37142.	18072.	942	37088.	7126.	23
197	1760	37566.	55770.	972	37524.	25859.	24
196	1786	38365.	17955.	966	38336.	6985.	25
197	1905	38883.	55850.	1028	38899.	25650.	26
3	1565	36377.	9539.	953	36613.	7227.	27
4	1663	36608.	45874.	929	36590.	26828.	28
3	1579	36260.	9553.	928	36568.	6977.	29
4	1673	36452.	45793.	953	36359.	26579.	30
3	1576	36890.	9413.	982	36858.	6723.	31
4	1683	36945.	45110.	951	37146.	25999.	32
198	1595	36794.	18583.	931	36894.	7408.	33
199	1612	36400.	56506.	947	36739.	26564.	34
198	1531	35379.	18142.	864	35526.	7067.	35

Text Box 4.3 Beginning of a typical printout of raw data above the ionization threshold for H_2.

Additional data must be acquired above the ionization threshold of H_2 in order to correct for ionization of molecular contamination in the beam and residual H_2 in the interaction chamber. The procedures for acquiring this data are described in the next two sections.

1. Determination of F_2

The determination of the fraction, F_2, of ion counts due to molecular contamination in the hydrogen beam [cf. (1.3)] requires data acquired with the hydrogen-source rf power off in addition to the primary data with the rf power on. Also, for both conditions of the rf power, data needs to be acquired with the QMA tuned to both 1 u/e and 2 u/e. The data acquisition procedure is otherwise the same as for the primary data, except that less data is acquired with the rf power off because its effect on the error in the asymmetry is less than that of the primary data.

2. Beam-loading correction

The hydrogen-beam chopper was toggled at a slow speed (toggling period = 2.33 s) due to the slow response time of the QMA at the pressure settings necessary to obtain precise measurements of the hydrogen-beam intensity. Unfortunately, this slow operation caused the residual-gas pressure in the interaction chamber to oscillate due to beam loading. This oscillation caused the background ion counts due to ionization of the residual gas to oscillate as well if the electron energy exceeded a certain threshold (see Figure 4.8). Notice

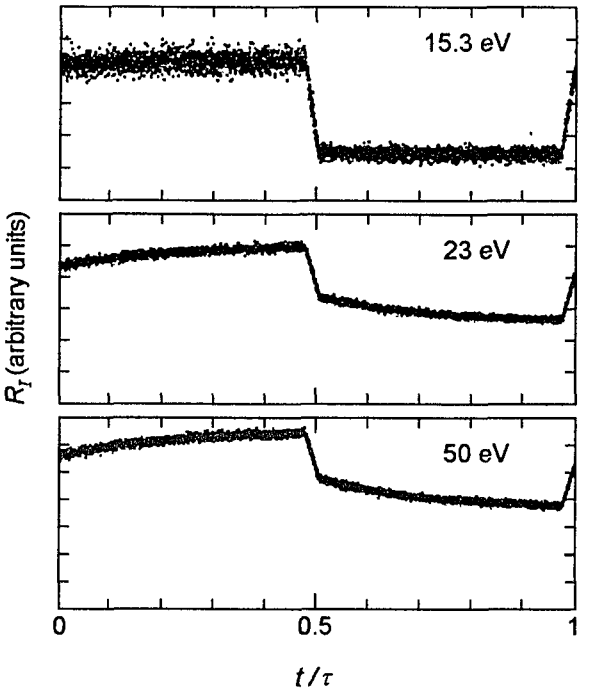

Figure 4.8 Plots of the ion rate, R_I, as a function of time, t, during one chopping period, τ = 2.33 s.

that the ion rate at 15.3 eV is constant while the chopper is either open or closed, while the corresponding rates at 23 eV and 50 eV exhibit significant drifts. This circumstance suggests that the changes in ion rates are due to the dumping and pumping of molecular hydrogen which has its ionization threshold at 15.43 eV, and that the atomic-hydrogen component of the residual-gas pressure changes negligibly due to beam chopping. This interpretation is reasonable because the focusing of the hydrogen beam by the hexapole magnet causes much of the beam to strike surfaces in the interaction chamber. The probability of recombination at these surfaces is very high because the surfaces are densely coated with hydrogen after prolonged exposure to the beam.

The data shown in Figure 4.8, as well as similar data at other energies, is acquired by routing the amplified and discriminated output of the CEM to a multichannel analyzer (MCA) (i.e., the MCA replaces the counter in Figure 3.18). The MCA is operated in a multiscaling mode with a dwell time of 0.5 ms per channel and an average delay between dwell times of 0.15 ms. A computer program executed on the LSI-11/23 microprocessor operated the hydrogen-beam chopper at the same rate as during acquisition of the primary data files, except that there were no interruptions for rotating the retardation plates and laser chopper or for translating the QMA. The polarization vectors of the incident and atomic electrons were antiparallel throughout the beam-loading data acquisition. Separate data files were acquired for each condition of the hydrogen-source rf (on or off) at each energy above the ionization threshold of H_2 at which primary data was acquired, as well as at 15.0 eV and 15.3 eV. Data acquisition typically continued for ~1 h for each file. The accumulated counts ranged from a few hundred per channel to a few thousand per channel, depending upon the magnitude of the ionization cross sections at the energy at which data is collected.

CHAPTER FIVE: DATA ANALYSIS

The procedures used for analyzing the acquired data are described in this chapter. The data-acquisition procedures are described in Chapter Four; the results of the analyses are presented and discussed in Chapter Six.

I. HYDROGEN BEAM

The procedures used for analyzing the data acquired for the determination of the following three parameters of the hydrogen beam at the interaction point are described in this section: the electron-spin polarization, the atomic density and the dissociation fraction. These procedures have already been described in Chan *et al* (1988); therefore, only a brief outline is given here.

A. Polarization

As a result of the coupling of nuclear and electronic spins at low magnetic-field intensities, the electron-spin polarization of the atomic-hydrogen beam depends upon the strength of the local magnetic field. The polarization of interest in the ionization-asymmetry measurement is the low-field (~100 mG) polarization at the interaction point. This polarization is determined by first determining the high-field limit of the net right-left asymmetry of the beam at the quadrupole-mass analyzer (QMA). Computer simulations are then

used to match this result and calculate the corresponding low-field polarization at the interaction region.

The raw data comprises the following set of beam profiles: a set of Q_1^{on} profiles with different driving currents, I_D, in the analyzing magnet; a Q_1^{off} profile; aQ_2^{on} profile and a Q_2^{off} profile, where the superscript indicates the state of the hydrogen-source rf power and the subscript indicates the mass tuning of the QMA. The Q_1^{on} profiles are the primary profiles; the other profiles are used to correct for background signal due to molecular hydrogen in the beam. The Q_1^{on} profiles contain contributions from the following three sources: (1) atomic hydrogen in the beam, (2) dissociative ionization of molecular hydrogen in the beam and (3) dissociative ionization of residual molecular hydrogen at the QMA. The signal of interest is due to atomic hydrogen, which is extracted by subtracting out the signals due to molecular hydrogen.

Figure 5.1 is a sketch of a typical profile indicating the relationship between several of the parameters used in the analysis. The net left-right asymmetry, Δ_H, is calculated about the centroid, x_c, of the undeflected atomic beam profile (Q_1^{on}, $I_D = 0$). The signal due to the beam is restricted to the region between x_L and x_R. The signal outside this region is entirely due to dissociative ionization of residual molecular hydrogen at the QMA, which also contributes to the signal where the beam is present. In order to calculate this latter contribution, the pedestal function, $y^P(x)$, is

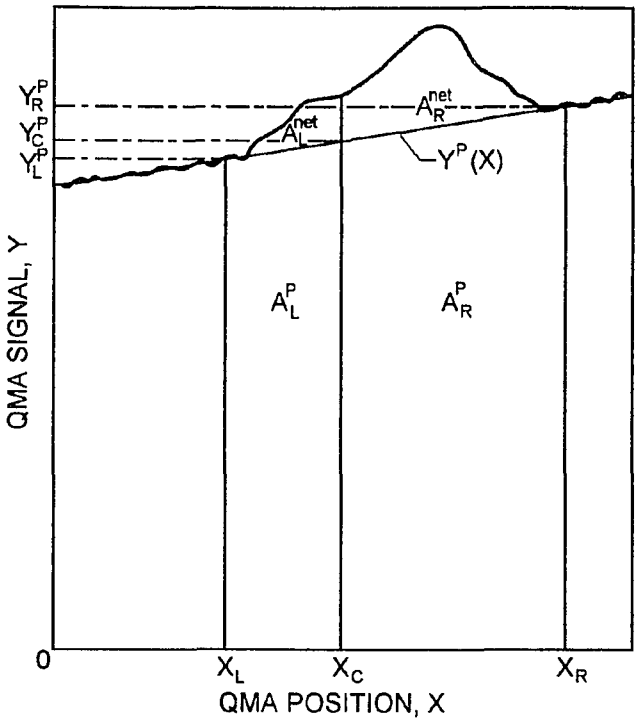

Figure 5.1 Graph showing the relationships between quantities used in the polarization analysis of the hydrogen beam profiles. The symbols are defined in the text.

determined by applying a linear least-squares fit to the signal in the outer region. The quantities y_L^P, y_C^P and y_R^P are the values of the pedestal function at x_L, x_C and x_R, respectively. The quantities A_L^{net} and A_R^{net} are the signals due to atomic hydrogen in the beam, which are the signals of primary interest. Not shown in the figure are the contributions A_L^D and A_R^D due to dissociative ionization of molecular hydrogen in the beam, where the former is in the region between x_L and x_C, and the latter is between x_C and x_R.

The analysis comprises five main stages: (1) calculation of the net signals for the Q_2^{on} and Q_2^{off} profiles, (2) calculation of the signals due to dissociative ionization of

molecular hydrogen in the beam, (3) determination of the centroid of the undeflected atomic-beam profile, (4) calculation of Δ_H at each setting of I_D, and (5) calculation of the low-field polarization in the interaction region.

Stage 1: Net Q_2^{on} and Q_2^{off} signals.

Step 1. Apply a linear least-squares fit to the outer regions of the profile to determine $y^P(x)$. The positions x_L and x_R are chosen based upon visual inspection of the profile. The results of the analysis are insensitive to the exact choice of values as long as they are in the linear regions and not too close to the extreme outer data points. The latter condition ensures that the uncertainty of the linear fit remains reasonably small.

Step 2. Calculate the total pedestal signal, A^P, as follows:

$$A^P = \frac{1}{2}(y_L^P + y_R^P)(x_R - x_L). \qquad (5.1)$$

Step 3. Calculate the total signal, A, as follows:

$$A = \left[\frac{1}{2}y(x_L) + \frac{1}{2}y(x_R) + \sum_{x=x_L+\Delta x}^{x_R-\Delta x} y(x)\right]\Delta x, \qquad (5.2)$$

where Δx = 0.125 mm is the distance between data points. For convenience, Δx is normalized to 1 for the purposes of the calculation, and all positions, x, are expressed as integral numbers of steps. The purpose of the one-half in the first two terms is to match the domain of the pedestal signal calculated in Step 2.

Step 4. Calculate the net signal, A^{net}, as follows:

$$A^{net} = A - A^{P}. \tag{5.3}$$

The net signal for the Q_2^{on} (Q_2^{off}) profile will be designated A_2^{on} (A_2^{off}).

Stage 2: Dissociative ionization of H_2 in beam.

Step 5. Determine $y^{P}(x)$ for the Q_1^{off} profile as in Step 1.

Step 6. Calculate the Q_1^{off} pedestal signals, A_L^P and A_R^P, as follows:

$$\begin{aligned} A_L^P &= \frac{1}{2}(y_L^P + y_C^P)(x_C - x_L) \\ A_R^P &= \frac{1}{2}(y_C^P + y_R^P)(x_R - x_C). \end{aligned} \tag{5.4}$$

Use x_0 (cf. Chapter Four, Section I.A) as the initial value for x_C. The final value of x_C is determined in Stage 3.

Step 7. Calculate the Q_1^{off} total signals, A_L and A_R, as follows:

$$\begin{aligned} A_L &= \left[\frac{1}{2}y(x_L) + \frac{1}{2}y(x_C) + \sum_{x=x_L+\Delta}^{x_C-\Delta} y(x)\right]\Delta x \\ A_R &= \left[\frac{1}{2}y(x_C) + \frac{1}{2}y(x_R) + \sum_{x=x_C+\Delta}^{x_R-\Delta} y(x)\right]\Delta x. \end{aligned} \tag{5.5}$$

Step 8. Calculate the Q_1^{off} net signals, A_L^{net} and A_R^{net}, as follows:

$$\begin{aligned} A_L^{net} &= A_L - A_L^P \\ A_R^{net} &= A_R - A_R^P. \end{aligned} \tag{5.6}$$

Step 9. Calculate the signals, A_L^D and A_R^D, due to dissociative ionization of molecular hydrogen in the beam as follows:

$$A_L^D = A_L^{net} \frac{A_2^{on}}{A_2^{off}}$$
$$A_R^D = A_R^{net} \frac{A_2^{on}}{A_2^{off}}. \qquad (5.7)$$

The physical significance of (5.7) is the following. The two contributions to the beam signal in Q_1^{on} profiles, the first due to atomic hydrogen and the second due to molecular hydrogen in the beam, cannot be separated by analyzing only Q_1^{on} profiles. However, when set to mass two, the QMA is insensitive to atoms. Also, when the rf power is off, there are no atoms to detect, even if the QMA is tuned to mass one. The signals A_L^{net} and A_R^{net} are due entirely to molecules (since the rf is off) with the QMA tuned to mass one. The signals A_2^{on} and A_2^{off} are also due entirely to molecules, since the QMA is tuned to mass two. Now the sensitivity of the QMA to molecules depends upon its mass tuning. The quantity of interest is the signal due to molecules with the rf on and the QMA tuned to mass one. The quotient in (5.7) is the ratio of the flux of molecules in the beam with the rf on to the flux with the rf off. The QMA measures the same flux ratio whether tuned to mass one or mass two. The quantities A_L^{net} and A_R^{net} measure the flux of

molecules with the rf off and the QMA tuned to mass one. By multiplying by the flux ratio, one obtains the desired quantity.

Stage 3: Determination of x_C.

Step 10. Determine $y^P(x)$ for the undeflected atomic beam (Q_1^{on}, $I_D = 0$) according to Step 1.

Step 11. Calculate the pedestal signals according to (5.4).

Step 12. Calculate the total signals according to (5.5).

Step 13. Calculate the Q_1^{on} net signals, A_L^{net} and A_R^{net}, as follows:

$$\begin{aligned} A_L^{net} &= A_L - A_L^P - A_L^D \\ A_R^{net} &= A_R - A_R^P - A_R^D . \end{aligned} \tag{5.8}$$

Step 14. Calculate the left-right asymmetry, Δ_H, as follows:

$$\Delta_H = \frac{A_R^{net} - A_L^{net}}{A_R^{net} + A_L^{net}} . \tag{5.9}$$

Step 15. Vary x_C in the direction that tends to reduce $|\Delta_H|$, and repeat Steps 6-9 and 11-14. Continue varying x_C until the minimum value of $|\Delta_H|$ is found. Use the value of x_C corresponding to this minimum value in all subsequent calculations.

Stage 4: Calculation of $\Delta_H(I_D)$.

Step 16. Repeat Steps 10-14 for the other Q_1^{on} profiles.

Stage 5: Low-field polarization.

Step 17. Perform a Monte-Carlo simulation of the atomic-hydrogen beam. This simulation is described in detail in Chan *et al* (1988).

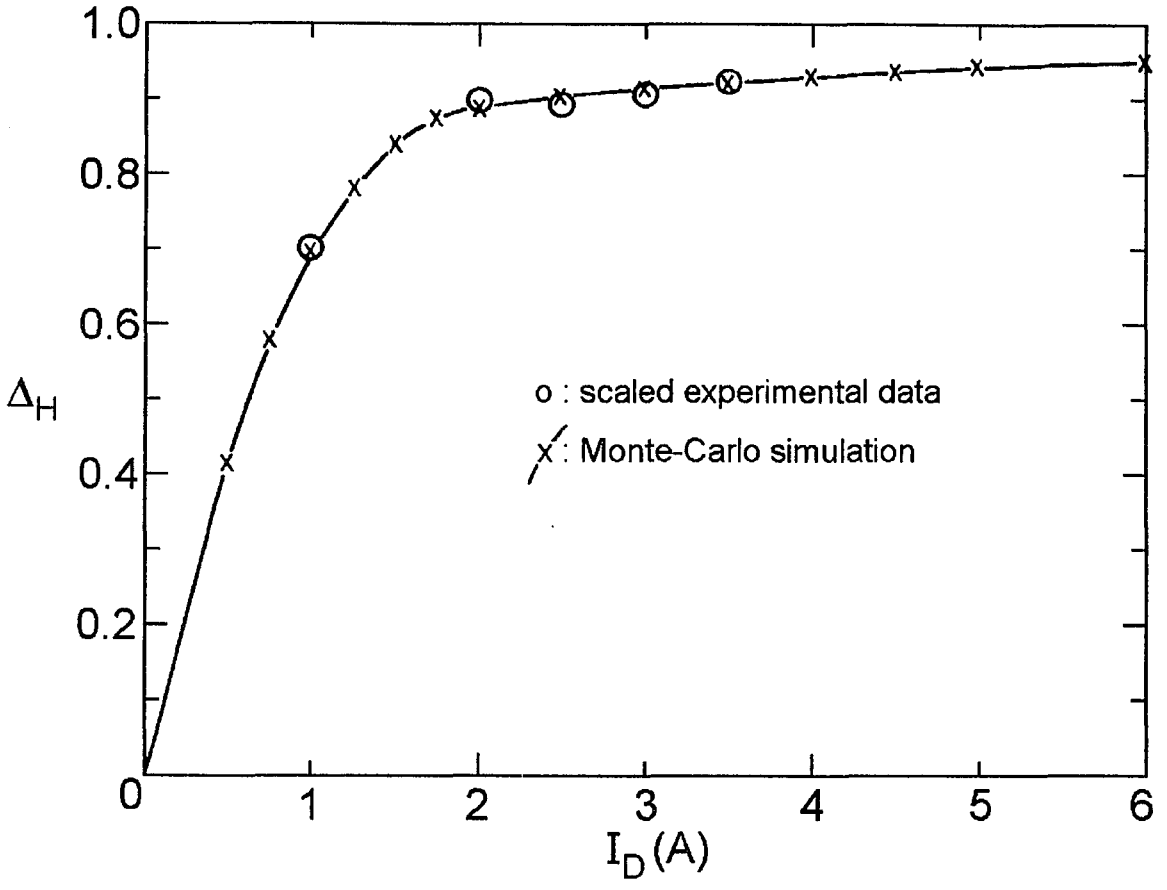

Figure 5.2 Plot of the left-right asymmetry, Δ_H, as a function of the driving current, I_D, in the analyzing magnet. The crosses are the results obtained by a Monte-Carlo simulation, with the solid line connecting them drawn to aid the eye. The experimental data points have been scaled as explained in the text.

Step 18. Compare the measured values of Δ_H with the results of the simulation. Figure 5.2 is a plot of both sets of values. The measured values have been uniformly scaled by a factor of 0.98 in order to match the simulation results. A slight misalignment of the hexapole and/or analyzing magnet could easily account for the scale factor (Chan *et al* 1988). With this one caveat, the agreement is outstanding.

Step 19. The Monte-Carlo simulation, having been validated by the measured asymmetry, is now used to calculate the low-field polarization of the atomic-hydrogen beam in the interaction region.

B. Density

Two separate determinations of the average density, $\overline{\rho}$, of the atomic-hydrogen beam in the interaction region are based upon measurements; a third determination is based purely upon a Monte-Carlo simulation (Chan *et al* 1988) of the hydrogen beam and will not be discussed here.

The raw data for the first determination are the pressures, p_H and p_0 in the interaction chamber with the hydrogen beam present and absent, respectively. The average density is then calculated from the relation (Chan *et al* 1988)

$$\overline{\rho} = \frac{2fS(p_H - p_0)}{\pi R_H^2 \overline{v} k T}, \qquad (5.10)$$

where f is the fraction of hydrogen atoms in the beam that reach the interaction region after entering the interaction chamber, S is the effective pumping speed in the interaction chamber, R_H is the radius of the hydrogen beam at the interaction region, $\overline{v}$ is the average velocity of a hydrogen atom at the interaction region, k is Boltzmann's constant and T is the absolute temperature of the gas. The 3-mm radius of the entrance aperture to the interaction region is used for R_H. The value of S is estimated to be ~530 l/s based upon the manufacturers specifications for the pumping speeds of the

various pumps in combination with calculated conductances between the pumps and the interaction chamber. The values of f and $\overline{v}$ are estimated by computer models of the beam (Chan *et al* 1988). Given the large uncertainties is some of the other values, T was simply estimated to be ~300 K.

The second determination of the density is based upon measurements of the angle-integrated ion production rate, R_I, due to electron-impact ionization at 15 eV. The average density is related to R_I by (Chan *et al* 1988)

$$\overline{\rho} = \frac{R_I}{\varepsilon \sigma_I j_e V}, \tag{5.11}$$

where ϵ is the efficiency for detecting ions, σ_I is the total ionization cross section, j_e is the electron current density, and V is the interaction volume given by

$$V = 8\int_0^{R_e} dz \int_0^{Y} dy \int_0^{X} dx, \tag{5.12}$$

where R_e is the radius of the electron beam at the interaction region, $X = \sqrt{R_e^2 - z^2}$, $Y = \sqrt{R_H^2 - R_e^2 + z^2}$, and the y (z) axis is the center of the electron (hydrogen) beam.

C. Dissociation Fraction

The raw data for the determination of the dissociation fraction, F_1, are a set of four QMA signals with the QMA tuned to 2 u/e: one with the hydrogen-source rf power on and the hydrogen-beam chopper open, one with the rf on and chopper closed, one with the rf power off and the chopper open, and

one with the rf power off and the chopper closed. The analysis proceeds as follows:

Step 1. Calulate the net QMA signals, Q_2^{on} and Q_2^{off}, with the rf on and off, respectively, by subtracting the chopper-closed signal from the chopper-open signal.

Step 2. Calculate F_1 as follows (Chan *et al* 1988):

$$F_1 = \frac{2\,(Q_2^{off} - Q_2^{on})}{2\,Q_2^{off} - Q_2^{on}} . \qquad (5.13)$$

II. ELECTRON BEAM

The procedures used to analyze the data acquired for the determination of the mean energy, standard deviation in energy, and polarization of the electron beam are described in this section.

A. Mean Energy

The mean energy, $\overline{E}_e$, of the electron beam is related to the voltage, V_c, applied to the GaAs crystal as follows:

$$\overline{E}_e = eV_c - \overline{E}_{offset} , \qquad (5.14)$$

where e is the elementary charge, and $\overline{E}_{offset}$ is an energy offset which results from contact potentials and the electron affinity of the GaAs crystal (Guo *et al* 1990a). The quantity $\overline{E}_{offset}$ is independent of V_c but varies with time. The voltage V_c is measured directly; $\overline{E}_{offset}$ is determined by measuring the

ionization cross section of molecular hydrogen, $\sigma_I^{H_2}$, near its ionization threshold, as noted previously.

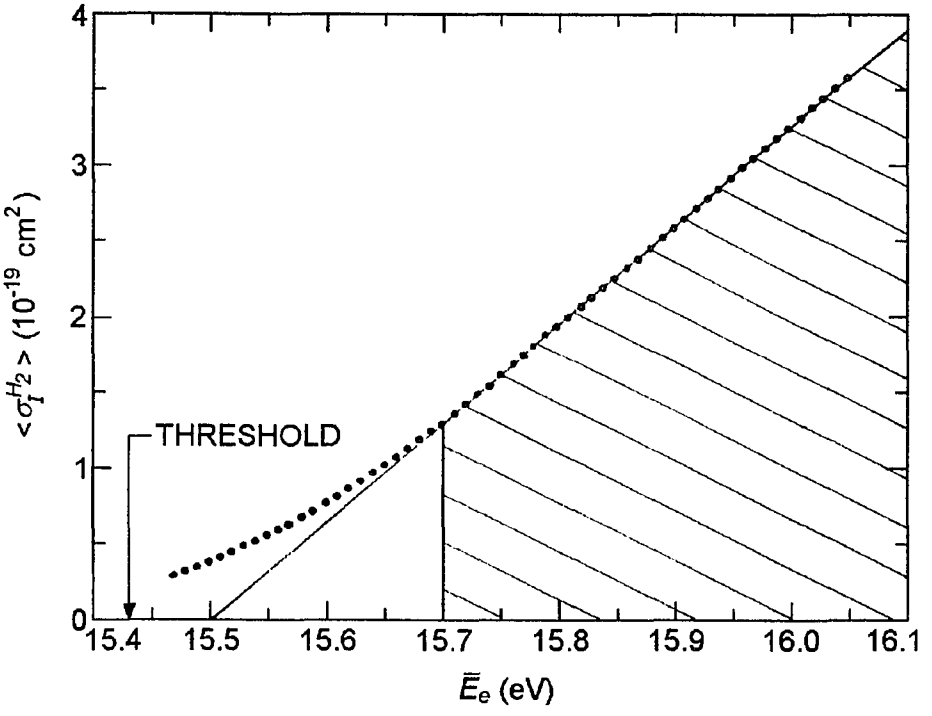

Figure 5.3 Plot of the convoluted molecular-hydrogen ionization cross section, $<\sigma_I^{H_2}>$, near threshold. The ionization data, taken from McGowan *et al* (1968), is convoluted with the Gaussian energy spread of σ_E = 75 meV typical of the electron beam. The convoluted cross section is linear above 15.7 eV. The extrapolation of the line intercepts the energy axis at 15.50 eV. The spectroscopic threshold at 15.43 eV is indicated by the arrow.

Figure 5.3 shows $<\sigma_I^{H_2}>$ in the near-threshold region, where <> indicates convolution, as described presently. The values of $\sigma_I^{H_2}$ are taken from McGowan *et al* (1968). The energy distribution of their (unpolarized) electron beam is very nearly Gaussian with an energy width $\lesssim$ 60 meV FWHM; as described in the next section, the energy distribution of our

(polarized) electron beam, although not Gaussian, is reasonably well characterized by a Gaussian width of ~180 meV FWHM. In order to compare our measurements with theirs, their results are convoluted with the Gaussian distribution that approximates the energy distribution of our beam. Since the energy width of our beam is much greater than theirs, the convolution assumes that their beam is monochromatic in order to simplify the calculation. The important features to note in the figure are (1) that the convoluted cross section is very well approximated by a straight line at energies between 15.70 and 16.05 eV, and (2) that the extrapolation of this line intercepts the energy axis at 15.500(10) eV. It should be noted that any data within 0.2 eV of the intercept should not be included in the linear fit used to determine the intercept.

The raw data comprise ion counts and measurements of the electron current and QMA mass-two signal at 0.1 V intervals in the range $18.3 < V_c < 19.0$ V. The measurements are made with the hydrogen-beam chopper alternately open and closed. When the chopper is closed, the ion signal is due to residual gases in the interaction chamber, and the QMA signal is due to residual gases in the beam dump; when the chopper is open, the signals due to molecular hydrogen in the beam are superposed on these backgrounds. The electron current is unaffected by the hydrogen-beam chopper.

The analysis proceeds as follows:

Step 1. Reject noisy data. A datum is rejected if it is more than 2.5 standard deviations from the mean.

Step 2. Sum data at each bias. The following five sums are generated at each bias: (1) ion counts with chopper open, (2) ion counts with chopper closed, (3) QMA signal with chopper open, (4) QMA signal with chopper closed, and (5) total electron current counts, I_e^{total}. The standard deviation in each of these quantities is calculated assuming Poisson (counting) statistics. This error is then propagated assuming stochastic independence between variables.

Step 3. Calculate the net ion counts, N_I^{net} (the counts due to ionization of molecular hydrogen in the beam), at each bias by subtracting the chopper-closed counts from the chopper-open counts. Similarly, calculate the net QMA signal, Q_2^{net} (the signal due to molecular hydrogen in the beam), at each bias by subtracting the chopper-closed signal from the chopper-open signal.

Step 4. Calculate $\sigma_I^{H_2}$ at each bias as follows:

$$\sigma_I^{H_2} = \frac{N_I^{net}}{I_e^{total} Q_2^{net}} . \qquad (5.15)$$

Although the acquisition time for I_e^{total} is twice that of either N_I^{net} or Q_2^{net}, this difference only contributes an extra factor of two to the scale factor of the relative cross section at each bias.

Step 5. Plot $\sigma_I^{H_2}$ as a function of V_c and perform a weighted linear least-squares fit, including the calculation of the V_c intercept, V_{int}, and its error. Figure 5.4 is a typical plot of this step.

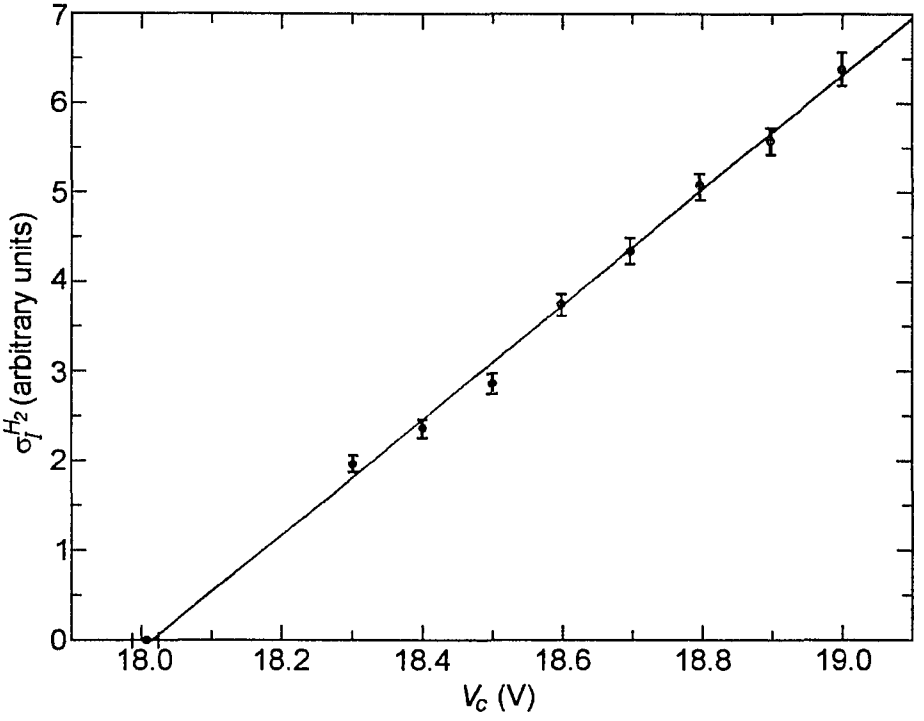

Figure 5.4 Graph of the molecular-hydrogen ionization cross section, $\sigma_I^{H_2}$, as a function of crystal voltage, V_c. Also shown is the linear least-squares fit, including its V_c intercept, V_{int}, which equals 18.0 V in this case, corresponding to $\overline{E}_{offset}$ = 2.5 eV.

Step 6. Calculate $\overline{E}_{offset} = eV_{int} - 15.50\ eV$ (cf. Figure 5.3).

The quantity $\overline{E}_{offset}$ was found to decrease with time after each reactivation (see Figure 5.5) due to a secular decrease in the negative electron affinity of the surface (Guo *et al* 1990a). The crystal surface was reactivated shortly after the last measurement shown in the figure.

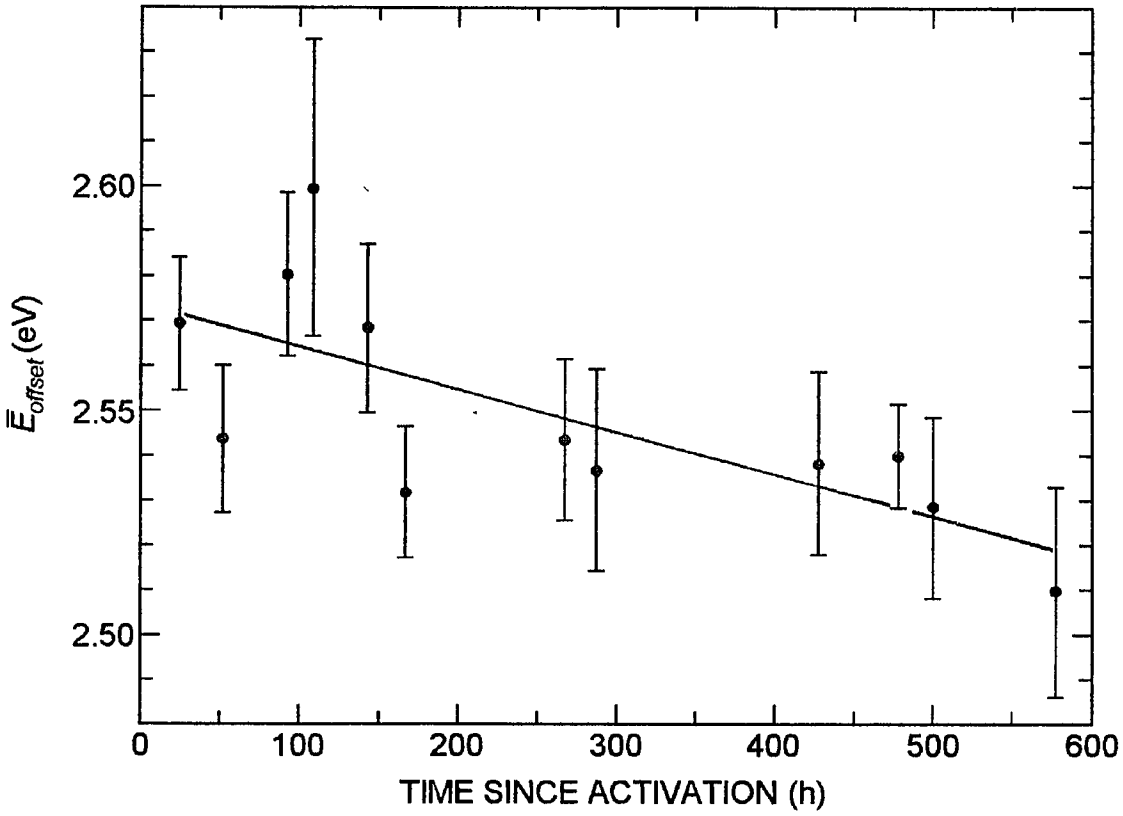

Figure 5.5 Graph showing time dependence of $\overline{E}_{offset} \equiv eV_c - \overline{E}_e$. Each data point is derived according to the procedure outlined in Figure 5.4. The error bars represent one standard deviation due to counting statistics. The line is the linear least-squares fit to the data.

B. Standard Deviation in Energy

The raw data for the determination of the standard deviation, σ_E, in the energy of the electron beam is similar to that for the determination of $\overline{E}_{offset}$ except that the hydrogen-source rf power is on and the QMA is tuned to mass one. The first four steps of the analysis are also the same with the following exceptions: in Step 3, N_I^{net} is due to ionization of atomic hydrogen in the beam, and the net QMA

signal is Q_1^{net} which is the signal due to atomic hydrogen in the beam; in Step 4, the atomic-hydrogen ionization cross section, $\sigma_I^{H_1}$, is calculated as follows:

$$\sigma_I^{H_1} = \frac{N_I^{net}}{I_e^{total} Q_1^{net}} . \qquad (5.16)$$

The analysis then continues as follows:

Step 5. Calculate theoretical curves of $\langle \sigma_I^{H_1} \rangle$, where $\langle\rangle$ again denotes convolution, as a function of $E - E_{th}$, where E is the energy of the electron beam and E_{th} = 13.605 eV is the ionization threshold of atomic hydrogen. These curves are generated by convoluting Wannier's (1953) theoretical prediction, $\sigma_I^{H_1} \propto (E - E_{th})^{1.127}$, with Gaussian distributions with various standard deviations. McGowan and Clarke (1968) demonstrated the validity of this form of Wannier's law in the regime in question: $0 \leq (E - E_{th}) \leq 300$ meV.

Step 6. Plot the experimental values of $\sigma_I^{H_1}$ and the theoretical curves as functions of $E - E_{th}$ on the same graph (see Figure 5.6). In order to compare these functions, they must all be normalized at the same value of E. This value has been chosen arbitrarily to be $E - E_{th}$ = 0.2 eV.

Step 7. Visually determine which theoretical curve best fits the data. Since the energy distribution of the electron beam differs significantly from a Gaussian, more sophisticated fitting techniques are not warranted.

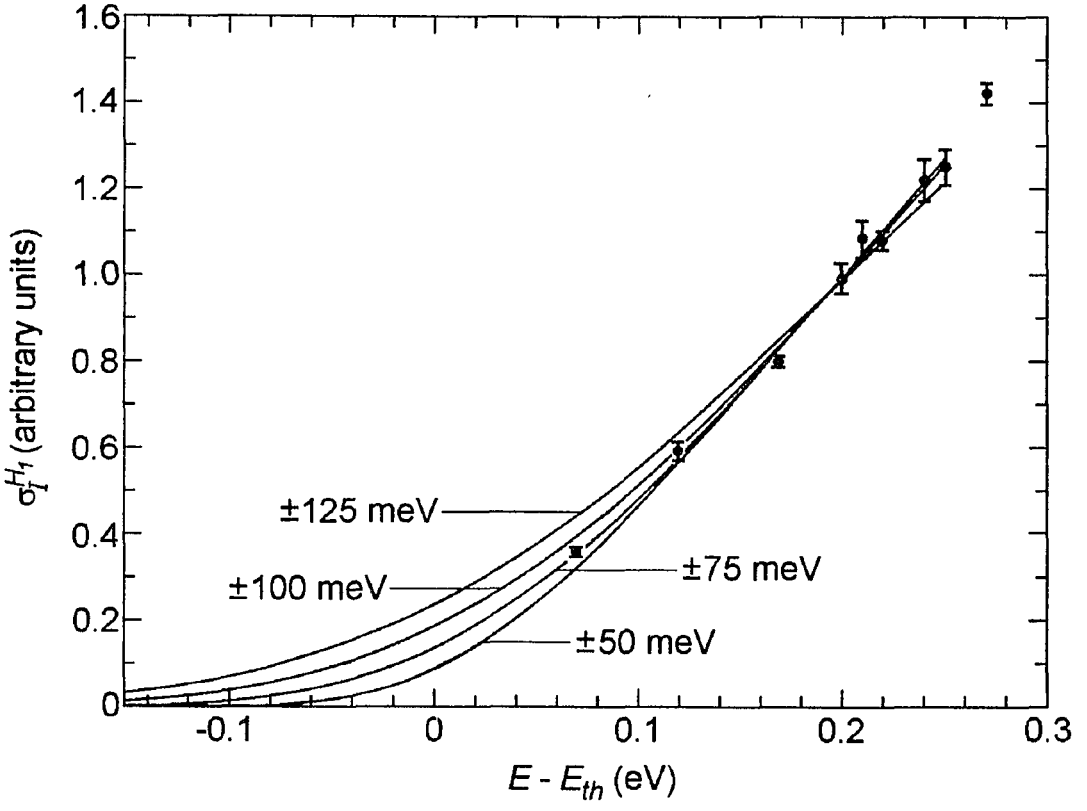

Figure 5.6 Graph of the ionization cross section, $\sigma_I^{H_1}$, of atomic hydrogen near its ionization threshold, E_{th}. The curves are derived from the Wannier (1953) cross-section laws convoluted with Gaussian distributions with the indicated standard deviations. All curves are normalized at $E - E_{th} = 0.2$ eV.

C. Polarization

The apparatus does not include an on-line electron polarimeter. The polarization, P_e, of the electron beam is determined by normalizing the ionization-rate asymmetries, Δ_I, of the present experiment to the absolute asymmetries, A_I, measured previously by Fletcher *et al* (1985). The polarization of the electron beam in the earlier experiment

was determined by Mott polarimetry. These asymmetries are related by (1.3), which when solved for A_I yields

$$A_I = \frac{\Delta_I}{P_e \cdot P_H \cdot |\cos\alpha| \cdot (1 - F_2)} = \frac{\Delta_I^{H_1}}{P_e \cdot P_H \cdot |\cos\alpha|}, \qquad (5.17)$$

where it is convenient to define the atomic-hydrogen ionization- rate asymmetry, $\Delta_I^{H_1}$, as

$$\Delta_I^{H_1} \equiv \frac{\Delta_I}{1 - F_2} \qquad (5.18)$$

since the latter denominator of (5.17) is independent of energy. The procedure for determining $\Delta_I^{H_1}$ is described in Section III; the procedure for determining P_H is described in Section I.A; $|\cos\alpha|$ was determined by magnetic-field measurements to be 0.99(1).

The energy spread of the electron beam in the previous experiment was more than an order of magnitude greater than that in the present experiment; therefore, the results of the present experiment must be convoluted with the energy spread of the previous experiment before the results of the two experiments can be compared. This convolution is effected by first fitting a functional form to $\Delta_I^{H_1}$ (see Figure 5.7). The convoluted curve is scaled according to (5.17) with various values of P_e and plotted on the same graph as the results of the previous experiment. A visual determination is then made as to which value of P_e results in the best fit (see Figure 5.8). A more rigorous fitting technique is unwarranted

due to the approximations made in fitting the functional form to $\Delta_I^{H_1}$.

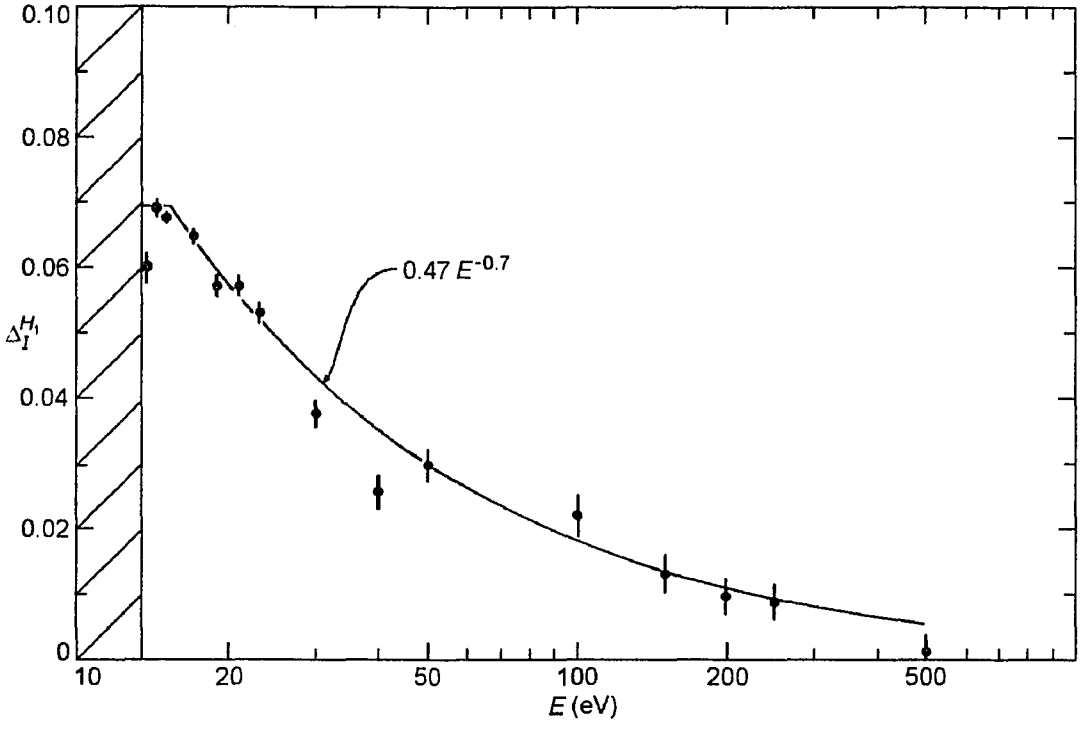

Figure 5.7 Graph of the atomic-hydrogen ionization asymmetry, $\Delta_I^{H_1}$, as a function of the incident electron energy, E. The error bars represent one standard deviation due to counting statistics. The curve is the least-squares fit of the data above 15.1 eV to a power law. The anomalous points at 30 eV and 40 eV are not included in the least-squares fit. Below 15.1 eV, the curve has a constant value of 0.07.

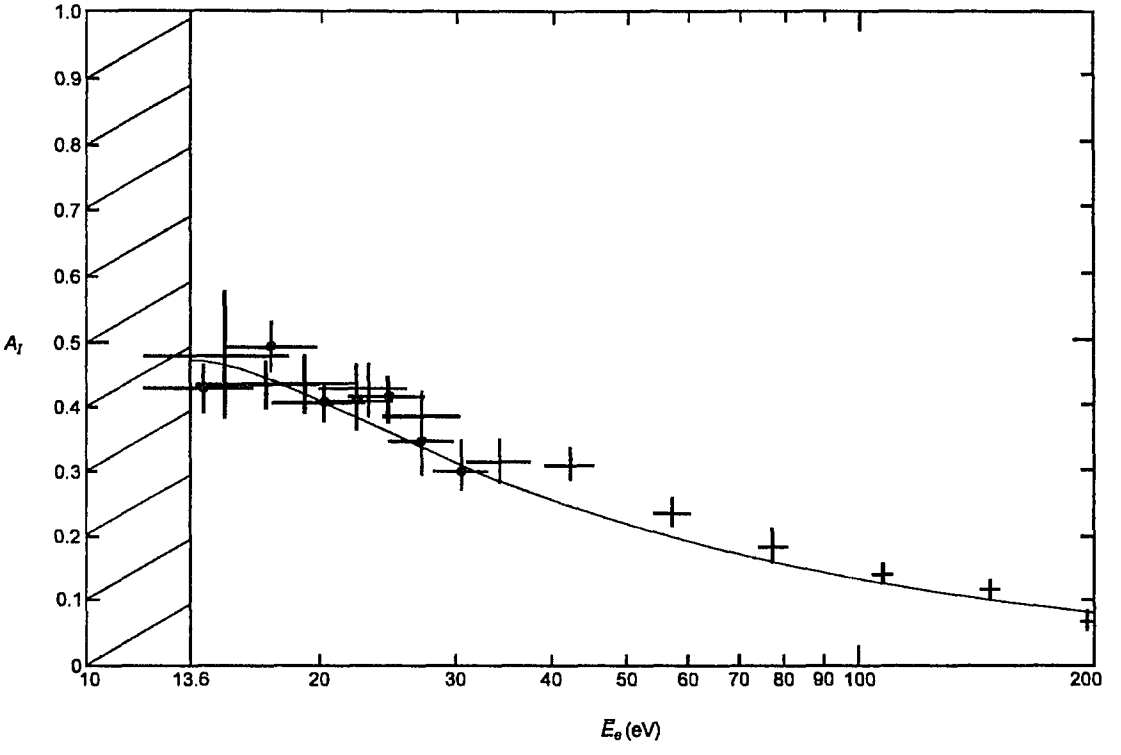

Figure 5.8 Comparison plot of the A_1 data of Fletcher *et al* (1985) and the convoluted functional fit to the present data for an assumed P_e = 0.27.

III. IONIZATION ASYMMETRY

Two slightly different procedures are used to analyze the data acquired for the determination of the ionization asymmetry: a simpler procedure below the H_2 ionization threshold and a more complicated one above the H_2 ionization threshold. The simpler procedure, which is a subset of the more complicated procedure, is described first. The analysis is outlined up to the calculation of $\Delta_I^{H_1}$ [cf. (5.18)], only. The last step of the analysis is described in Section II.C.

A. Near Threshold

The raw data for the determination of the ionization asymmetry in the near threshold region are contained in a set of data files (cf. Text Box 4.2). Each data file contains data obtained at a single electron energy. The basic data types are ion counts, N_I, electron-current counts, I_e, and QMA mass-one-signal counts, Q_1. These counts are recorded in six columns in the data files with two columns for each data type: one with the hydrogen-beam chopper open and one with the chopper closed. A seventh column records a code which indicates, among other things, the orientations of the retardation plates and the position of the laser chopper. In the following, superscripts indicate the position of the hydrogen-beam chopper. In addition, the lower-case symbols, n_I, i_e and q_1, represent ion, electron and QMA counts, respectively, during laser-blocked-code data acquisition (LBCDA).

The measured signals comprise the following contributions:

$$
\begin{aligned}
N_I^{open} &= N_{H^+} + N_R + N_{\gamma_H} + N_{\gamma_S} + N_P + N_D + G \\
N_I^{closed} &= N_R + N_P + N_D + G \\
n_I^{open} &= (N_{H^+} + N_R + N_{\gamma_H}) + N_{\gamma_S} + N_P + N_D + G \\
n_I^{closed} &= (N_R) + N_P + N_D + G \qquad (5.19) \\
I_e^{open} = I_e^{closed} &= I_e + I_B + G \\
i_e^{open} = i_e^{closed} &= (I_e) + I_B + G \\
Q_1^{open} &= Q_B + Q_R + G \\
Q_1^{closed} = q_1^{open} = q_1^{closed} &= Q_R + G,
\end{aligned}
$$

where the symbols on the right-hand side have the following meanings:

N_{H^+} Ion counts due to ionization of H atoms by e^- beam.

N_R Ion counts due to ionization of residual gas by e^- beam.

N_{γ_H} Ion counts due to photons from atoms excited by e^- beam.

N_{γ_S} Ion counts due to photons generated in hydrogen source.

N_P Ions due to ionization of residual gas by ion pumps.

N_D Ion counts due to dark current in the CEM.

I_e Electron counts due to electron beam.

I_B Electron counts due to improper zeroing of electrometer.

Q_B QMA counts due to hydrogen beam.

Q_R QMA counts due to residual gas.

G Spurious counts due to gating blind counters (1/reading).

The parenthetical terms in (5.19) are included if the laser is never blocked.

The analysis proceeds as follows:

Step 1. Reject noisy data. A datum is rejected if it is more than 2.5 standard deviations from the local mean value for its data type. Six plots are generated from each data file: one for each column. Figure 5.9 is an example of one of these plots. The plots are inspected visually to identify suspected noisy points. The numerical values are then read from a printout of the data file, and standard deviations are calculated assuming Poisson (counting) statistics. If any of the six data types on a line is noisy, the entire line is deleted from the data file before continuing with the analysis. (A copy of the unedited data file is maintained separately.)

Step 2. Sum data for each combination of retardation-plate orientations and laser-chopper position. The following seven sums are generated for each of the thirty-three LBCDA combinations: n_I^{open}, n_I^{closed}, i_e^{open}, i_e^{closed}, q_1^{open}, q_1^{closed} and n, where n is the number of lines of data for that combination. The following seven sums are generated for each of the thirty-two non-LBCDA combinations: N_I^{open}, N_I^{closed}, I_e^{open}, I_e^{closed}, Q_1^{open}, Q_1^{closed} and N, where N is the number of lines of data for that combination. Errors are calculated assuming Poisson (counting) statistics and propagated assuming stochastic independence between variables.

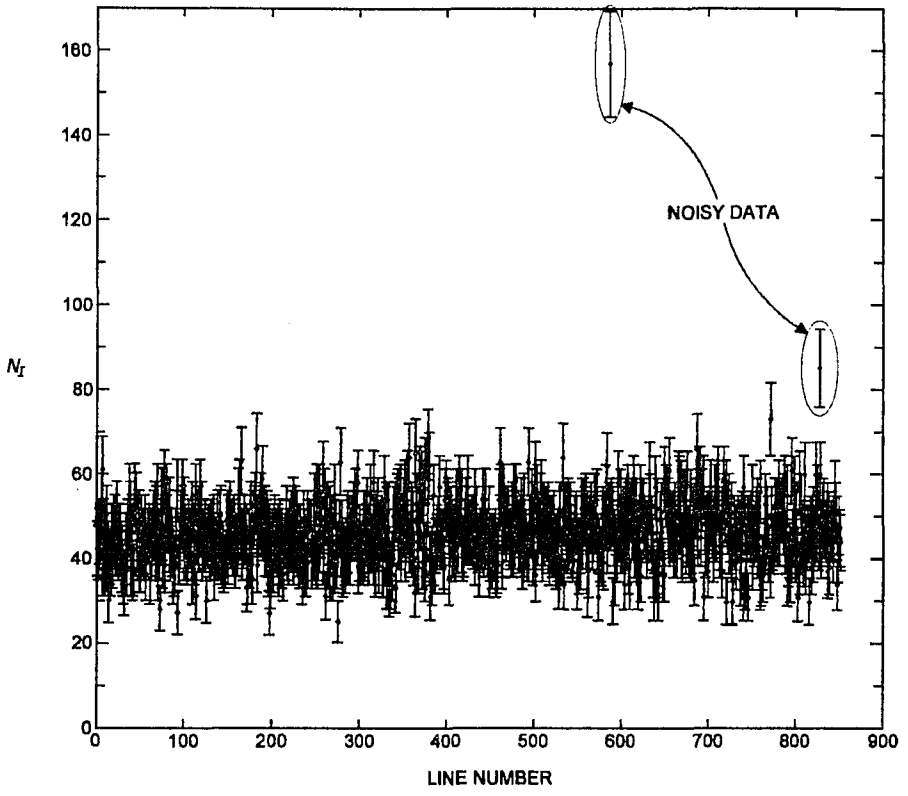

Figure 5.9 An example of a plot of N_I^{closed} data showing noisy data. This plot is for a data run at 13.67 eV.

Step 3. If the laser was blocked, correct ion and electron counts for background signals during LBCDA as follows:

$$
\begin{aligned}
(N_I^{open})^{net} &= N_I^{open} - \frac{N}{2}\left[\left(\frac{n_I^{open}}{n}\right)_- + \left(\frac{n_I^{open}}{n}\right)_+\right] \\
(N_I^{closed})^{net} &= N_I^{closed} - \frac{N}{2}\left[\left(\frac{n_I^{closed}}{n}\right)_- + \left(\frac{n_I^{closed}}{n}\right)_+\right] \\
(I_e^{open})^{net} &= I_e^{open} - \frac{N}{2}\left[\left(\frac{i_e^{open}}{n}\right)_- + \left(\frac{i_e^{open}}{n}\right)_+\right] \\
(I_e^{closed})^{net} &= I_e^{closed} - \frac{N}{2}\left[\left(\frac{i_e^{closed}}{n}\right)_- + \left(\frac{i_e^{closed}}{n}\right)_+\right],
\end{aligned}
\qquad (5.20)
$$

where the subscript - (+) indicates the LBCDA data acquired immediately preceding (following) the

acquisition of the non-LBCDA data. If $n = 0$ for one of the LBCDA combinations, its term is eliminated and the factor of ½ is dropped. If the laser was not blocked, add the LBCDA ion and electron counts to the non-LBCDA counts as follows:

$$\begin{aligned} (N_I^{open})^{net} &= N_I^{open} + (n_I^{open})_- \\ (N_I^{closed})^{net} &= N_I^{closed} + (n_I^{closed})_- \\ (I_e^{open})^{net} &= I_e^{open} + (i_e^{open})_- \\ (I_e^{closed})^{net} &= I_e^{closed} + (i_e^{closed})_- . \end{aligned} \tag{5.21}$$

Remember that the retardation plates are rotated before each LBCDA.

Step 4. Correct the Q_1^{closed} signal for beam loading as follows:

$$(Q_1^{closed})' = Q_1^{closed} \frac{(q_1^{open})_- + (q_1^{open})_+}{(q_1^{closed})_- + (q_1^{closed})_+} . \tag{5.22}$$

When the hydrogen-beam chopper is open (closed), the residual pressure downstream increases (decreases). Therefore the QMA signal acquired with the chopper closed is not the QMA signal due to residual pressure while the chopper is open. This difference is corrected by translating the QMA off to the side of the hydrogen beam during LBCDA. Thus, the signal during LBCDA is due to residual pressure for both chopper positions. The correction in (5.22) assumes that the ratio of residual pressures is the same at the center of the beam as it is off to the side of the beam. This assumption is reasonable considering that

when the chopper is closed, the QMA signal is practically the same in both positions (cf. Text Box 4.2).

Step 5. Calculate the net QMA signal for each code as follows:

$$Q_1^{net} = C_Q\left[\frac{Q_1^{open}}{NT_O} - \frac{(Q_1^{closed})'}{NT_C}\right], \qquad (5.23)$$

where C_Q is a factor that converts QMA counts into mbar and T_O (T_C) is the data-acquisition time with the hydrogen-beam chopper open (closed).

Step 6. Calculate the (relative) angle-integrated ionization cross section for each code as follows:

$$\sigma_I^{H_1} = \frac{1}{C_e Q_1^{net}}\left[\frac{(N_I^{open})^{net}}{(I_e^{open})^{net}} - \frac{(N_I^{closed})^{net}}{(I_e^{closed})^{net}}\right], \qquad (5.24)$$

where C_e is a factor that converts electron-current counts into number of electrons.

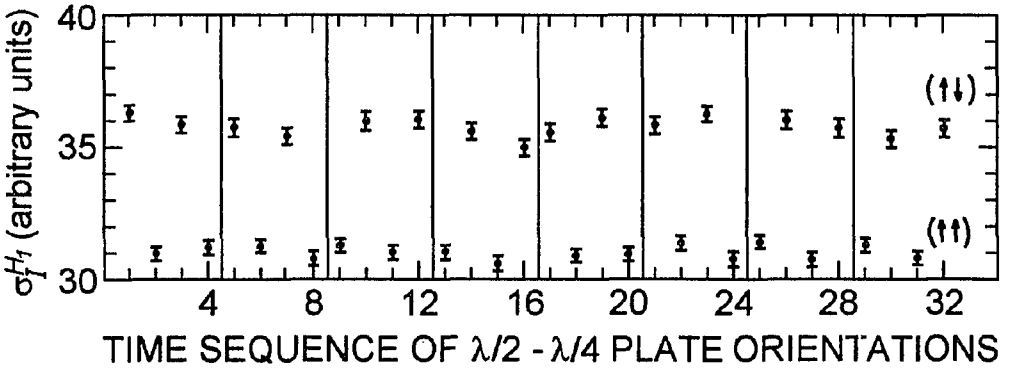

Figure 5.10 The atomic-hydrogen ionization cross section, $\sigma_I^{H_1}$, as a function of the time sequence of retardation-plate orientations from a data run at 14.82 eV. Note the obvious difference between the cross sections with spins parallel and antiparallel.

Step 7. Divide the complete set of thirty-two cross sections into eight subsets of four cross sections each (cf. Figure 5.10). Two of these four cross sections, hereafter designated $\sigma_1(\uparrow\downarrow)$ and $\sigma_2(\uparrow\downarrow)$, are for electron and atom spins antiparallel; the other two cross sections, $\sigma_1(\uparrow\uparrow)$ and $\sigma_2(\uparrow\uparrow)$, are for electron and atom spins parallel. Calculate $\Delta_I^{H_1}$ for each subset as follows:

$$\Delta_I^{H_1} = \frac{\sigma(\uparrow\downarrow) - \sigma(\uparrow\uparrow)}{\sigma(\uparrow\downarrow) + \sigma(\uparrow\uparrow)}, \qquad (5.25)$$

where $\sigma(\uparrow\downarrow)$ $[\sigma(\uparrow\uparrow)]$ is the weighted mean of $\sigma_1(\uparrow\downarrow)$ and $\sigma_2(\uparrow\downarrow)$ $[\sigma_1(\uparrow\uparrow)$ and $\sigma_2(\uparrow\uparrow)]$.

Step 8. In order to assess systematic errors, calculate two false asymmetries, Δ_{F+} and Δ_{F-}, for each subset as follows:

$$\Delta_{F\pm} = \frac{[\sigma_1(\uparrow\downarrow) - \sigma_2(\uparrow\downarrow)] \pm [\sigma_1(\uparrow\uparrow) - \sigma_2(\uparrow\uparrow)]}{\sigma_1(\uparrow\downarrow) + \sigma_2(\uparrow\downarrow) + \sigma_1(\uparrow\uparrow) + \sigma_2(\uparrow\uparrow)}. \qquad (5.26)$$

In the absence of systematic errors, both false asymmetries should be zero. If either false asymmetry differs from zero by more than 2.5 standard deviations, reject all data for that subset.

Step 9. Calculate the weighted mean of the values of $\Delta_I^{H_1}$ for the remaining subsets. Also calculate the reduced chi-squared about the mean. If any value is more than 2.5 standard deviations from the mean, that value is rejected and the mean and reduced chi-squared are recalculated.

Step 10. Calculate the reduced chi-squared about zero of the false asymmetries for the remaining subsets.

Step 11. After all the data files have been analyzed, calculate at each energy, E, the weighted mean, $\overline{\Delta}_I^{H_1}(E)$, of the values of $\Delta_I^{H_1}$ for that energy. Also calculate the reduced chi-squared about the mean.

Step 12. Calculate the reduced chi-squared about zero for each of the sixteen false asymmetries using all data files at all energies, including the higher energies discussed in the next section.

Step 13. Plot a histogram of the normalized real-asymmetry residuals, x_R, given by

$$x_R \equiv \frac{\Delta_I^{H_1}(E) - \overline{\Delta}_I^{H_1}(E)}{\sigma_{\Delta_I^{H_1}(E)}}, \qquad (5.27)$$

where $\sigma_{\Delta_I^{H_1}(E)}$ is the standard deviation of $\Delta_I^{H_1}(E)$. Include all data runs at all energies, including the higher energies discussed in the next section.

Step 14. Plot histograms of the normalized false asymmetries, $x_{F\pm}$, given by

$$x_{F\pm} \equiv \frac{\Delta_{F\pm}}{\sigma_{\Delta_{F\pm}}}, \qquad (5.28)$$

where $\sigma_{\Delta_{F\pm}}$ is the standard deviation of $\Delta_{F\pm}$. Include all data runs at all all energies, including the higher energies discussed in the next section.

B. Above H_2 Ionization Threshold

The primary data files for energies above the ionization threshold of molecular hydrogen (15.43 eV) are the same as the data files for lower energies except that the QMA tuning alternates between mass one and mass two from one line to the next. The analysis of these data files proceeds as outlined in the previous section with the following exceptions. In Step 1, the mass-one and mass-two data are plotted separately, resulting in a total of eight plots. In Step 2, four new sums, q_2^{open}, q_2^{closed}, Q_2^{open} and Q_2^{closed}, are generated for mass-two data for a total of nine sums for each combination. Note that the ion and electron counts, as well as the number of lines, are summed over both QMA settings. In Step 4, Q_2^{closed} is also corrected for beam loading according to (5.22) with all subscripts changed from 1 to 2. In Step 5, the net mass-two signal is also calculated according to (5.23) with all subscripts changed from 1 to 2. And in Steps 6, 7, 9, 11 and 13, drop the superscript "H_1", since some of the ions are now due to electron-impact ionization of molecular hydrogen. In addition, the quantity Λ^{on} is calculated, as described in the next section.

Additional data is acquired at energies above the ionization threshold of H_2 in order to correct for ionization of molecular contamination in the beam and residual H_2 in the interaction chamber. The procedures for analyzing this data are described in the next two sections.

1. Determination of F_2

The raw data for the determination of the fraction, F_2, of ions due to molecular contamination in the hydrogen beam is contained in the primary data files (with the additional mass-two readings) and in similar data files acquired with the hydrogen-source rf power off. Both sets of data files are analyzed as outlined in the previous section. In particular, the quantities $(N_I^{open})^{net}$, $(N_I^{closed})^{net}$, $(I_e^{open})^{net}$, $(I_e^{closed})^{net}$ and Q_2^{net} are calculated. The analysis then continues as follows:

Step 15. Calculate the quantity $\Lambda(E)$ given by

$$\Lambda(E) \equiv \frac{1}{C_e Q_2^{net}} \left[\frac{(N_I^{open})^{net}}{(I_e^{open})^{net}} - \frac{(N_I^{closed})^{net}}{(I_e^{closed})^{net}} \right], \quad (5.29)$$

where E is the electron energy for the data file being analyzed. The quantity for data files with the rf on [off] is labelled $\Lambda^{on}(E)$ [$\Lambda^{off}(E)$].

Step 16. Calculate F_2 as follows (Fletcher *et al* 1985):

$$F_2(E) = \frac{\Lambda^{off}(E)}{\Lambda^{on}(E)}. \quad (5.30)$$

The quantity F_2 is calculated separately for each primary (rf-on) data file. Generally, only one rf-off data file was acquired per day at each electron energy for which rf-on data files were also acquired that day.

2. Beam-loading correction

The raw data for the beam-loading correction are contained in a set of data files, each of which was acquired at a single energy and rf condition (on or off). The data

files record the ion production rate, R_I, as a function of time, t. Figure 5.11 is a sketch of a typical data set showing some of the key parameters for the analysis of the data.

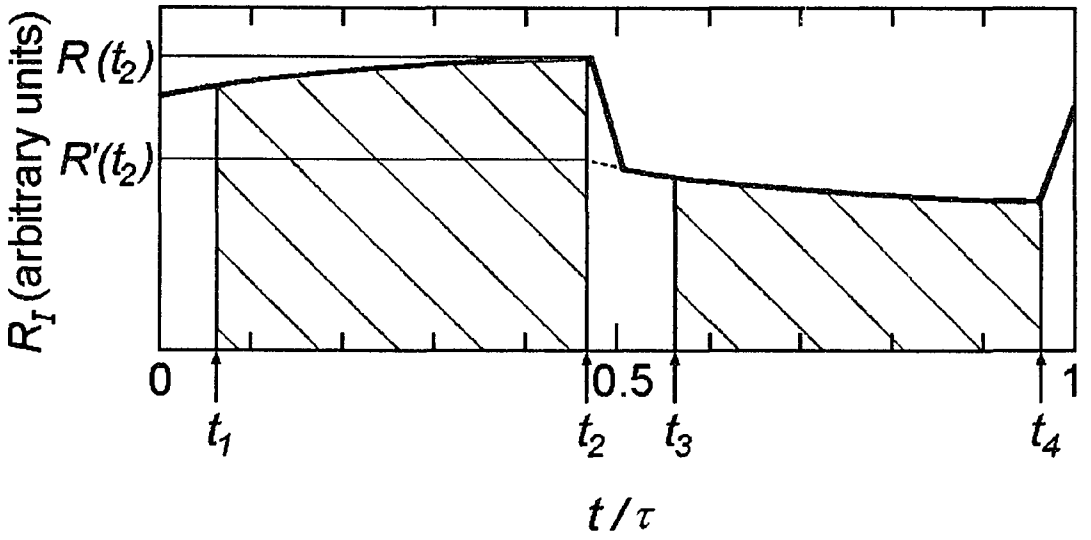

Figure 5.11 Graph showing important parameters for the analysis of the ion production rate, R_I, as a function of time, t, during one hydrogen-beam chopping period, τ. Asymmetry data acquisition begins at t_1 (t_3) and ends at t_2 (t_4) for chopper-open (chopper-closed) data. The dotted line is the extrapolation of the chopper-closed portion of the spectrum to time t_2, with its corresponding event rate labeled $R'(t_2)$. The actual chopper-open event rate at t_2 is labeled $R(t_2)$.

During acquisition of the primary data for the determination of the asymmetry, two ion counts, corresponding to the two hatched areas, are generated during each chopper period. When the chopper is open, the incident electron beam ionizes both particles in the beam and residual gas particles; when the chopper is closed, all ions are due to the residual gas. The first-order correction for ionization of the

residual gas is to subtract the ion counts with the chopper closed from the ion counts with chopper open [cf. (5.24)]. If the residual-gas pressure was constant, no further correction would be needed. However, the changes in residual-gas pressure due to beam loading and unloading require that an additional correction be made.

Referring to Figure 5.11, the steep straight line starting a t_2 (t_4) corresponds to the rapid decrease (increase) in ion counts due to the hydrogen-beam chopper closing (opening) and the sudden presence (absence) of the hydrogen beam. The more gradual increase (decrease) in ion counts between $\frac{t}{\tau} = 0$ (0.5) and t_2 (t_4) reflects the increase (decrease) in residual-gas pressure due to beam loading (unloading). The dotted line represents the component of the ion signal due to the residual gas during the time that the chopper is closing. At time t_2, the total ion-production rate is $R(t_2)$, while the ion-production rate due to the residual gas is $R'(t_2)$. The net ion-production rate, $R^{net}(t_2)$, due to the hydrogen beam is the difference between these two rates:

$$R^{net}(t_2) = R(t_2) - R'(t_2) . \qquad (5.31)$$

This net rate is assumed to be constant over the period between t_1 and t_2. The net ion counts, N_I^{net}, due to the hydrogen beam during the period from t_1 to t_2 is, therefore,

$$N_I^{net} = [R(t_2) - R'(t_2)](t_2 - t_1) . \qquad (5.32)$$

The net ion counts, $(N_I^{net})'$, determined by the first-order correction is given by

$$(N_I^{net})' = \int_{t_1}^{t_2} dt\, R(t) - \int_{t_3}^{t_4} dt\, R(t) . \qquad (5.33)$$

The beam-loading correction to the asymmetry is expressed conveniently in terms of a correction factor, ϵ, defined as

$$1 + \epsilon \equiv \frac{(N_I^{net})'}{N_I^{net}}, \qquad (5.34)$$

in terms of which the corrected counting-rate asymmetry, A, is related to the uncorrected asymmetry, A', as follows:

$$A = \frac{[1 + \epsilon(\uparrow\downarrow)]A'}{1 - \epsilon(\uparrow\downarrow)A'}, \qquad (5.35)$$

where the arrows indicate that the correction factor was determined with the polarization vectors of the incident and atomic electrons antiparallel.

The analysis proceeds as follows:

Step 1. Apply a quadratic least-squares fit to $R(t)$ just before the chopper closes. Also apply a linear least-squares fit to $R(t)$ during the period that the chopper is closing. Determine t_2 and $R(t_2)$ from the intersection of these two fits.

Step 2. Apply a quadratic least-squares fit to $R(t)$ just after the chopper closes. Extrapolate this fit to t_2 to determine $R'(t_2)$.

Step 3. Calculate N_I^{net} according to (5.32).

Step 4. Determine t_4 by a procedure similar to Step 1.

Step 5. Calculate $(N_I^{net})'$ according to (5.33).

Step 6. Calculate ϵ according to (5.34). Figure 5.12 is a plot of $\epsilon(\uparrow\downarrow)$ with the rf on.

Step 7. Correct the asymmetries according to (5.35).

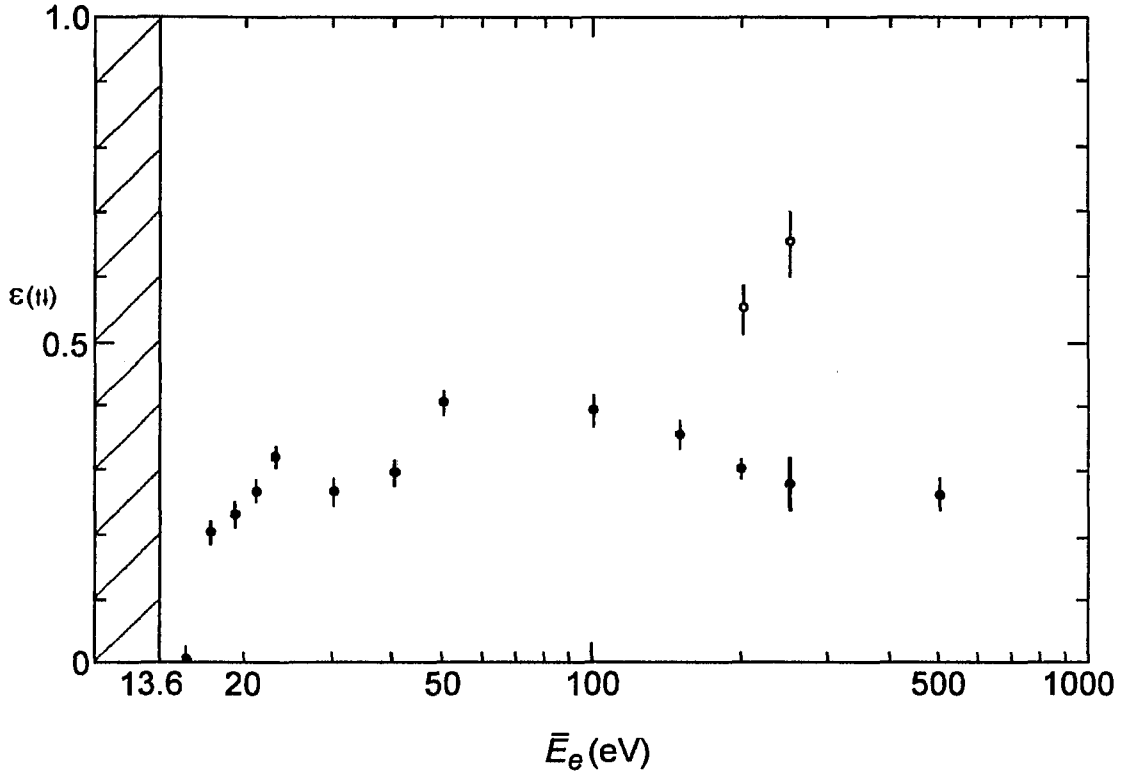

Figure 5.12 Plot of the dynamic beam-loading correction term, $\epsilon(\uparrow\downarrow)$, as a function of incident electron energy, E_e.

CHAPTER SIX: RESULTS & CONCLUSIONS

Results are presented and discussed for the parameters of the hydrogen and electron beams as well as for the asymmetry measurements. The data-acquisition procedures are described in Chapter Four; the procedures used for analyzing the data are described in Chapter Five. This chapter concludes with a proposal for the next step in the experimental program.

I. HYDROGEN BEAM

The results of the measurements of the hydrogen-beam polarization, P_H, density, $\overline{\rho}$, and dissociation fraction, F_1, are presented in Table 6.1 where they are compared with the values for the polarized-hydrogen beam used by Fletcher *et al* (1985). The value indicated value for $\overline{\rho}$ is a composite from three seperate determinations: The first determination, based upon the pressure rise in the interaction chamber upon admitting the hydrogen beam, yielded the value 6(3) x 10^9 cm^{-3}; the second determination, based upon the ion-production rate,

Table 6.1 Hydrogen-beam parameter results.

LOCATION	P_H	$\overline{\rho}$ (cm^{-3})	F_1	REFERENCES
Yale	0.50(8)	~10^9	?	Fletcher *et al* (1985)
CCNY[1]	**0.515(5)**	**~10^{10}** [2]	**0.831(4)**	**Chan *et al* (1988)**

Notes: (1) Present experiment.
(2) See text.

yielded the value 1.7(7) $\times 10^{10}$ cm^{-3}; the third determination, based upon a Monte-Carlo simulation of the beam, yielded the value 9 $\times 10^{9}$ cm^{-3}. Each of the two empirical values agrees with the Monte-Carlo value, and the agreement between the two empirical values, although less satisfactory, is acceptable. The Monte-Carlo value is probably the most accurate one for three reasons: (1) the Monte-Carlo simulation accurately predicted the deflected beam profiles used in the determination of the polarization (see Chapter Five, Section I.A), (2) both empirical determinations depend upon values generated by the Monte-Carlo simulation, and (3) the Monte-Carlo value is between the two empirical values and approximately one standard deviation from either one.

The beams at CCNY and Yale have the same polarization, which is not suprising since they both use hexapole magnets; however, the polarization is more precisely determined at CCNY through experimental measurement and is slightly, but significantly (three standard deviations), greater than 50%. The density of the CCNY beam is an order of magnitude greater than that of the Yale beam.

II. ELECTRON BEAM

The polarization, P_e, figure of merit[15], $P_e^2 Q$, and energy spread, ΔE_{FWHM}, of the present electron beam are listed in Table 6.2 where they are compared with the characteristics of other GaAs polarized-electron sources. The polarization of the present source is typical of GaAs sources. Both sources with the highest polarization (49%) are thin molecular-beam-epitaxial layers. The thinness of these layers results in relatively low quantum efficiencies and thus relatively low figures of merit. The energy spread of the current source is measured after the beam has passed through the monochromator. All of the other values listed in the table are for systems without monochromators. Four of these energy spreads are less than that of the present beam; two energy spreads are larger than that of the present beam. Kolac *et al* (1988) assert that the earlier low values are not representative of the electron beams actually used in applications of these sources because only a very small fraction of the beam was analyzed and special precautions were taken to avoid energy broadening due to space charge and the Boersch effect. Thus the larger values measured at Zürich and München are more representative of the beams used in scattering experiments. The energy spread of the present beam is reduced by the monochromator.

---

[15]It is customary with photocathodes to use $P_e^2 Q$, where Q is the quantum efficiency, rather than $P_e^2 I$, where I is the current, as the figure of merit.

Table 6.2 Characteristics of NEA GaAs polarized-electron sources[1].

LOCATION	P_e (%)	P_e^2Q (10^{-3})	ΔE_{FWHM} (meV)	REFERENCES
Zürich	40	0.16	?	Pierce & Meier (1976)
SLAC	37	11	?	Prescott *et al* (1978) Sinclair & Miller (1981)
Zürich	23	2	400	Reihl *et al* (1979)
NBS	43(2)	6	31	Pierce *et al* (1980) Feigerle *et al* (1984)
Jülich	49(1)	3.5	90	Alvarado *et al* (1981)
Bates	38(2)	17	?	Cates *et al* (1989)
Palaiseau	30	?	30	Drouhin *et al* (1985a,b)
Nagoya	10	0.4	?	Nakanishi *et al* (1986)
Münster	21	?	160	Luig *et al* (1986)
CCNY[2]	**27(2)**	**1.5**	**175**	**Guo *et al* (1990a)**
München	35(5)	7.5	300	Kolac *et al* (1988)
USA[3]	49	2.5	?	Maruyama *et al* (1989)
Perth	25(2)	1.7	?	Ranganathaiah *et al* (1990)
Milano	27(3)	?	?	Ciccacci *et al* (1994)

Notes: (1) The best value of each parameter is listed. The values listed for different parameters do not necessarily correspond to the same condition.
(2) Present experiment.
(3) Madison/SLAC/CEBAF/Champaign/Urbana.

The most promising new technology in polarized-electron sources is strained layers. The operating source at SLAC (Alley *et al* 1995) has achieved polarizations over 80%. The

figure of merit, P^2Q, is relatively low (of the order of 10^{-3}), however, because the active layer is thin (100 nm), which limits Q. This limitation is overcome by using a very-high-power laser, thus maximizing P^2I. The maximum current, I, is determined by either space charge, if Q is sufficiently high, or by a cathode charge limit (Alley *et al* 1995) if Q is below a critical value.

III. IONIZATION ASYMMETRY

The results of the ionization-asymmetry measurements are presented and discussed separately for the near-threshold region and for energies above the ionization threshold of H_2.

A. Near Threshold

The results of the ionization-asymmetry measurements in the near-threshold region have been discussed in detail in another dissertation (Guo 1991); however, Macek, Ovchinnikov and Pasovets (1995) recently published hidden-crossing-theory calculations for the asymmetry in this region. These calculated values are compared with the experimental results in Figure 6.1 and Figure 6.2. The theoretical results match the secular trend of the experimental results for energies above 14 eV, but the theoretical values are uniformly greater than the experimental values by ~10%. Below 14 eV, theory and experiment diverge, with slopes of opposite sign. Also, the theoretical spectrum does not exhibit the oscillations

apparent in the experimental spectrum. Macek, Ovchinnikov and Pasovets (1995) suggest several refinements to the theory that might improve agreement between theory and experiment. In particular, the current calculations use a basis set of only one Sturmian function. The inclusion of more Sturmian functions might result in oscillations.

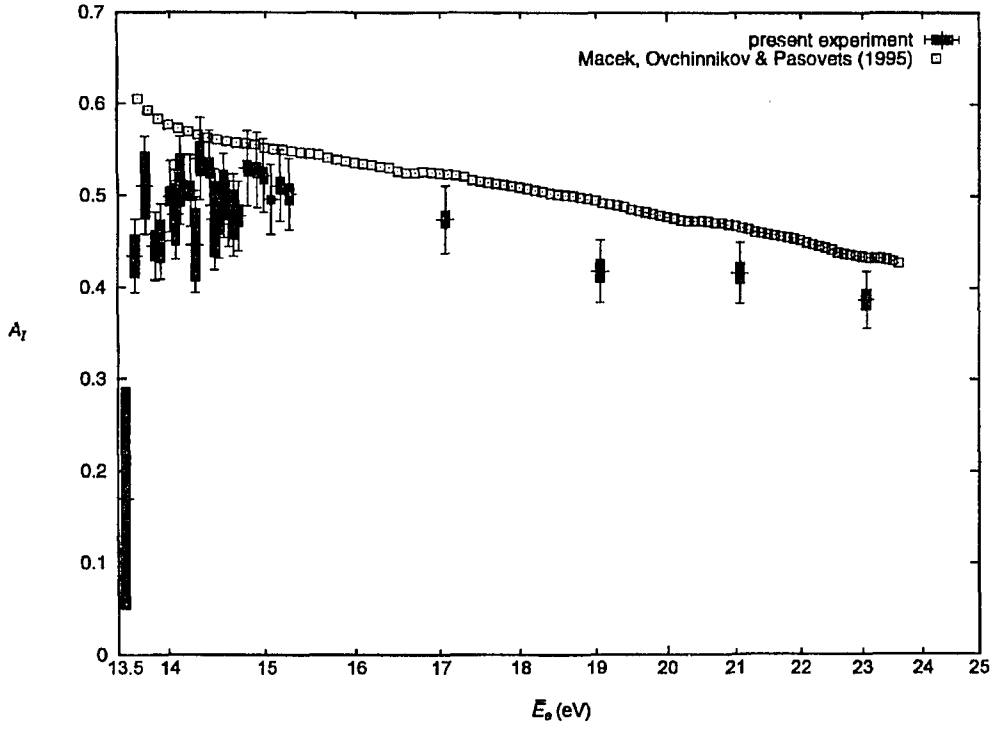

Figure 6.1 Energy spectrum of A_I from threshold to 25 eV comparing the results of the present experiment with the hidden-crossing-theory calculations of Macek, Ovchinnikov and Pasovets (1995). The solid rectangles represent the random errors associated with counting statistics. The error bars include the systematic errors associated with normalization. Note that the experimental point at 13.57 eV represents ionization by the high-energy tail of the electron distribution.

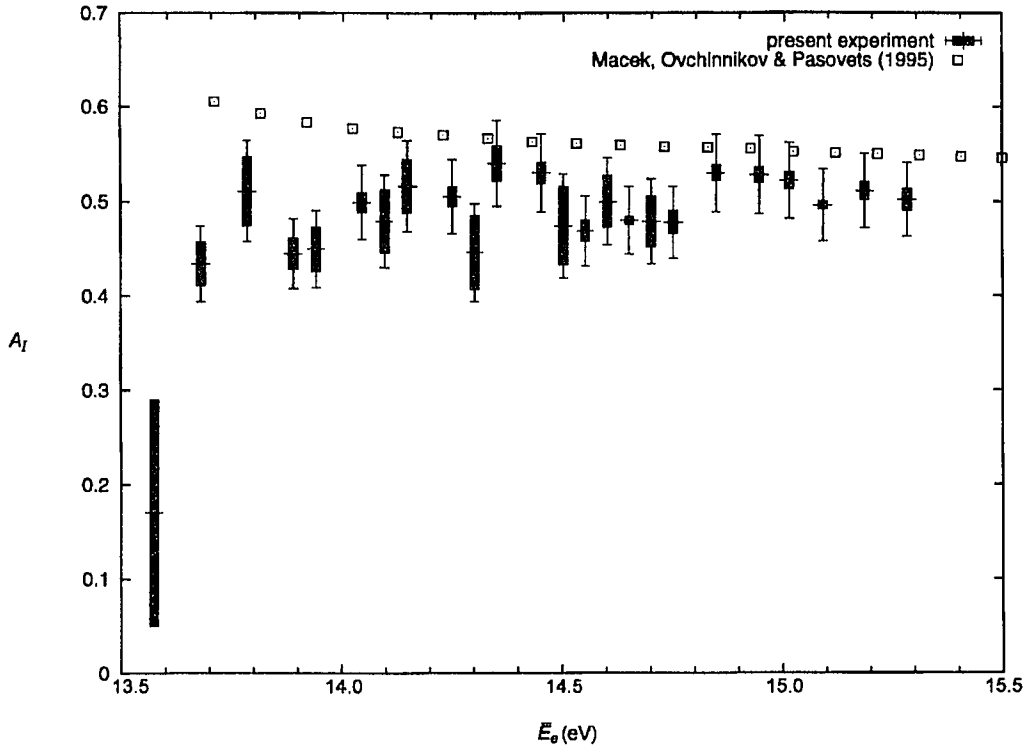

Figure 6.2 An expanded view of the near-threshold region of Figure 6.1.

Although the agreement between theory and experiment is not perfect, it is important to remember that the hidden-crossing theory is the first *ab initio* electron-impact ionization theory incorporating electron correlations in the near-threshold region. As such, it brings a new perspective to a problem that has frustrated theorists for four decades. The most successful previous theory, the Wannier theory, predicted only the energy exponent of the cross section, and its range of validity is less than 1 eV above threshold. The hidden-crossing theory not only reproduces the Wannier exponent in its leading term, but also provides the coefficient. In addition, higher-order terms in the hidden-

crossing theory extend its range of validity to at least 10 eV above threshold.[16]

B. Above H_2 Ionization Threshold

The results of the ionization-asymmetry measurements from threshold to 500 eV, with an emphasis upon the results above the ionization threshold of H_2, are listed in Table 6.3 and plotted in Figure 6.3 where they are compared with the previous measurements of Fletcher *et al* (1985) and the convergent-close-coupling (CCC) calculations of Bray and Stelbovics (1993, 1994). Many other theoretical calculations have been compared with the previous measurements (Fletcher *et al* 1985, Figure 23a); however, the level of agreement between the CCC results and experiment over the entire range from threshold to 500 eV far exceeds the agreement shown by these other theories. The predictions of one other theory, the coupled-channel optical method of Bray, Madison and McCarthy (1990), also agree well (Crowe *et al* 1990) with experiment over the range from threshold to 200 eV; however, this method greatly overestimates (Bray, Konovalov & McCarthy 1991) the total ionization cross section as measured by Shah, Elliot and Gilbody (1987). The predictions of the CCC method for both the asymmetry and the cross section agree well with experiment. The results of the other calculations are not shown in Figure 6.1 in order to avoid cluttering the graph.

---

[16]For a more detailed comparison between the hidden-crossing theory and the Wannier theory, see Chapter Two, Section II.B.

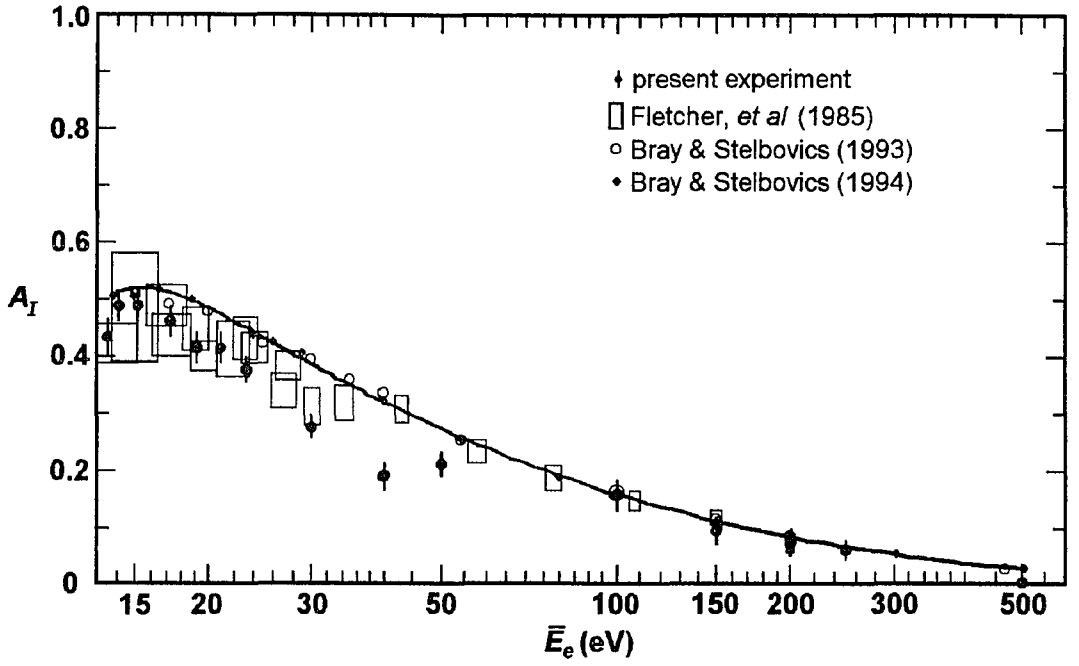

Figure 6.3 Energy spectrum of A_I from threshold to 500 eV comparing the results of the present experiment with those of the previous experiment of Fletcher *et al* (1985) and the CCC calculations of Bray and Stelbovics (1993, 1994). The solid line is drawn to aid the eye in following the theoretical points. Only two points below 15 eV are shown for the present experiment in order to avoid cluttering the graph.

The results of the present experiment agree with the previous measurements except at 40 eV. It should be remembered, however, that the present results are normalized to the previous values (cf. Chapter Five, Section II.C), and that the present value at 40 eV, as well as the value at 30 eV, were ignored during the normalization process. A systematic error of approximately ±7% results from this normalization, due mostly to the systematic error of the Mott polarimetry of the previous experiment. The present results are generally more precise, especially below 50 eV. In

Table 6.3 Asymmetry results.

$\overline{E_e}$ (eV)	A_I (1)	$\Delta_I{}^{H_1}$ (2)	$\overline{\sigma}$ (3)	σ^B (2)	σ^t (2)
			(10^{-17} cm^2)		
13.67	0.434(40)	0.0598(32)	0.04(8)	0.08(18)	0.02(5)
14.02	0.499(39)	0.0687(14)	0.23(8)	0.56(20)	0.12(4)
15.07	0.496(38)	0.0683(5)	0.80(7)	1.98(18)	0.41(5)
17.07	0.474(37)	0.0652(12)	1.73(6)	4.16(16)	0.92(7)
19.07	0.418(34)	0.0576(17)	2.64(5)	5.93(14)	1.55(9)
21.07	0.416(33)	0.0573(16)	3.36(4)	7.51(14)	1.97(11)
23.07	0.387(31)	0.0532(15)	3.93(9)	8.44(22)	2.42(13)
30.0	0.275(26)	0.0378(22)	5.07(9)	9.20(20)	3.69(14)
40.0	0.188(24)	0.0258(27)	5.81(7)	9.04(17)	4.73(15)
50.0	0.217(24)	0.0299(24)	6.26(8)	10.30(19)	4.91(16)
100.0	0.162(27)	0.0223(33)	5.45(8)	8.07(18)	4.57(16)
150.0	0.098(22)	0.0134(28)	4.61(5)	5.94(12)	4.17(11)
200.0	0.074(20)	0.0101(27)	3.96(7)	4.82(12)	3.67(10)
250.0	0.067(19)	0.0092(26)	3.42(4)	4.10(6)	3.19(8)
500.0	0.011(18)	0.0016(26)	2.03(5)	2.10(6)	2.01(6)

Notes: (1) The errors include both random errors due to counting statistics and systematic errors due to normalization.
(2) Errors are due to counting statistics only.
(3) Values from Shah, Elliot and Gilbody (1987).

addition, the energy spread of the present electron beam is more than an order of magnitude smaller than the energy spread of the previous electron beam. This difference in energy convolution does not appear to explain the discrepancy at 40 eV, however. One last observation is that the present measurements extend to 500 eV, whereas the previous measurements stopped at 200 eV. While the measured value at 500 eV is consistent with zero, which would indicate that exchange effects are negligible, it is also consistent with the nonzero value of the CCC prediction, which would indicate that exchange effects, while small, are still present.

The CCC values agree with the previous experimental measurements over the entire range from threshold to 200 eV, although they are above the mean values in most cases. The only possible disagreement is at 30 eV, but the experimental values at 27 eV tend to negate such an assessment. The agreement between the CCC values and the present measurements is less satisfactory between 19 eV and 50 eV, with the theoretical values again greater than the experimental values, but much of the discrepancy may be due to the systematic error in the normalization of the experimental values. The worst agreement is again at 40 eV. In addition, the agreement between the CCC value and the present experiment at 30 eV is poor, whereas the two experimental values are in agreement.

The results of the present experiment are are plotted together with the ionization asymmetry spectra of other atoms in Figure 6.4. Where two sets of results are available for

one atom (i.e., for H, Li, Na and K)[17] only the later, more precise set is shown in order to avoid cluttering the graph. Previous comparisons (e.g., Baum *et al* 1985) between ionization asymmetry spectra for different atoms have plotted the asymmetry as a function of E/I; however, plotting the asymmetry as a function of $E - I$ exhibits the similarities between the spectra more clearly. The first observation is that all values are positive, indicating that singlet scattering dominates over triplet scattering. Second, with the exception of K, the secular trend of all of the spectra is a positive slope for the first few eV above threshold until a peak is reached followed by a negative slope. The asymmetry spectra of H, Li and Na essentially overlap. The He* spectrum is very similar, but slightly lower. The spectra of K and Cs, the heaviest atoms studied, are ~50% lower, probably as the result of spin-orbit effects. The Cs spectrum is similar in structure to H, He*, Li and Na, but with a much more pronounced slope in the near-threshold region. The near-threshold structure of the K spectrum is anomolous.

---

[17]It should be noted that the agreement between the two sets for any one atom is not entirely satisfactory. The agreement for Na is particularly bad, even though both experiments have the same energy resolution and comparable precision. Even in the case of Li, where both sets of data were acquired in the same laboratory, the two spectra are significantly different below 15 eV. The agreement for K is better, mostly due to the poorer precision of the earlier experiment. In all three cases, the later results are uniformly higher than the earlier ones. The agreement for H is discussed above.

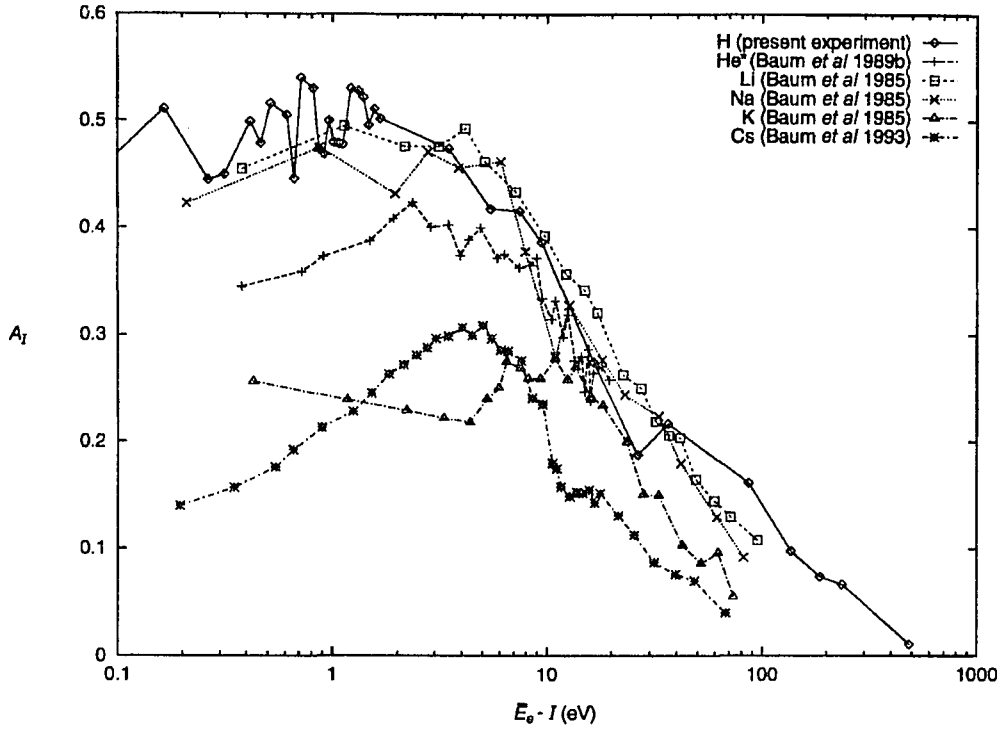

Figure 6.4 Graph comparing experimental spectra of the electron-impact ionization asymmetry for different atoms. The threshold energies, I, for the various atoms are I_H = 13.6 eV, I_{He^*} = 4.8 eV, I_{Li} = 5.39 eV, I_{Na} = 5.14 eV, I_K = 4.34 eV and I_{Cs} = 3.89 eV. The errorbars are omitted in order to avoid cluttering the graph. The lines are drawn only to guide the eye.

The singlet (σ_I^s) and triplet (σ_I^t) cross sections are calculated according to (2.23) from the measured asymmetry, A_I, and the spin-averaged cross section, $\overline{\sigma}_I$, as reported by Shah, Elliot and Gilbody (1987). The three cross sections are plotted together in Figure 6.5. The cross sections diverge at threshold and reconverge at high energies. The singlet cross section is uniformly highest throughout. The structure in σ_I^s at 40 eV reflects the structure in A_I.

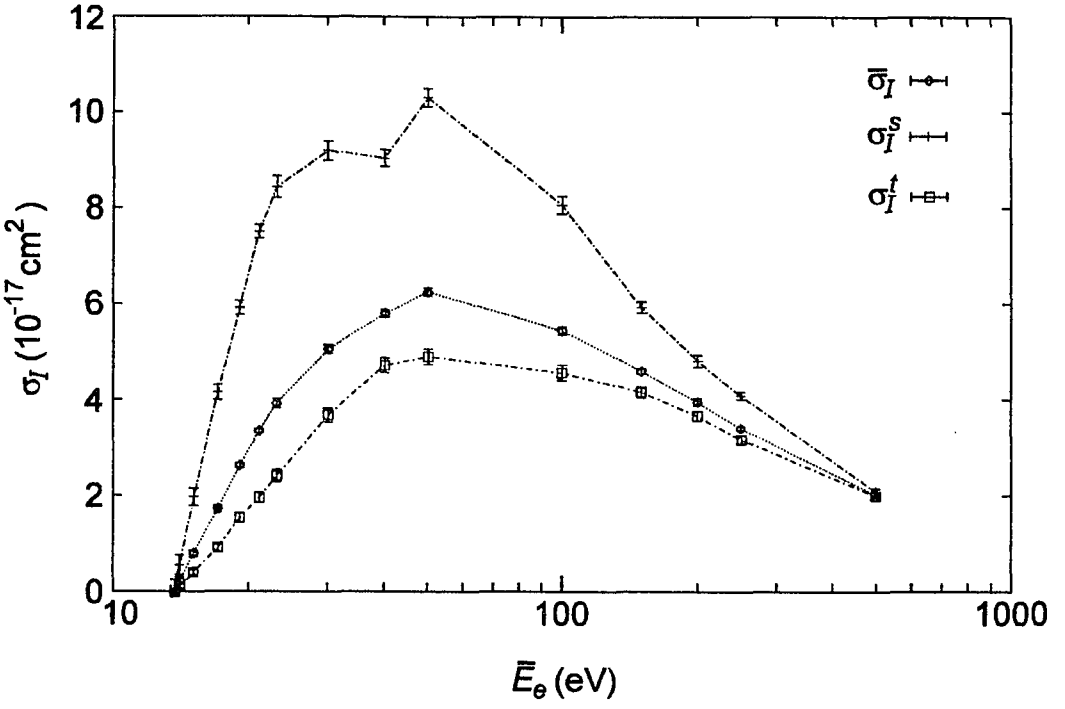

Figure 6.5 Graph comparing the energy spectra of the singlet (σ_I^s), triplet (σ_I^t) and spin-averaged ($\bar{\sigma}_I$) ionization cross sections. The values of $\bar{\sigma}_I$ are from Shah, Elliot and Gilbody (1987). The lines are drawn only to guide the eye.

IV. EXCITATION OF THE N = 2 STATES: A PROPOSAL

The next logical step in the experimental program is the measurement of the spin asymmetry for electron-impact excitation of hydrogen to the states with n = 2. The following is a proposed design for an apparatus that allows simultaneous yet separate measurement of the the spin asymmetry for excitation of the 2s and 2p states. The use of a coincidence measurement eliminates the problem of cascade in

addition to enabling differential measurements. Figure 6.6 is a schematic diagram of the proposed apparatus.

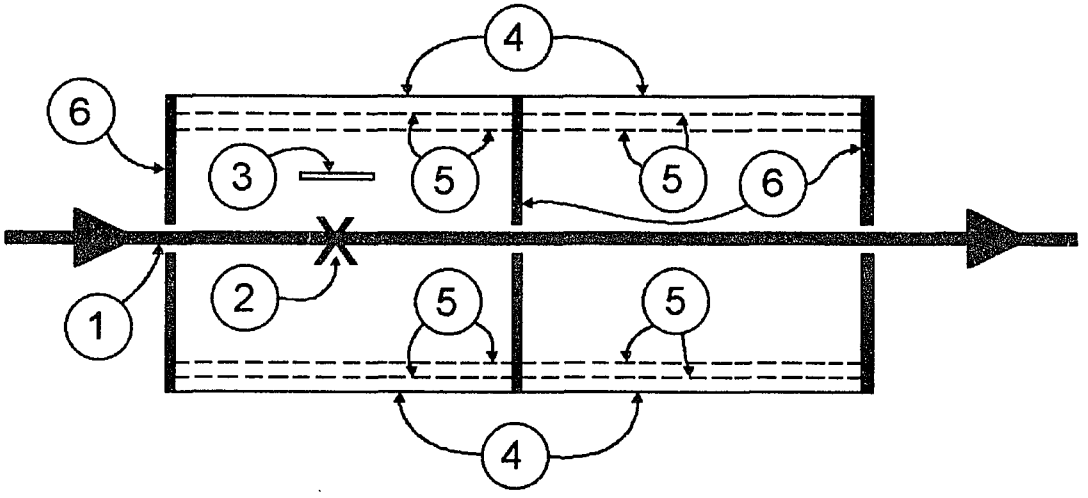

Figure 6.6 Schematic diagram of the proposed apparatus for measuring the spin asymmetry for excitation to the 2s and 2p levels. The numbered elements are (1) polarized hydrogen beam, (2) interaction point (the polarized electron beam is moving into the page), (3) electron energy analyzer entrance slit, (4) multichannel plates (5) metal grids and (6) metal plates.

The apparatus comprises two sections: the interaction section on the left and the quenching section on the right. The inner grids and the side plates in the interaction section are grounded in order to keep the region free of electric fields. The inner grids in the quenching section are biased to generate an electric field.

Atoms excited to the 2s and 2p states are detected by the Lyman-alpha (L_α) photons they emit. Atoms excited to the 2p state spontaneously emit L_α photons with a half life of only 2.1 ns (Wiese & Martin 1989). These photons are detected by the multichannel plates in the interaction section. The outer

grids serve two purposes: (1) they prevent scattered electrons from striking the multichannel plates and (2) they prevent secondary electrons generated by L_α photons striking the multichannel plates from escaping. These purposes are attained by applying a negative bias to the outer grids and a less negative, or perhaps positive, bias to the input side of the multichannel plates. A much greater positive bias is applied to the output side of the multichannel plates.

The 2s state is metastable with a lifetime of the order of 0.1 s in the absence of an electric field. Metastable atoms are quenched in an external electric field: the field destroys the spherical symmetry, thereby inducing an admixture of 2p which then decays rapidly by L_α emission. The metastable atoms generated by electron impact drift downstream without decaying until they reach the quenching section. A second set of multichannel plates then detects the resulting L_α photons. The outer grids serve the same puposes as before.

If the energy of the incident electrons exceeds the threshold (12.1 eV) for excitation to the n = 3 states, cascade becomes a problem: atoms excited to higher-energy states emit photons and decay to the n = 2 states which can then emit L_α photons. The electron energy analyzer is used to detect only those atoms that have been excited directly to the n = 2 states. The analyzer is tuned to detect only electrons with energies equal to the incident energy minus the excitation energy (10.2 eV) of the n = 2 states. The energy spread of the incident beam is not problematic as long as it

is of the order of 1 eV FWHM or less, since the neighboring channels are at 0 eV (elastic scattering) and 12.1 eV. The electron beam used in the present experiment, for example, has an energy spread of ~0.2 eV FWHM.

REFERENCES

Alguard, M. J., V. W. Hughes, M. S. Lubell & P. F. Wainwright (1977) *Measurement of spin-exchange effects in electron-hydrogen collisions: Impact ionization* **Physical Review Letters 39**, 334-8.

Alguard, M. J., J. E. Clendenin, R. D. Ehrlich, V. W. Hughes, J. S. Ladish, M. S. Lubell, K. P. Schüler, G. Baum, W. Raith, R. H. Miller & W. Lysenko (1979) *A source of highly polarized electrons at the Stanford Linear Accelerator Center* **Nuclear Instruments and Methods 163**, 29-59.

Allen, F. G. & G. W. Gobeli (1963) *High vacuum deposition of cesium* **Review of Scientific Instruments 34**, 184-5.

Allenspach, R., F. Meier & D. Pescia (1984) *Spin polarized photoemission from GaAs and Ge: Temperature dependence of the threshold polarization* **Applied Physics Letters 44**, 1107-9.

Alley, R., H. Aoyagi, J. Clendenin, J. Frisch, C. Garden, E. Hoyt, R. Kirby, L. Klaisner, A. Kulikov, R. Miller, G. Mulhollan, C. Prescott, P. Sáez, D. Schultz, H. Tang, J. Turner, K. Witte, M. Woods, A. D. Yeremian & M. Zolotorev (1995) *The Stanford linear accelerator polarized electron source* **SLAC-PUB-95-6489**.

Alvarado, S. F., F. Coccacco, S. Valeri, M. Campagna, R. Feder & H. Pleyer (1981) *Spin polarized photoemission from molecular beam epitaxy-grown Be-doped GaAs* **Zeitschrift für Physik B44**, 259-64.

Alvarado, S. F., F. Ciccacci & M. Campagna (1981) *GaAs-$Al_xGa_{1-x}As$ superlattices as sources of polarized photoelectrons* **Applied Physics Letters 39**, 615-7.

Amaldi, V., A. Egidi, R. Marconero & G. Pizella (1969) *Use of a two channeltron coincidence in a new line of research in atomic physics* **Review of Scientific Instruments 40**, 1001-4.

Anderson, David L. (1964) **The Discovery of the Electron: The Development of the Atomic Concept of Electricity** (NY: van Nostrand).

Anderson, Herbert (ed.) (1989) **A Physicist's Desk Reference: The Second Edition of Physics Vade Mecum** (NY: American Institute of Physics).

Aoyagi, H., H. Horinaka, Y. Kamiya, T. Kato, T. Kosugoh, S. Nakamura, T. Nakanishi, S. Okumi, T. Saka, M. Tawada & M. Tsubata (1992) *Strain dependence of spin polarization of photoelectrons from a thin GaAs layer* **Physics Letters A167**, 415-20.

Arianer, J., I. Brissaud, S. Essabaa, H. Humblot & W. Zerhouni (1993) *The Orsay polarized electron source from a flowing helium afterglow* **Nuclear Instruments & Methods in Physics Research A337**, 1-2.

Baum, G. & U. Koch (1969) *A source of polarized electrons* **Nuclear Instruments and Methods 71**, 189-95.

Baum, G., E. Kisker, W. Raith, W. Schröder, U. Sillmen & D. Zenses (1981) *Spin-dependent electron impact ionisation of lithium from threshold to 80 eV* **Journal of Physics B14**, 4377-88.

Baum, G., M. Moede, W. Raith & W. Schröder (1985) *Measurement of spin asymmetries in the electron impact ionisation of alkali atoms* **Journal of Physics B18**, 531-8.

Baum, G., M. Moede, W. Raith & U. Sillmen (1986) *Measurement of spin dependence in low-energy elastic scattering of electrons from lithium atoms* **Physical Review Letters 57**, 1855-8.

Baum, G., L. Frost, W. Raith & U. Sillmen (1989a) *Spin asymmetries in the low-energy electron impact excitation of 2S → 2P transitions in lithium atoms* **Journal of Physics B22**, 1667-77.

Baum, G., M. Fink, W. Raith, H. Steidl & J. Taborski (1989b) *Polarized electron-impact ionization of metastable helium* **Physical Review A40**, 6734-6.

Baum, G., B. Granitza, L. Grau, B. Leuer, W. Raith, K. Rott, M. Tondera & B. Witthuhn (1993) *Spin asymmetry in electron impact ionization of caesium* **Journal of Physics B26**, 331-6.

Beaty, E. C., K. H. Hesselbacher, S. P. Hong & J. H. Moore (1977) *Triple-differential three-dimensional cross sections for low-energy electron impact ionization of helium* **Journal of Physics B10**, 611-20.

Bederson, B., H. Malamud & J. Hammer (1957) *Elastic scattering of electrons by atomic hydrogen* (abstract only) **Bulletin of the American Physical Society 2**, 172.

Bederson, Benjamin & Thomas M. Miller (1976) *Spin polarization in electron-atom scattering* in Kleinpoppen & McDowell (1976) pp. 191-202.

Bell, Ronald L. & William E. Spicer (1970) *3-5 compound photocathodes: A new family of photoemitters with greatly improved performance* **Proceedings of the IEEE 58**, 1788-801.

Bell, R. L. (1973) **Negative Electron Affinity Devices** (Oxford: Clarendon Press).

Belushkina, A. A., V. P. Vadeev, A. I. Valevich, G. I. Gai, E. D. Donets, V. P. Ershov, L. S. Kotova, Yu. A. Plis, Yu. K. Pilipenko & V. V. Smelyanskii (1976) *Cryogenic source of polarized hydrogen and deuterium atoms* **Instrum. Exp. Tech. 19**, 1618-22.

Bennewitz, H. G. & W. Paul (1954) *Eine Methode zur Bestimmung von Kernmomenten mit fokussiertem Atomstrahl* **Zeitschrift für Physik 139**, 489-97.

Berger, O., J. Kessler, K. J. Kollath, R. Möllenkamp & W. Wübker (1981) *"Triple" scattering experiment for the maximum possible information on elastic scattering from mercury* **Physical Review Letters 46**, 768-70.

Berkovits, V. L., A. I. Ekimov & V. I. Safarov (1974) *Optical orientation in a system of electrons and lattice nuclei in semiconductors. Experiment* **Soviet Physics JETP 38**, 169-76.

Beurtey, R., A. Papineau & J. Thirion (1961) *Sources de protons et deutons polarisès* **Il Nuovo Cimento 19, Supplemento 2**, 207-20.

Bir, G. L., A. G. Aronov & G. E. Pikus (1976) *Spin relaxation of electrons due to scattering by holes* **Soviet Physics JETP 42**, 705-12.

Bleakney, W. (1929) *A new method of positive ray analysis and its application to the measurement of ionization potentials in mercury vapor* **Physical Review 34**, 157-60.

Bonner, William A., Mark A. Van Dort & Mason R. Yearian (1975) *Asymmetric degradation of DL-leucine with longitudinally polarised electrons* **Nature 258**, 419-21.

Born, M. & E. Wolf (1964) **Principles of Optics**, 2nd ed. (NY: Macmillan).

Boucher, Paul Edward (1922) *The measurement of the resonance, radiation and ionization potentials of several gases and vapors* **Physical Review 19**, 189-209.

Boutry, Georges-Albert, Robert Évrard & Jean-Claude Richard (1964) *Contribution à l'étude des propriétés photoélectroniques du césium pur, préparé et conservé dans l'ultravide* **Comptes Rendus de l'Académie des Sciences 258**, 143-6.

Boyd, R. L. F & G. W. Green (1958) *Electron ionization cross sections using chopped beams* **Proceeding of the Physical Society** (London) **71**, 351-6.

Brackmann, R. T., Wade L. Fite & Roy H. Neynaber (1958) *Collisions of electrons with hydrogen atoms. III. Elastic scattering* **Physical Review 112**, 1157-61.

Bray, I., D. H. Madison & I. E. McCarthy (1990) *Coupled-channel optical calculation of electron-hydrogen scattering: The distorted-wave optical potential* **Physical Review A41**, 5916-28.

Bray, I., D. A. Konovalov & I. E. McCarthy (1991) *Coupled-channel optical calculation of electron-hydrogen scattering: Elastic scattering from 0.55 to 30 eV* **Physical Review A43**, 5878-85.

Bray, I. & A. T. Stelbovics (1992) *Convergent close-coupling calculations of electron-hydrogen scattering* **Physical Review A46**, 6995-7011.

Bray, Igor & Andris T. Stelbovics (1993) *Calculation of the total ionization cross section and spin asymmetry in electron-hydrogen scattering from threshold to 500 eV* **Physical Review Letters 70**, 746-9.

Bray, Igor & Andris T. Stelbovics (1994) private communication.

Burstein, E., G. S. Picus, R. F. Wallis & F. Blatt (1959) *Zeeman-type magneto-optical studies of interband transitions in semiconductors* **Physical Review 113**, 15-33.

Calabrese, R., G. Ciullo, V. Guidi, G. Lamanna, P. Lenisa, B. Maciga, L. Tecchio & B. Yang (1994) *Long-lifetime high-intensity GaAs photosource* **Review of Scientific Instruments 65**, 343-8.

Campagna, M., S. F. Alvarado & F. Ciccacci (1983) *Solid state polarized electron sources* **AIP Conference Proceedings 95**, 566-73.

Campbell, D. M., H. M. Brash & P. S. Farago (1971) *A source of polarized electrons using spin exchange* **Physics Letters 36A**, 449-50.

Cates, G. D., V. W. Hughes, R. Michaels, H. R. Schaefer, T. J. Gay, M. S. Lubell, R. Wilson, G. W. Dodson, K. A. Dow, S. B. Kowalski, K. Isakovich, K. S. Kumar, M. E. Schulze, P. A. Souder & D. H. Kim (1989) *The Bates polarized electron source* **Nuclear Instruments and Methods in Physics Research A278**, 293-317.

Chan, N., D. M. Crowe, M. S. Lubell, F. C. Tang, A. Vasilakis, M. J. Mulligan & J. Slevin (1988) *A polarized atomic hydrogen beam* **Zeitschrift für Physik D10**, 393-415.

Chelikowsky, James R. & Marvin L. Cohen (1974) *Electronic structure of GaAs* **Physical Review Letters 32**, 674-7.

Chelikowsky, James R. & Marvin L. Cohen (1976) *Nonlocal pseudopotential calculations for the electronic structure of eleven diamond and zinc-blende semiconductors* **Physical Review B14**, 556-82.

Ciccacci, F., S. F. Alvarado & S. Valeri (1982) *Spin-polarized phoelectron emission study of $Al_xGa_{1-x}As$ alloys grown by molecular beam epitaxy* **Journal of Applied Physics 53**, 4395-8.

Ciccacci, F., H.-J. Drouhin, C. Hermann, R. Houdré, G. Lampel & F. Alexandre (1988) *Energy and spin polarization analysis of near band gap photoemission in AlGaAs/GaAs heterostructures* **Solid-State Electronics 31**, 489-92.

Ciccacci, F., H.-J. Drouhin, C. Hermann, R. Houdré & G. Lampel (1989) *Spin-polarized photoemission from AlGaAS/GaAs: A convenient highly polarized electron source* **Applied Physics Letters 54**, 632-4.

Ciccacci, F., G. Chiaia, S. De Rossi & P. Lenisa (1994) *Calibrating the spin polarization in electron beams from NEA GaAs photocathodes by means of electron spectroscopy* **Nuclear Instruments and Methods in Physics Research A340**, 122-6.

Clark, A. H., R. D. Burnham, D. J. Chadi & R. M. White (1975) *Spin relaxation of conduction electrons in $Al_xGa_{1-x}As$* **Physical Review B12**, 5758-65.

Clark, A. H., R. D. Burnham, D. J. Chadi & R. M. White (1976) *Spin relaxation of conduction electrons in GaAs* **Solid State Communications 20**, 385-7.

Collins, Richard E., Marvin Goldstein, Benjamin Bederson & Kenneth Rubin (1967) *Elastic differential spin-exchange cross sections for scattering of slow electrons by potassium* **Physical Review Letters 19**, 1366-8.

Collins, R. E., B. Bederson, M. Goldstein & K. Rubin (1968) *Potassium-electron elastic spin-exchange: Comparison of experiment with a close-coupling calculation* **Physics Letters 27A**, 440-1.

Collins, R. E., B. Bederson & M. Goldstein (1971) *Differential spin exchange and the elastic scattering of low-energy electrons by potassium* **Physical Review A3**, 1976-87.

Compton, Arthur H. (1921) *Possible magnetic polarity of free electrons* **Philosophical Magazine and Journal of Science 41**, 279-81.

Compton, K. T. (1922) *A tungsten furnace for experiments on dissociation and ionization* **Journal of the Optical Society of America and Review of Scientific Instruments 6**, 910-2.

Conrath, D., T. Heindorff, A. Hermanni, N. Ludwig & E. Reichert (1979) *Photoemission of spin-polarized electrons from negative electron affinity GaAsP* **Applied Physics 20**, 155-7.

Coplan, M. A., J. H. Moore & J. P. Doering (1994) *(e,2e) spectroscopy* **Reviews of Modern Physics 66**, 985-1014.

Cox, R. T., C. G. McIlwraith & B. Kurrelmeyer (1928) *Apparent evidence of polarization in a beam of β-rays* **Proceedings of the National Academy of Sciences 14**, 544-9.

Crowe, D. M., X. Q. Guo, M. S. Lubell, J. Slevin & M. Eminyan (1990) *Spin-tagged electron-hydrogen scattering: New measurements of ionisation asymmetries from threshold to 500 eV* **Journal of Physics B23**, L325-31.

Davis, Luther, Jr., Bernard T. Feld, Carrol W. Zabel & Jerrold R. Zacharias (1949) *The hyperfine structure and nuclear moments of the stable chlorine isotopes* **Physical Review 76**, 1076-85.

Defrance, P., W. Claeys, A. Cornet & G. Poulaert (1981) *Electron impact ionisation of metastable atomic hydrogen* **Journal of Physics B14**, 111-7.

Deichsel, H. (1961) *Herstellung und Nachweis polarisierter Elektronenstrahlen durch zweimalige Streuung von Glühelektronen kleiner Energie (1-2 keV) an Hg-Atomstrahlen* **Zeitschrift für Physik 164**, 156-65.

Ding, A., J. Karlau & J. Weise (1977) *Production of H-atom and O-atom beams by a cooled microwave discharge source* **Review of Scientific Instruments 48**, 1002-4.

Dirac, P. A. M. (1928) *The quantum theory of the electron* **Proceedings of the Royal Society of London A117**, 610-24.

Dixon, A. J., A. Von Engel & M. F. A. Harrison (1975) *A measurement of the electron impact ionization cross section of atomic hydrogen in the metastable 2S state* **Proceedings of the Royal Society of London A343**, 333-49.

Dresselhaus, G. (1955) *Spin-orbit coupling effects in zinc blende structures* **Physical Review 100**, 580-6.

Drouhin, H.-J., C. Hermann, M. Eminyan & G. Lampel (1983) *Photoelectron energy distribution and spin polarization from activated gallium arsenide* **Journal de Physique Lettres 44**, L-1027-34.

Drouhin, H.-J., C. Hermann & G. Lampel (1985a) *Photoemission from activated gallium arsenide. I. Very-high-resolution energy distribution curves* **Physical Review B31**, 3859-71.

Drouhin, H.-J., C. Hermann & G. Lampel (1985b) *Photoemission from activated gallium arsenide. II. Spin polarization versus kinetic energy analysis* **Physical Review B31**, 3872-86.

Duffendack, O. S. (1922) *Low voltage arcs in diatomic gases. I. Hydrogen, nitrogen, and iodine.* **Physical Review 20**, 665-87.

D'yakonov, M. I. & V. I. Perel' (1971) *Spin orientation of electrons associated with the interband absorption of light in semiconductors* **Soviet Physics JETP 33**, 1053-9.

Dzhioev, R. I., B. P. Zakharchenya & V. G. Fleisher (1971) *Optical orientation of electron spins and band splitting in doped semiconductors* **JETP Letters 14**, 381-4.

Dzhioev, R. I., V. G. Fleisher, L. M. Kanskaya, O. A. Ninu & B. P. Zakharchenya (1972) *Optical spin orientation of non-equilibrium electrons in GaAs and GaAs-AlAs solid solution* **Physica Status Solidi B50**, 39-43.

Eichenbaum, A. L. & M. E. Moi (1964) *Cesium vapor dispenser* **Review of Scientific Instruments 35**, 691-3.

Ekimov, A. I. & V. I. Safarov (1970) *Optical orientation of carriers in interband transitions in semiconductors* **JETP Letters 12**, 198-201.

Ekimov, A. I. & V. I. Safarov (1971a) *Observation of optical orientation of equilibrium electrons in n-type semiconductors* **JETP Letters 13**, 177-9.

Ekimov, A. I. & V. I. Safarov (1971b) *Influence of spin relaxation of 'hot' electrons on the effectiveness of optical orientation in semiconductors* **JETP Letters 13**, 495-8.

Ekimov, A. I. & V. I. Safarov (1972a) *Optical detection of dynamic polarization of nuclei in semiconductors* **JETP Letters 15**, 179-81.

Ekimov, A. I. & V. I. Safarov (1972b) *Optical electron-nuclear resonance in semiconductors* **JETP Letters 15**, 319-21.

Elliott, R. J. (1954) *Theory of the effect of spin-orbit coupling on magnetic resonance in some semiconductors* **Physical Review 96**, 266-79.

Erbudak, M. & B Reihl (1978) *Depolarization of photoelectrons emitted from optically pumped GaAs* **Applied Physics Letters 37**, 584-5.

Ehrhardt, H., M. Schulz, T. Tekaat & K. Willmann (1969) *Ionization of helium: Angular correlation of the scattered and ejected electrons* **Physical Review Letters 22**, 89-92.

Escher, John S. (1981) *NEA semiconductor photoemitters* **Semiconductors and Semimetals 15**, 195-300

Fano, U. (1969) *Spin orientation of photoelectrons ejected by circularly polarized light* **Physical Review 178**, 131-6; *Spin orientation of photoelectrons: Erratum and addendum* **Physical Review 184**, 250-1.

Feigerle, C. S., D. T. Pierce, A. Seiler & R. J. Celotta (1984) *Intense source of monochromatic electrons: Photoemission from GaAs* **Applied Physics Letters 44**, 866-8.

Fite, Wade L. & R. T. Brackmann (1958a) *Collisions of electrons with hydrogen atoms. I. Ionization* **Physical Review 112**, 1141-51.

Fite, Wade L. & R. T. Brackmann (1958b) *Collisions of electrons with hydrogen atoms. II. Excitation of Lyman-alpha radiation* **Physical Review 112**, 1151-6.

Fite, Wade L., R. F. Stebbings & R. T. Brackmann (1959a) *Collisions of electrons with hydrogen atoms. IV. Excitation of Lyman-alpha radiation near threshold* **Physical Review 116**, 356-7.

Fite, Wade L., R. T. Brackmann, David G. Hummer & R. F. Stebbings (1959b) *Lifetime of the 2s state of atomic hydrogen* **Physical Review 116**, 363-7; (errata) **Physical Review 124**, 2051 (1961).

Fleisher, V. G., R. I. Dzhioev, B. P. Zakharchenya & L. M. Kanskaya (1971) *Spin relaxation of electrons oriented by light in a GaAs crystal* **JETP Letters 13**, 299-302.

Fletcher, G. D., M. J. Alguard, T. J. Gay, V. W. Hughes, C. W. Tu, P. F. Wainwright, M. S. Lubell, W. Raith & F. C. Tang (1982) *Measurement of spin-exchange effects in electron-hydrogen collisions: 90° elastic scattering from 4 to 30 eV* **Physical Review Letters 48**, 1671-4.

Fletcher, G. D., M. J. Alguard, T. J. Gay, V. W. Hughes, P. F. Wainwright, M. S. Lubell & W. Raith (1985) *Experimental study of spin-exchange effects in elastic and ionizing collisions of polarized electrons with polarized hydrogen atoms* **Physical Review A31**, 2854-84.

Foner, S. N. & B. H. Nall (1961) *Structure in the ionization near threshold of rare gases by electron impact* **Physical Review 122**, 512-24.

Fox, R. E., W. M. Hickam, T. Kjeldaas, Jr. and D. J. Groves (1951) *Ionization potentials and probabilities using a mass spectrometer* **Physical Review 84**, 859-60.

Friedburg, H. & W. Paul (1951) *Optische Abbildung mit neutralen Atomen* **Naturwissenschaften 38**, 159-60.

Friedburg, Helmut (1951) *Optische Abbildung mit neutralen Atomen* **Zeitschrift für Physik 130**, 493-512.

Friedman, J. R., X. Q. Guo, M. S. Lubell & M. R. Frankel (1992) *Reexamination of tests of the Wannier threshold law for two-electron escape* **Physical Review A46**, 652-5.

Fues, E. & H. Hellmann (1930) *Über polarisierte Elektronenwellen* **Physikalische Zeitschrift 31**, 465-78.

Funk, Hans (1930) *Über die Ionisierung von Alkaliatomen durch langsame Elekronen* **Annalen der Physik 4**,149-84.

Garbuzov, D. Z., A. I. Ekimov & V. I. Safarov (1971) *Measurement of the lifetime and of the spin-relaxation time of electrons in semiconductors by the optical-orientation method* **JETP Letters 13**, 24-6.

Garbuzov, D. Z., R. I. Dzhioev, L. M. Kanskaya & V. G. Fleisher (1972) *Surface influence on the optical orientation of electron spins in semiconductors* **Soviet Physics Solid State 14**, 1481-7.

Garwin, E. L., D. T. Pierce & H. C. Siegmann (1974) *Polarized photoelectrons from optically magnetized semiconductors* **Helvetica Physica Acta 47**, 393.

Gay, T. J., G. D. Fletcher, M. J. Alguard, V. W. Hughes, P. F. Wainwright & M. S. Lubell (1982) *Measurement of spin-exchange effects in electron-hydrogen collisions: Further studies of impact ionization* **Physical Review A26**, 3664-7.

Gay, T. J. & F. B. Dunning (1992) *Mott electron polarimetry* **Review of Scientific Instruments 63**, 1635-51.

Gerlach, Walther & Otto Stern (1922) *Der experimentelle Nachweis der Richtungsquantelung im Magnetfeld* **Zeitschrift für Physik 9**, 349-55.

Gilbody, H. B., R. F. Stebbings & Wade L. Fite (1961) *collisions of electrons with hydrogen atoms. VI. Angular distribution in elastic scattering* **Physical Review 121**, 794-8.

Goldenberg, H. M., D. Kleppner & N. F. Ramsey (1960) *Atomic hydrogen maser* **Physical Review Letters 5**, 361-2.

Goldstein, Marvin, Abraham Kasdan & Benjamin Bederson (1972) *Differential cross sections with spin analysis for $4^2S_{1/2} \rightarrow 4^2P_{1/2,3/2}$ excitation of potassium by electrons* **Physical Review A5**, 660-8.

Gray, L. G., K. W. Giberson, Chu Cheng, R. S. Keiffer, F. B. Dunning & G. K. Walters (1983) *Intense source of spin-polarized electrons using laser-induced optical pumping* **Review of Scientific Instruments 54**, 271-4.

Guo, X. Q., D. M. Crowe, M. S. Lubell, F. C. Tang, A. Vasilakis, M. Eminyan & J. Slevin (1990a) *Further observations on the operation of a GaAs polarized electron source* **Review of Scientific Instruments 61**, 1858-62.

Guo, X. Q., D. M. Crowe, M. S. Lubell, F. C. Tang, A. Vasilakis, J. Slevin & M. Eminyan (1990b) *Spin-tagged electron-hydrogen scattering: Ionization in the near-threshold region* **Physical Review Letters 65**, 1857-60.

Guo, Xiao-Qin (1991) **Test of the Ionization Threshold Law through Spin-Dependent Collisions of Electrons and Hydrogen Atoms** (doctoral dissertation, CUNY).

Guo, X. Q. & M. S. Lubell (1993) *Energy dependence of the spin asymmetry for electron impact ionization of atomic hydrogen and its implications for the Wannier theory of double escape* **Journal of Physics B26**, 1221-32.

Hanne, G. F. & J. Kessler (1974) *Direct observation of exchange scattering by spin flip of polarized electrons in excitation of mercury* **Physical Review Letters 33**, 341-3.

Hanne, G. F. & J. Kessler (1976a) *Direct observation of exchange scattering by spin flip of polarized electrons in excitation of mercury* in Kleinpoppen & McDowell (1976) pp. 445-54.

Hanne, G. F. & J. Kessler (1976b) *Study of exchange excitation in mercury by means of polarized electrons I. Experiment* **Journal of Physics B9**, 791-804.

Harnwell, Gaylord P. (1929) *Electron scattering in atomic and molecular hydrogen* **Physical Review 34**, 661-72; *Note on electron scattering in atomic and molecular hydrogen* (addendum) **Physical Review 35**, 285 (1930).

Harting, E. & F. H. Read (1976) **Electrostatic Lenses** (NY: Elsevier).

Hecht, Eugene & Alfred Zajac (1974) **Optics** (Reading, MA: Addison-Wesley).

Hegemann, T., M. Oberste-Vorth, R. Vogts & G. F. Hanne (1991) *Study of exchange in collisions of polarized electrons with atoms and molecules* **Physical Review Letters 66**, 2968-71.

Hendrie, J. M. (1954) *Dissociation energy of N_2* **Journal of Chemical Physics 22**, 1503-7.

Hermann, Claudine & Georges Lampel (1971) *Measurement of the g factor of conduction electrons by optical detection of spin resonance in p-type semiconductors* **Physical Review Letters 27**, 373-6.

Hershcovitch, A., A. Kponou & T. O. Niinikoski (1987) *Cold high-intensity atomic hydrogen beam source* **Review of Scientific Instruments 58**, 547-56.

Herzog, R. F. (1934) *Ionen- und elektronenoptische Zylinderlinsen und Prismen I* **Zeitschrift für Physik 89**, 447-73.

Herzog, R. F. (1935) *Ablenkung von Kathoden- und Kanalstrahlen am Rande eines Kondensators, dessen Streufeld durch eine Blende begrenzt ist* **Zeitschrift für Physik 97**, 596-602.

Hill, J. C., L. L. Hatfield, N. D. Stockwell & G. K. Walters (1972) *Direct demonstration of spin-angular-momentum conservation in the reaction $He(2^3S_1) + He(2^3S_1) \rightarrow He(1^1S_0) + He^+ + e^-$* **Physical Review A5**, 189-95.

Hils, D., M. V. McCusker, H. Kleinpoppen & S. J. Smith (1972) *Differential and direct differential elastic scattering cross sections for electrons and potassium atoms* **Physical Review Letters 29**, 398-401.

Hils, D. & H. Kleinpoppen (1978) *The ionisation of polarised potassium atoms by polarised electrons* **Journal of Physics B11**, L283-7.

Hils, D., K. Rubin & H. Kleinpoppen (1980) *Ionization of polarized alkali atoms by polarized electrons* in Kleinpoppen & Williams (1980) pp. 689-96.

Hils, D., W. Jitschin & H. Kleinpoppen (1982) *The spin-dependent ionisation asymmetry in sodium* **Journal of Physics B15**, 3347-57.

Hodge, L. A., F. B. Dunning & G. K. Walters (1979) *Intense source of spin-polarized electrons* **Review of Scientific Instruments 50**, 1-4.

Hofmann, M., G. Regenfus, O. Schärpf & P. J. Kennedy (1967) *Measurements of the polarization of field emitted electrons from polycrystalline gadolinium* **Physics Letters 25A**, 270-1.

Hood, S. T., E. Weigold & A. J. Dixon (1979) *Electron-photon angular correlations in the electron impact excitation of H(2p)* **Journal of Physics B12**, 631-48.

Houdrè, R., C. Hermann, G. Lampel, P. M. Frijlink & A. C. Gossard (1985) *Photoemission from a superlattice and a single quantum well* **Physical Review Letters 55**, 734-7.

Hughes, A. Ll., & Elias Klein (1924) *Ionization of gases as a function of the energy of electron impacts* **Physical Review 23**, 450-63.

Hughes, V. W., R. L. Long, M. S. Lubell, M. Posner & W. Raith (1972) *Polarized electrons from photoionization of polarized alkali atoms* **Physical Review A5**, 195-222.

Jaduszliwer, Bernardo, Natarajan D. Bhaskar & Benjamin Bederson (1976) *Differential spin exchange in the elastic scattering of low-energy electrons by rubidium* **Physical Review A14**, 162-8.

Jammer, Max (1966) **The Conceptual Development of Quantum Mechanics** (NY: McGraw-Hill).

Jitschin, W., S. Osimitsch, H. Reihl, H. Kleinpoppen & H. O. Lutz (1984) *Electron exchange in the Na 3p electron impact excitation* **Journal of Physics B17**, 1899-912.

Jolly, William Lee (1974) *Hydrogen and its compounds* **Encyclopædia Britannica**, 15th ed., Macropædia, v. 9, pp. 93-7.

Jones, T. J. (1927) *Probability of ionization of mercury vapor by electron impact* **Physical Review 29**, 822-9.

Joseph, C. & J. Soffer (eds.) (1981) **High Energy Physics with Polarized Beams and Polarized Targets** (Bäsel: Birkhäuser).

Jost, Klaus & Joachim Kessler (1966) *Zur Polarisation langsamer Elektronen durch Streuung an Quecksilber zwischen 180 und 1700 eV* **Zeitschrift für Physik 195**, 1-12.

Jaduszliwer, Bernardo, Natarajan D. Bhaskar & Benjamin Bederson (1976) *Differential spin exchange in the elastic scattering of low-energy electrons by rubidium* **Physical Review A14**, 162-8.

Kauppila, W. E., W. R. Ott & W. L. Fite (1970) *Excitation of atomic hydrogen to the metastable $2^2S_{\frac{1}{2}}$ state by electron impact* **Physical Review A1**, 1099-108.

Keller, R. (1957) Report CERN 57-30 (Geneva).

Khakoo, M. (1995) private communication.

Keliher, P. J., F. B. Dunning, M. R. O'Neill, R. D. Rundel & G. K. Walters (1975) *Spin conservation during chemi-ionization and surface-electron ejection by He(2^3S)* **Physical Review A11**, 1271-8.

Keliher, P. J., R. E. Gleason & G. K. Walters (1975) *Intense polarized electron beams from chemi-ionization reactions with optically pumped He(2^3S)* **Physical Review A11**, 1279-85.

Kelly, M. H., W. T. Rogers, R. J. Celotta & S. R. Mielczarek (1983) *Near-threshold measurement of the spin dependence of electron-impact ionization* **Physical Review Letters 51**, 2191-3.

Kessler, J. & J. Lorenz (1970) *Experimental verification of the Fano effect* **Physical Review Letters 24**, 87-8.

Kessler, Joachim (1985) **Polarized Electrons**, 2nd ed. (NY: Springer-Verlag).

Kieffer, L. J. & Gordon H. Dunn (1966) *Electron ionization cross-section data for atoms, atomic ions, and diatomic molecules: I. Experimental data* **Reviews of Modern Physics 38**, 1-35.

Kirschner, J., H. P. Oepen & H. Ibach (1983) *Energy- and spin-analysis of polarized photoelectrons from NEA GaAsP* **Applied Physics A30**, 177-83.

Kisker, E., G. Baum, A. H. Mahan, W. Raith & B. Reihl (1978) *Electron field emission from ferromagnetic europium sulfide on tungsten* **Physical Review B18**, 2256-75.

Klein, Wolfgang (1971) *A molecular beam cesium source for photoemission experiments* **Review of Scientific Instruments 42**, 1082-3.

Kleinpoppen, H. & M. R. C. McDowell (1976) (*International Symposium on*) **Electron and Photon Interactions with Atoms** (*University of Stirling, 16-19 July 1974*) (NY: Plenum).

Kleinpoppen, H. & J. F. Williams (eds.) (1980) (*The International Workshop on*) **Coherence and Correlation in Atomic Collisions** (NY: Plenum).

Kolac, U., M. Donath, K. Ertl, H. Liebl & V. Dose (1988) *High-performance GaAs polarized electron source for use in inverse photoemission spectroscopy* **Review of Scientific Instruments 59**, 1933-40.

Koschmieder, H., V. Raible & H. Kleinpoppen (1973) *Resonance structure in the excitation cross section by electron impact of the 2s state in atomic hydrogen* **Physical Review A8**, 1365-8.

Kunz, Jacob & J. T. Tykociner (1929) *Electrodeless ring discharge and the production of atomic rays of hydrogen* (abstract only) **Physical Review 33**, 117.

Kunz, Jacob (1933) *Application of a vibrating velocity selector for the determination of the magnetic moment of hydrogen* (abstract only) **Physical Review 44**, 323.

Kurihara, Yoshimasa, Tsunehiko Omori, Yasunori Takeuchi, Masakazu Yoshioka, Tsutomu Nakanishi, Syooji Okumi, Mmasabumi Tawada, Kazuaki Togawa, Mitsuru Tsubata, Toshio Baba, Masashi Mizuta, Raymond K. Alley, Hideki Aoyagi, James E. Clendenin, Josef C. Frisch, Gregory A. Mulhollan, Pablo J. Sáez, David C. Schultz, Huan Tang & Klaus H. Witte (1995) *A high polarization and high quantum efficiency photocathode using a GaAs-AlGaAs superlattice* **Japanese Journal of Applied Physics, Part 1, 34**, 355-8.

Kuskevics, G. & B. Thompson (1966) *Surface ionization source of cesium ions* **Review of Scientific Instruments 37**, 710-2.

Lamb, Willis E., Jr. & Robert C. Retherford (1950) *Fine structure of the hydrogen atom. Part I* **Physical Review 79**, 41-64.

Lamb, Willis E., Jr. & Robert C. Retherford (1951) *Fine structure of the hydrogen atom. Part II* **Physical Review 81**, 222-32.

Lampel, Georges (1968) *Nuclear dynamic polarization by optical electronic saturation and optical pumping in semiconductors* **Physical Review Letters 20**, 491-3.

Lampel, G. & C. Weisbuch (1975) *Proposal for an efficient source of polarized photoelectrons from semiconductors* **Solid State Communications 16**, 877-80.

Lawrence, Ernest O. (1926) *The ionization of atoms by electron impact* **Physical Review 28**, 947-61.

Lichten, William & Sheldon Schultz (1959) *Cross sections for the excitation of the metastable 2s state of atomic hydrogen by electron impact* **Physical Review 116**, 1132-9.

Lloyd, C. R., P. J. O. Teubner, E. Weigold & B. R. Lewis (1974) *Differential cross sections for the elastic scattering of electrons form atomic hydrogen. II. Medium energies* **Physical Review A10**, 175-81.

Lohmann, B. & E. Weigold (1981) *Direct measurement of the electron momentum probability distribution in atomic hydrogen* **Physics Letters 86A**, 139-41.

Long, R. L., Jr., W. Raith & V. W. Hughes (1965) *Polarized electrons from a polarized atomic beam* **Physical Review Letters 15**, 1-4.

Lubell, M. S. & W. Raith (1969) *Polarization effect in photoionization of cesium* **Physical Review Letters 23**, 211-4.

Lubell, M. S. (1980) *Polarized-beams studies of spin exchange in electron-hydrogen collisions* in Kleinpoppen & Williams (1980) pp. 663-87.

Luig, T., M. Rissmann & H. Merz (1986) *Double-step excitation in spin photoemission from NEA GaAs(100)* **Solid State Communications 58**, 775-9.

Macek, J. H., S. Yu. Ovchinnikov & S. V. Pasovets (1995) *Hidden crossing theory of threshold ionization of atoms by electron impact* **Physical Review Letters 74**, 4631-4.

Madey, Theordore E. & John T. Yates, Jr. (1971) *Electron-stimulated desorption and work function studies of clean and cesiated (110) GaAs* **Journal of Vacuum Science and Technology 8**, 39-44.

Märk, T. D. & G. H. Dunn (eds.) (1985) **Electron Impact Ionization** (NY: Springer-Verlag).

Marton, Ladislaus L. (1974) *Photoelectric effect* **Encyclopædia Britannica**, 15th ed., Macropædia, v. 14, pp. 296-300.

Marton, L. & C. Marton (1980) *Evolution of the concept of the elementary charge* **Advances in Electronics and Electron Physics 50**, 449-72.

Maruyama, T., R. Prepost, E. L. Garwin, C. K. Sinclair, B. Dunham & S. Kalem (1989) *Enhanced electron spin polarization in photoemission from thin GaAs* **Applied Physics Letters 55**, 1686-8.

Maruyama, T., E. L. Garwin, R. Prepost, G. H. Zapalac, J. S. Smith, J. D. Walker (1991) *Observation of strain-enhanced electron-spin polarization in photoemission from InGaAs* **Physical Review Letters 66**, 2376-9.

Maruyama, T., E. L. Garwin, R. Prepost & G. H. Zapalac (1992) *Electron-spin polarization in photoemission from strained GaAs grown on* $GaAs_{1-x}P_x$ **Physical Review B46**, 4261-4.

Maruyama, T., E. L. Garwin, R. A. Mair, R. Prepost, J. S. Smith & J. D. Walker (1993) *Electron-spin polarization in*

photoemission from thin $Al_xGa_{1-x}As$ **Journal of Applied Physics 73**, 5189-92.

Massey, H. S. W. & C. B. O. Mohr (1941) *The polarization of electrons by double scattering* **Proceedings of the Royal Society of London A177**, 341-57.

McCarthy, I. E., E. Weigold, X. Zhang & Y. Zheng (1989) *Ionisation of atomic hydrogen at intermediate momentum transfer* **Journal of Physics B22**, 931-8.

McClelland, J. J., M. H. Kelley & R. J. Celotta (1986) *Spin-dependent superelastic scattering from pure angular momentum states of Na(3P)* **Physical Review Letters 56**, 1362-5.

McClelland, J. J., M. H. Kelley & R. J. Celotta (1987) *Spin-orbit and exchange effects in elastic scattering of spin-polarized electrons from spin-polarized Na atoms* **Physical Review Letters 58**, 2198-200.

McClelland, J. J., M. H. Kelley & R. J. Celotta (1989) *Superelastic scattering of spin-polarized electrons from sodium* **Physical Review A40**, 2321-9.

McCusker, M. V., L. L. Hatfield & G. K. Walters (1969) *Intense polarized electron beams from optically pumped helium discharges* **Physical Review Letters 22**, 817-20.

McCusker, M. V., L. L. Hatfield & G. K. Walters (1972) *Cumulative ionization in optically pumped helium discharges: A source of polarized electrons* **Physical Review A5**, 177-89.

McGowan, J. William & E. M. Clarke (1968) *Ionization of H(1s) near threshold* **Physical Review 167**, 43-51.

McGowan, J. William, M. A. Fineman, E. M. Clarke & H. P. Hanson (1968) *Direct and auto-ionization of H_2 near threshold* **Physical Review 167**, 52-60.

Mergl, E., E. Geisenhofer & W. Nakel (1991) *GaAsP spin-polarized electron source for a 300 keV accelerator* **Review of Scientific Instruments 62**, 2318-21.

Millman, S., I. I. Rabi & J. R. Zacharias (1938) *On the nuclear moments of indium* **Physical Review 53**, 384-91.

Mohr, C. B. O. & R. H. Nicoll (1934) *The scattering of electrons in ionizing collisions with gas atoms* **Proceedings of the Royal Society of London A144**, 596-608.

Möllenkamp, R. & U. Heinzmann (1982) *A source of highly spin-polarised slow electrons based on the 'Fano effect' on caesium atoms* **Journal of Physics E15**, 692-6.

Moore, John H., Christopher C. Davis & Michael A. Coplan (1983) **Building Scientific Apparatus** (Don Mills, Ontario: Addison-Wesley).

Mott, N. F. (1929) *The scattering of fast electrons by atomic nuclei* **Proceedings of the Royal Society of London A124**, 425-42.

Mott, N. F. (1932) *The polarisation of electrons by double scattering* **Proceedings of the Royal Society of London A135**, 429-58.

Motz, J. W., H. Olsen & H. W. Koch (1964) *Electron scattering without atomic or nuclear excitation* **Reviews of Modern Physics 36**, 881-928.

Müller, N., W. Eckstein, W. Heiland & W. Zinn (1972) *Electron spin polarization in field emission from EuS-coated tungsten tips* **Physical Review Letters 29**, 1651-4.

Murphy, Edmond J. & John H. Brophy (1979) *Atomic hydrogen beam source: A convenient, extended cavity, microwave discharge design* **Review of Scientific Instruments 50**, 635-6.

Myers, F. E., J. F. Byrne & R. T. Cox (1934) *Diffraction of electrons as a search for polarization* **Physical Review 46**, 777-85.

Nagle, Darragh E., Renne S. Julian & Jerrold R. Zacharias (1947) *The hyperfine structure of atomic hydrogen and deuterium* **Physical Review 72**, 971.

Nakanishi, Tsutomu, Kazuhiko Dohmae, Shuji Fukui, Yoshikazu Hayashi, Ikuo Hirose, Naoaki Horikawa, Tetsuaki Ikoma, Yoshihiro Kamiya, Mitsuru Kurashina & Shoji Okumi (1986) *Construction of GaAs spin-polarized electron source and measurements of electron polarization* **Japanese Journal of Applied Physics 25**, 766-7.

Nakanishi, T., H. Aoyagi, H. Horinaka, Y. Kamiya, T. Kato, S. Nakamura, T. Saka & M. Tsubata (1991) *Large enhancement of spin polarization observed by photoelectrons from a strained GaAs layer* **Physics Letters A158**, 345-9.

Neynaber, R., Lawrence L. Marino, Erhard W. Rothe & S. M. Trujillo (1961) *Scattering of low-energy electrons by atomic hydrogen* **Physical Review 124**, 135-6.

Olmstead, P. S. & K. T. Compton (1923) *Radiation potentials of atomic hydrogen* **Physical Review 22**, 559-65.

Omori, T., Y. Kurihara, T. Nakanishi, H. Aoyagi, T. Baba, T. Furuya, K. Itoga, M. Mizuta, S. Nakamura, Y. Takeuchi, M. Tsubata & M. Yoshioka (1991) *Large enhancement of*

polarization observed by extracted electrons from the AlGaAs-GaAs superlattice **Physical Review Letters 67**, 3294-7.

Omori, Tsunehiko, Yoshimasa Kurihara, Yasunori Takeuchi, Masakazu Yoshioka, Tsutomu Nakanishi, Shoji Okumi, Mitsuru Tsubata, Masafumi Tawada, Kazuaki Togawa, Yasunori Tanimoto, Chikako Takahashi, Toshio Baba & Masashi Mizuta (1994) *Highly polarized electron source using InGaAs-GaAs strained-layer superlattice* **Japanese Journal of Applied Physics, Part 1, 33**, 5676-80.

Ott, W. R., W. E. Kauppila & W. L. Fite (1967) *Polarization of Lyman-alpha radiation produced in collisions of electrons and hydrogen atoms* **Physical Review Letters 19**, 1361-3.

Ott, W. R., W. E. Kauppila & W. L. Fite (1970) *Polarization of Lyman-α radiation emitted in electron collisions with hydrogen atoms and molecules* **Physical Review A1**, 1089-98.

Parsons, R. R. (1969) *Band-to-band optical pumping in solids and polarized photoluminescence* **Physical Review Letters 23**, 1152-4.

Pauli, W., jr. (1925) *Über den Zusammenhang Abschlusses der Elektrongruppen im Atom mit der Komplexstruktur der Spektren* **Zeitschrift für Physik 31**, 765-85.

Peterkop, R. (1971) *WKB approximation and threshold law for electron-atom ionization* **Journal of Physics B4**, 513-21.

Phipps, T. E. & J. B. Taylor (1927) *The magnetic moment of the hydrogen atom* **Physical Review 29**, 309-20.

Pierce, D. T., F. Meier & P. Zürcher (1975a) *Direct observation of spin dependent electronic structure of GaAs using spin polarized photoemission* **Physics Letters 51A**, 465-6.

Pierce, D. T., F. Meier & P. Zürcher (1975b) *Negative electron affinity GaAs: A new source of spin-polarized electrons* **Applied Physics Letters 26**, 670-2.

Pierce, Daniel T. & Felix Meier (1976) *Photoemission of spin-polarized electrons from GaAs* **Physical Review B13**, 5484-500.

Pierce, D. T., G. C. Wang & R. J. Celotta (1979) *Face dependence of the spin polarization of photoelectrons from NEA GaAs (100) and (110)* **Applied Physics Letters 35**, 220-2.

Pierce, D. T., R. J. Celotta, G.-C. Wang, W. N. Unertl, A. Galejs, C. E. Kuyatt & S. R. Mielczarek (1980) *GaAs spin polarized electron source* **Review of Scientific Instruments 51**, 478-99.

Prescott, C. Y., W. B. Atwood, R. L. A. Cottrell, H. DeStaebler, Edward L. Garwin, A. Gonidec, R. H. Miller, L. S. Rochester, T. Sato, D. J. Sherden, C. K. Sinclair, S. Stein, R. E. Taylor, J. E. Clendenin, V. W. Hughes, N. Sasao, K. P. Schüler, M. G. Borghini, K. Lübelsmeyer & W. Jentschke (1978) *Parity non-conservation in inelastic electron scattering* **Physics Letters 77B**, 347-52.

Rabi, I. I., J. M. B. Kellogg & J. R. Zacharias (1934) *The magnetic moment of the proton* **Physical Review 46**, 157-63.

Ramsey, Norman F. (1956) **Molecular Beams** (Oxford: Clarendon).

Ranganathaiah, C., J. L. Robins, A. L. Yates, W. C. Macklin, R. A. Anderson & J. F. Williams (1990) *Characteristics of a source and detector of spin polarized electrons* **Journal of Electron Spectroscopy and Related Phenomena 51**, 331-8.

Ratcliff, J. M., G. H. Rutherford, F. B. Dunning & G. K. Walters (1989) *Electron exchange collisions with O_2 and NO* **Physical Review A39**, 5584-7.

Rau, A. R. P. (1971) *Two electrons in a Coulomb potential. Double-continuum wave functions and threshold law for electron-atom ionization* **Physical Review A4**, 207-20.

Reihl, B., M Erbudak & D. M. Campbell (1979) *Production of spin-polarized electrons by photoemission from GaAs(110)* **Physical Review B19**, 6358-66.

Reichert, E. & K Zähringer (1982) *Electron spin polarization in the photoemission of NEA $GaAs_{1-x}P_x$* **Applied Physics A29**, 191-3.

Reichert, E. (1983) *A source of polarized electrons for a neutral current parity experiment* **AIP Conference Proceedings 95**, 580-5.

Riechert, H., H.-J. Drouhin & C. Hermann (1988) *Energy-resolved study of the spin precession in photoemission from activated (110) GaAs* **Physical Review B38**, 4136-55.

Risler, R., W. Grüebler, V. König & P. A. Schmelzbach (1974) *Investigation of a polarized neutral atomic beam* **Nuclear Instruments and Methods 121**, 425-30.

Roth, Laura M., Benjamin Lax & Solomon Zwerdling (1959) *Theory of optical magneto-absorption effects in semiconductors* **Physical Review 114**, 90-104.

Roth, T. A. (1972) *Threshold law for double photoionization and related processes with L = 1 final states* **Physical Review A5**, 476-8.

Rothe, Erhard W., Lawrence L. Marino, R. H. Neynaber & S. M. Trujillo (1962) *Electron impact ionization of atomic hydrogen and atomic oxygen* **Physical Review 125**, 582-3.

Rougeot, H. & C. Baud (1979) *Negative Electron Affinity Photoemitters* **Advances in Electronics and Electron Physics 48**, 1-36.

Rubin, Kenneth, Julius Perel & Benjamin Bederson (1960) *Measurement of the total, differential, and exchange cross sections for the scattering of low-energy electrons by potassium* **Physical Review 117**, 151-8.

Rubin, K., B. Bederson, M. Goldstein & R. E. Collins (1969) *Electron-alkali-metal inelastic recoil experiments with spin analysis: Experimental method and the small-angle behavior of the* $4^2S_{1/2} \rightarrow 4^2P_{1/2,3/2}$ excitation of potassium **Physical Review 182**, 201-14.

Saka, Takashi, Toshihiro Kato, Tsutomu Nakanishi, Mitsuru Tsubata, Katsumi Kishino, Hiromichi Horinaka, Yoshihiro Kamiya, Shoji Okumi, Chikako Takahashi, Yasunori Tanimoto, Masafumi Tawada, Kazuaki Togawa, Hideki Aoyagi & Shinsuke Nakamura (1993) *New-type photocathode for polarized electron source with distributed Bragg reflector* **Japanese Journal of Applied Physics, Part 2, 32**, L1837-40.

Schade, H., H. Nelson & H. Kressel (1972) *Novel GaAs-(AlGa)As cold-cathode structure and factors affecting extended operation* **Applied Physics Letters 20**, 385-7.

Schaefer, D. L. (1970) *A cesium ion source and an oxygen source for photoemission studies* **Review of Scientific Instruments 41**, 274-5.

Scheer, J. J. & J. van Laar (1965) *GaAs-Cs: A new type of photoemitter* **Solid State Communications 3**, 189-93.

Schlemmer, P., T. Rösel, K. Jung & H. Ehrhardt (1989) *(e,2e) investigation of atomic hydrogen and helium close to threshold* **Physical Review Letters 63**, 252-4.

Schultz, D., R. Alley, H. Aoyagi, J. Clendenin, J. Frisch, C. Garden, E. Hoyt, R. Kirby, L. Klaisner, A. Kulikov, G. Mulhollan, C. Prescott, P. Saez, H. Tang. J. Turner, M. Woods, D. Yeremian & M. Zolotorev (1994) *The high peak current polarized electron source of the Stanford Linear Collider* **Nuclear Instruments & Methods in Physics Research A340**, 127-32.

Seaton, M. J. (1951) *A comparison of theory and experiment for photo-ionization cross-sections II. Sodium and the alkali metals* **Proceedings of the Royal Society of London A208**, 418-30.

Shah, M. B., D. S. Elliott & H. B. Gilbody (1987) *Pulsed crossed-beam study of the ionisation of atomic hydrogen by electron impact* **Journal of Physics B20**, 3501-14.

Sherman, Noah (1956) *Coulomb scattering of relativistic electrons by point nuclei* **Physical Review 103**, 1601-7.

Shull, C. G., C. T. Chase & F. E. Myers (1943) *Electron polarization* **Physical Review 63**, 29-37.

Shyn, T. W. (1992) *Doubly differential cross sections of secondary electrons ejected from atomic hydrogen by electron impact* **Physical Review A45**, 2951-6.

Simon, R. E. (1963) **Quarterly Report 17, U. S. Army Contract DA 36-039-AMC-02221(E).**

Simon, R. E. & C. R. Fuselier (1964) *Research in electron emission from semiconductors* **Final Report, U. S. Army Contract DA36 039AMC02221E** (NTIS accession number AD-446 723/9).

Sinclair, C. K., E. L. Garwin, R. H. Miller & C. Y. Prescott (1976) *A high intensity polarized electron source for the Stanford Linear Accelerator* **AIP Conference Proceedings 35**, 424-31.

Sinclair, Charles K. (1981) *High intensity polarized electron sources* in Joseph & Soffer (1981) pp. 27-33.

Sinclair, Charles K. & Roger H. Miller (1981) *A high current, short pulse, rf synchronized electron gun for the Stanford Linear Accelerator* **IEEE Transactions on Nuclear Science NS-28**, 2649-51.

Sinclair, C. K. (1985) *Report on the May 1983 polarized electron source workshop at SLAC* **Journal de Physique 46**, (C2-669)-(C2-682).

Singy, D., P. A. Schmelzbach, W. Grüebler & W. Z. Zhang (1990) *Study of the surface recombination in the production of a dense polarized hydrogen beam at low temperature* **Nuclear Instruments and Methods in Physics Research B47**, 167-80.

Slack, Francis G. (1926) *The duration of radiation excited in hydrogen by 10.2 volt electron impacts* **Physical Review 28**, 1-12.

Slevin, J., M. Eminyan, J. M. Woolsey, G. Vassilev & H. Q. Porter (1980) *Electron-photon angular correlation measurements for excitation of the 2P state of hydrogen at 55 and 100 eV* **Journal of Physics B13**, L341-5.

Slevin, J. & W. Stirling (1981) *Radio frequency atomic hydrogen beam source* **Review of Scientific Instruments 52**, 1780-2.

Slevin, J., M. Eminyan, J. M. Woolsey, G. Vassilev, H. Q. Porter, C. G. Back & S. Watkin (1982) *Electron-photon angular correlation measurements for the 2P state of hydrogen at 35 eV* **Physical Review A26**, 1344-9.

Smith, D. L. & D. A. Huchital (1972) *Adsorption kinetics of Cs on GaAs* **Journal of Applied Physics 43**, 2624-8.

Sonnenberg, H. (1971) *Long-wavelength photoemission from* $InAs_{1-x}P_x$ **Applied Physics Letters 19**, 431-3.

Souder, P., A. Barber, W. Bertozzi, G. Cates, G. Dodson, T. J. Gay, M. Goodman, V. W. Hughes, S. Kowalski, M. S. Lubell, A. Magnon, C. P. Sargent, R. Schaefer, W. Turchinetz & R. Wilson (1983) *Polarized electron source for parity experiment at Bates* **AIP Conference Proceedings 95**, 574-9.

Spicher, Gottfried, Björn Olsson, Wilhelm Raith, Günther Sinapius & Wolfgang Sperber (1990) *Ionization of atomic hydrogen by positron impact* **Physical Review Letters 64**, 1019-22.

Stebbings, R. F., Wade L. Fite, David G. Hummer & R. T. Brackmann (1960) *Collisions of electrons with hydrogen atoms. V. Excitation of metastable 2s hydrogen atoms* **Physical Review 119**, 1939-45; (errata) **Physical Review 124**, 2051-2 (1961).

Tang, F. C., M. S. Lubell, K. Rubin, A. Vasilakis, M. Eminyan & J. Slevin (1986) *Operating experience with a GaAs photoemission electron source* **Review of Scientific Instruments 57**, 3004-11.

Tang, Fu-Ching (1989) **Spin-Tagged Electron-Hydrogen Scattering: Ionization in the Near Threshold Region** (doctoral dissertation, CUNY).

Taylor, John R. (1972) **Scattering Theory: The Quantum Theory of Nonrelativistic Collisions** (Malabar, FL: Robert E. Krieger).

Teubner, P. J. O., C. R. Lloyd & E. Weigold (1973) *The differential cross section for elastic scattering of electrons from atomic hydrogen* **Journal of Physics B6**, L134-7.

Teubner, P. J. O., C. R. Lloyd & E. Weigold (1974) *Differential cross section for elastic scattering of electrons from atomic hydrogen: Low energies* **Physical Review A9**, 2252-8.

Thomson, G. P. (1930) **The Wave Mechanics of Free Electrons** (NY: McGraw-Hill) pp. 148-51.

Thomson, J. J. (1891) *On the discharge of electricity through exhausted tubes without electrodes* **Philosophical Magazine and Journal of Science 32**, 321-36, 445-64.

Thomson, J. J. (1897) *Cathode rays* **Philosophical Magazine and Journal of Science 44**, 293-311.

Thomson, J. J. (1899) *On the masses of the ions in gases at low pressure* **Philosophical Magazine and Journal of Science 48**, 547-67.

Thomson, J. J. (1927) *The electrodeless discharge through gases* **Philosopical Magazine and Journal of Science 4**, 1128-60.

Thonemann, P. C., J. Moffatt, D. Roaf & J. H. Sanders (1948) *The performance of a new radio-frequency ion source* **Proceedings of the Physical Society** (London) **61**, 483-5.

Triebwasser, Sol, Edward S. Dayhoff & Willis E. Lamb, Jr. (1953) *Fine structure of the hydrogen atom. V* **Physical Review 89**, 98-106.

Turnbull, A. A. & G. B. Evans (1968) *Photoemission from GaAs-Cs-O* **Journal of Physics D1**, 155-60.

Uebbing, John J. (1970) *Use of Auger electron spectroscopy in determining the effect of carbon and other surface contaminants on GaAs-Cs-O photocathodes* **Journal of Applied Physics 41**, 802-4.

Uhlenbeck, G. E. & S. Goudsmit (1925) *Ersetzung der Hypothese vom unmechanischen Zwang durch eine Forderung bezüglich des inneren Verhaltens hedes einzelnen Elektrons* **Die Naturwissenschaften 13**, 953-4.

Uhlenbeck, G. E. & S. Goudsmit (1926) *Spinning electrons and the structure of spectra* **Nature 177**, 264-5.

van Laar, J. & J. J. Scheer (1968) *Photoemission of semiconductors* **Philips Technical Review 29**, 54-66.

von Drachenfels, W., U. T. Koch, Th. M. Müller, W. Paul & H. R. Schaefer (1977) *A pulsed source for polarized electrons with high repetition rate* **Nuclear Instruments and Methods 140**, 47-55.

Wainwright, P. F., M. J. Alguard, G. Baum & M. S. Lubell (1978) *Application of a dc Fano effect polarized electron source to low-energy electron-atom scattering* **Review of Scientific Instruments 49**, 571-85.

Walraven, J. T. M. & Isaac F. Silvera (1982) *Helium-temperature beam source of atomic hydrogen* **Review of Scientific Instruments 53**, 1167-81.

Wannier, Gregory H. (1953) *The threshold law for single ionization of atoms or ions by electrons* **Physical Review 90**, 817-25.

Weber, Roland E. & Linus F. Cordes (1966) *Aluminosilicate alkali ion sources* **Review of Scientific Instruments 37**, 112-3.

Weigold, E., S. T. Hood, I. Fuss & A. J. Dixon (1977) *Ionisation of atomic hydrogen: Angular correlations of the outgoing electrons* **Journal of Physics B10**, L623-7.

Weigold, E., C. J. Noble, S. T. Hood & I. Fuss (1979) *Electron impact ionisation of atomic hydrogen: Experimental and theoretical (e,2e) differential cross sections* **Journal of Physics B12**, 291-313.

Weigold, Erich (1980) *Coincidence investigations of electron--hydrogen collisions* in Kleinpoppen & Williams (1980) pp. 59-66.

Weigold, E., L. Frost & K. J. Nygaard (1980) *Large-angle electron-photon coincidence experiment in atomic hydrogen* **Physical Review A21**, 1950-4.

Weisbuch, C. & G. Lampel (1974) *Spin-dependent recombination and optical orientation in semiconductors* **Solid State Communications 14**, 141-4.

Whetten, N. R. & J. R. Young (1959) *Use of a silver tube to admit oxygen to a vacuum system* **Review of Scientific Instruments 30**, 472-3.

Wiese, Wolfgang L. & Georgia A. Martin (1989) *Atomic spectroscopy* in Anderson (1989) pp. 92-102.

Williams, Brown F. & J. J. Tietjen (1971) *Current status of negative electron affinity devices* **Proceedings of the IEEE 59**, 1489-97.

Williams, J. F. (1974) *Differential cross sections for the elastic scattering of electrons from atomic hydrogen at low energies* **Journal of Physics B7**, L56-60.

Williams, J. F. & B. A. Willis (1974) *Electron excitation of the 2p state of atomic hydrogen near threshold* **Journal of Physics B7**, L61-5.

Williams, J. F. (1975a) *Electron scattering from hydrogen atoms II. Elastic scattering at low energies from 0.5 to 8.7 eV* **Journal of Physics B8**, 1683-92.

Williams, J. F. (1975b) *Electron scattering from hydrogen III. Absolute differential cross sections for elastic scattering of electrons of energies from 20 to 680 eV* **Journal of Physics B8**, 2191-9.

Williams, J. F. (1976) *The 2S and 2P state excitation of atomic hydrogen* **Journal of Physics B9**, 1519-27.

Williams, J. F. (1981) *Electron-photon angular correlations from the electron impact excitation of the 2s and 2p electronic configurations of atomic hydrogen* **Journal of Physics B14**, 1197-217.

Wilmers, M., R. Haug & H. Deichsel (1969) *Über die Herstellung eines niederenergetischen, polarisierten Elektronenstrahles* **Zeitschriften Angewarten Physik 27**, 204-6.

Wilson, C. T. R. (1923) *Investigation on x-rays and β-rays by the cloud method. Part II.--β-rays.* **Proceedings of the Royal Society of London A104**, 192-212.

Wood, R. W. (1922a) *Atomic hydrogen and the Balmer series spectrum* **Philosophical Magazine and Journal of Science 44**, 538-46.

Wood, R. W. (1922b) *Spontaneous incandescenc of substances in atomic hydrogen gas* **Proceedings of the Royal Society of London A102**, 1-9.

Wübker, W., R. Möllenkamp & J. Kessler (1982) *"Perfect" elastic e⁻-Xe scattering experiment* **Physical Review Letters 49**, 272-5.

Yashin, Yu. P., A. I. Klimin, Yu. A. Mamaev, V. N. Petrov, G. B. Stuchinskiĭ & E. I. Yanyushkin (1987) *Spin-polarized photoemission from GaAsP* **Soviet Physics Solid State 29**, 823-6.

Zakharchenya, B. I., V. G. Fleisher, R. I. Dzhioev, Yu. P. Veshchunov & I. B. Rusanov (1971) *Effect of optical orientation of electron spins in a GaAs crystal* **JETP Letters 13**, 137-9.

Zeman, H. D., K. Jost & S. Gilad (1971) *The optimization of low energy scattering for producing a beam of spin-polarized electrons* **Abstracts of the VIIth International Conference of the Physics of Electronic and Atomic Collisions, Amsterdam, 1971** (Amsterdam: North Holland) pp. 1005-6.

Zucca, Ricardo R. L., John P. Walter, Y. R. Shen & Marvin L. Cohen (1970) *Wavelength modulation spectra of GaAs and silicon* **Solid State Communications 8**, 627-32.

Zürcher, P. & F. Meier (1979) *Spin-polarized photoelectrons from semiconductors with chalcopyrite structure: $ZnSiAs_2$ and $ZnGeAs_2$* **Journal of Applied Physics 50**, 3687-90.